UNIVERSITA' DEGLI STUDI DI NAPOLI FEDERICO II

Dipartimento di Ingegneria Chimica, dei Materiali e della Produzione Industriale

DOTTORATO DI RICERCA
IN INGEGNERIA DEI PRODOTTI E DEI PROCESSI INDUSTRIALI

XXIX CICLO

Optical manipulation and advanced analysis of cells using an innovative optofluidic platform

COORDINATOR
Ch.mo Prof. Giuseppe Mensitieri

CANDIDATE
Martina Mugnano

TUTORS
Ch.mo Prof. P.A. Netti
Dr. Pietro Ferraro

April 2017

To Gabriella Matarazzo,

who has inspired me in life with her courage,

willpower and strength of spirit…

Two roads diverged in a yellow wood,
And sorry I could not travel both
And be one traveler, long I stood
And looked down one as far as I could
To where it bent in the undergrowth;
Then took the other, as just as fair
And having perhaps the better claim,
Because it was grassy and wanted wear;
Though as for that, the passing there
Had worn them really about the same,

And both that morning equally lay
In leaves no step had trodden black
Oh, I kept the first for another day!
Yet knowing how way leads on to way,
I doubted if I should ever come back.

I shall be telling this with a sigh
Somewhere ages and ages hence:
two roads diverged in a wood, and I -
I took the one less traveled by,
And that has made all the difference…

Robert L. Frost (1920)

The road not taken

CONTENTS

List of acronyms

ARI:	Average Refractive Index
BS:	Beam Splitter
CARS:	Coherent Amplified Raman Spectroscopy
CBC:	Complete Blood Count
CCD:	Charge-Coupled Device
CH:	Corpuscular Hemoglobin
CL:	Condenser Lens
CNR:	Contrast-to-Noise-Ratios
CTC:	Circulating Tumour Cell
CW:	Continuous Wave
DA:	Diatom Algae
DEP:	Dielectrophoresis
DH:	Digital Holography
DHM:	Digital Holographic Microscopy
DIC:	Differential Interference Contrast
DMEM:	Dulbecco's Modified Eagle Medium
ECM:	Extra-Cellular Matrix
EDTA:	Ethylene-Diamine-Tetra-Acetic acid
ESA:	Early Stage Adhesion
ETHD-1:	Ethidium Homo-Dimer
FA:	Focal Adhesion
FACS:	Fluorescence Activated Cell Sorting
FF-OCM:	Full-Field Optical Coherence Microscopy
FLIM:	Fluorescence Lifetime Imaging
GFP:	Green Fluorescence Protein
H:	Healthiness (parameter)
HOT:	Holographic Optical Tweezers
IE:	Injurious Exposure
IR:	InfraRed
IRIDA:	Iron Refractory Iron Deficiency Anaemia
L:	Lens

LA-PAT: Linear-Array-based Photo-Acoustic Tomography

LB: Luria Bertani

LCLS: Low-Coherence Light Source

LED: Light Emitting Diode

LN: Lithium Niobate

LOC: Lab-On-Chip

LS: Linear Translation Stage

LSA: Late Stage Adhesion

M: Mirror

MACS: Magnetic Activated Cell Sorting

MCV: Mean Corpuscular Volume

MO: Microscope Objective

NA: Numerical Aperture

O: Object (wave)

OCM: Optical Coherence Microscopy

OCT: Optical Coherence Tomography

OPD: Optical Path Difference

OPL: Optical Path Length

OTs: Optical Tweezers

P: Porro prism

PBS: Phosphate Buffer Saline

PE: Pyroelectric

PH: Pin-Hole

PI: Propidium Iodide

PM: Piezo actuated Mirror

PR: Photo-Refractive

PV: Photo-Voltaic

PX: Pixel

PZ: Piezoelectric

QPI: Quantitative Phase Imaging

QPM: Quantitative Phase Map

R: Reference (wave)

RBC: Red blood cell

RFP: Red Fluorescence Protein

RGD: Arginine-Glycine-Aspartic acid

RI: Refractive Index

R-TPM: Rolling-Tomographic Phase Microscopy

S: Sample

SE: Safe Exposure

SF: Sigmoidal Function

SH: Shutter

SLD: Super-Luminescence Diode

SLM: Spatial Light Modulator

TL: Tube Lens

V: Volume

List of publications

- F. Merola, A. Barroso, L. Miccio, P. Memmolo, M. Mugnano, P. Ferraro, C. Denz, “Biolens behavior of RBCs under optically-induced mechanical stress, “Cytometry PART A, 16-144, DOI: 10.1002/cyto.a.23085. Impact Factor (IF): 3.181, (2017).
- F. Merola, P. Memmolo, L. Miccio, R. Savoia, M. Mugnano, A. Fontana, G. D’Ippolito, A. Sardo, A. Iolascon, A. Gambale, P. Ferraro, “Tomographic Flow Cytometry by Digital Holography”. Nature; Light: Science & Applications; DOI: 10.1038/lsa.2016.241, IF: 13.6, (2016).
- P. Memmolo, F. Merola, L. Miccio, M. Mugnano, P. Ferraro, “Investigation on dynamics of red blood cells through their behavior as biophotonic lenses,” J. Biomed. Opt. 21(12), DOI: 10.1117/1.JBO.21.12.121509, 121509, IF: 2.5, (2016).
- Calabuig, M. Mugnano, L. Miccio, S. Grilli, P. Ferraro, “Investigating fibroblast cells under “safe” and “injurious,” blue-light exposure by holographic microscopy,” J. Biophotonics 1–9, DOI: 10.1002/jbio.201500340, IF: 3.8, (2016).
- S. Fusco, P. Memmolo, L. Miccio, F. Merola, M. Mugnano, A. Paciello, P. Ferraro, P. A. Netti, “Nanomechanics of a fibroblast suspended using point-like anchors reveal cytoskeleton formation,” RSC Adv., 6, 24245, IF: 3.28, (2016).
- L. Miccio, V. Marchesano, M. Mugnano, S. Grilli, P. Ferraro, “Light induced DEP for immobilizing and orienting Escherichia coli bacteria,” Optics and Lasers in Engineering 76, 34–39, IF: 2.3, (2016).

List of proceedings

- M. Mugnano, F. Merola, P. Memmolo, L. Miccio, A. Gambale, A. Iolascon, and P. Ferraro “Quantitative phase imaging for improvement of microcytic anemia identification”, Proc. SPIE (2017).
- P. Memmolo, F. Merola, L. Miccio, M. Mugnano, and P. Ferraro, “Computational tomographic phase microscopy,” ECLEO-EQEC (2017).
- F. Merola, P. Memmolo, L. Miccio, M. Mugnano, P. Ferraro, “Tomographic flow cytometry assisted by intelligent wavefronts analysis,” SPIE Optical Metrology (2017).
- F. Merola, P. Memmolo, L. Miccio, M. Mugnano, P. Ferraro, “Red blood cells as microlenses: wavefront analysis and applications,” SPIE Optical Metrology (2017).
- P. Memmolo, T. Cacace, M. Paturzo, M. Mugnano, F. Merola, L. Miccio, and P. Ferraro, “Investigation of microfluidic particles motion by 3D holographic tracking,” EOS Optical Technologies (2017).
- M. Mugnano, P. Memmolo, L. Miccio, F. Merola, and P. Ferraro, “Tomographic Phase Microscopy as a tool for red blood cell morphological analysis,” 18th Italian National Conference on Photonic Technologies, 1-3 DOI: 10.1049/cp.2016.0941, (2016).
- M. Mugnano, A. Calabuig, S. Grilli, L. Miccio, P. Ferraro, “Quantitative phase-imaging method for measuring the phototoxicity effects of blue light on *in-vitro* cell”, 18th Italian National Conference on Photonic Technologies, DOI: 10.1049/cp.2016.0947, (2016).
- L. Miccio, P. Memmolo, F. Merola, M. Mugnano, and P. Ferraro, "Red Blood Cells are Bio-lenses With Tunable Focal Length", Imaging and Applied Optics, OSA, OSA Technical Digest (online) (Optical Society of America), paper DM3I.4, DOI: 10.1364/DH.2016.DM3I.4., (2016).
- P. Ferraro, P. Memmolo, F. Merola, L. Miccio, and M. Mugnano, "Tomographic Phase Microscopy of Rolling Cells in Microfluidic Flow," in Imaging and Applied Optics, OSA Technical Digest (online) (Optical Society of America), paper DTh3F.3, DOI: 10.1364/DH.2016.DTh3F.3, (2016).

- M. Mugnano, A. Calabuig, S. Grilli, L. Miccio, P. Ferraro, “Monitoring cell morphology during necrosis and apoptosis by quantitative phase imaging”, Proc. SPIE 9529, DOI: 10.1117/12.2186771, (2015).
- L. Miccio, P. Memmolo, F. Merola, M. Mugnano, S. Fusco, A. Paciello, P. Ferraro, and P.A. Netti, “Investigation on cytoskeleton dynamics for non-adherent cells under point-like stimuli,” Proc. SPIE 9529, Optical Methods for Inspection, Characterization, and Imaging of Biomaterials II, 95290P, DOI: 10.1117/12.2185929, (2015).
- F. Merola, P. Memmolo, L. Miccio, O. Gennari, M. Mugnano, P.A. Netti, and P. Ferraro, “Red blood cell three-dimensional morphometry by quantitative phase microscopy,” Proc. SPIE 9529, Optical Methods for Inspection, Characterization, and Imaging of Biomaterials II, 95290K, DOI: 10.1117/12.2186785, (2015).
- P. Memmolo, L. Miccio, F. Merola, O. Gennari, M. Mugnano, P.A. Netti, and P. Ferraro, “Lab on chip optical imaging of biological sample by quantitative phase microscopy,” Proc. SPIE 9336, Quantitative Phase Imaging, 933625, DOI: 10.1117/12.2086806, (2015).
- L. Miccio, F. Merola, P. Memmolo, M. Mugnano, S. Fusco, P.A. Netti, and P. Ferraro, “Investigation on cytoskeleton dynamics for no-adherent cells subjected to point-like stimuli by digital holographic microscopy and holographic optical trapping,” Proc. SPIE 9129, Biophotonics: Photonic Solutions for Better Health Care IV, 91291V, DOI: 10.1117/12.2052811 (2014).

Abstract

This doctoral research project aims to analyse complex processes of living cells using Digital Holographic Microscopy (DHM) as a three-dimensional (3D) imaging tool. DHM is a real-time, high-throughput, label-free and quantitative phase imaging technique which permits advanced cell analysis in microfluidic environment. In particular, an innovative optofluidic platform is implemented, composed of a DHM modulus and aided by holographic optical tweezers (HOT) for optical manipulation and a fluorescence modulus. This platform has been used for blood disease screening, cell manipulation studies and tracking of migrating cells.

In this thesis, three main topics have been investigated.

The first topic focuses on diagnostics, which plays several critical roles in healthcare. Here a novel and cost-effective approach for detecting real blood disorders such as iron-deficiency anaemia and thalassemia at lab-on-chip scale is shown. In addition, cell dynamics studies were performed by DHM. In particular, a study regarding the temporal evolution of cell morphology and volume during blue light exposure is reported.

The second topic aims to investigate cell mechanics. To this end, the capabilities of HOT were used to enable the generation and the independent high-precision control of an arbitrary number of 3D optical traps. The combination of HOT and DHM provides the possibility to manipulate cells, detect nano-mechanical cell response in the pN range, and reveal cytoskeleton formation. To confirm the formation of the cytoskeleton structures after the stimulation, a fluorescence imaging system was used as control.

Finally, the third topic focuses on cell manipulation using an innovative electrode-free dielectrophoretic approach (DEP) for investigating smart but simple strategies for orientation and immobilization of biological samples such as bacteria and fibroblast. In particular, the light-induced DEP is achieved using ferroelectric iron-

doped lithium niobate crystal as substrate. In this way, a dynamic platform that can dynamically regulate the cell response has been developed. In this case, DHM is going to be used as a time-lapse imaging tool for the characterization of dynamic cell processes.

In conclusion, the results show that DHM is a highly relevant method that allows novel insights into dynamic cell biology, with applications in cancer research and toxicity testing. In addition, this study could pave the way for detecting and quantifying circulating tumor cells and for providing multidimensional information on tumour metastasis. In this framework, the optofluidic platform is a promising tool for both identification and characterization of “foreign” cancer cells in the blood stream in order to achieve an early diagnosis.

Introduction

1 Optofluidic cell manipulation

1.1 Cell manipulation: state of art and recent developments

Nowadays, cell manipulation is a key step in several research area from tissue engineering to biosensors, besides the basic research in terms of biochemical pathways study [1,2]. Some well-established methods exist for single cell and cell population handling. In particular, the development of tools for the manipulation and characterization of single cells is of major importance for rapidly growing area of personalized medicine, diagnostic testing but also fundamental research, especially, purification, concentration and counting of specific cell types from complex mixtures (e.g. blood, cell culture) is often required in clinical practice. Successful detection and isolation of specific subsets of cells is the key to understand their functional heterogeneity and the single cell biology [3]. Actuators for the positioning and moving of objects such as cells must be compatible with the living conditions for cells. Therefore, new engineered nanodevices, characterized by functionalized substrates have been developed as alternative methods. Very recently, chips have been coated with components of extracellular matrix (ECM) caged with photo-deprotectable groups. By using focused light it has been possible to create patterns on the chip with de-protected ECM factors in order to guide cell adhesion towards those points [4].

When cell manipulations such as identification and sorting are needed, the gold standard methods to identify and separate a certain subpopulation are the Fluorescence Activated Cell Sorting (FACS) [5], magnetic activated cell sorting (MACS) [6] and chemically functionalized pillar-based micro-chips [7]. These techniques, although effective and promising, are limited by the necessary knowledge of the properties of the desired cell types, they are time-consuming, and require special training to be executed. Furthermore, both FACS and MACS have limitations and lack of more sophisticated cell manipulation capabilities, e.g. to

precisely control and adjust trajectories as required in elaborated cell stimulation experiments [8]. However, these procedures remain the gold standard techniques for isolation and counting of cell populations for many biomedical applications, like stem cell therapy. Furthermore, besides routine applications, these techniques have been demonstrated to (i) detect rare cells [9,10], such as circulating tumor cells (CTC), and achieve high (ii) isolation/purification rate as well as (iii) throughput. To date, cell manipulation has been majorly performed using conventional techniques and labware such as pipettes, sample tubes, microwell plates and cell culture flasks.

Notably, these strategies have only limited cell manipulation capabilities, are rather time and reagent consuming, lack sufficient precision and reproducibility and have only limited or no online monitoring capacities (e.g., integrated sensors for pH, fluorescence or magnetic field measurement). These limitations have motivated the development of microfluidic methods for enhanced spatial and temporal control of the neighbouring cellular environment, as represented by numerous publications [11-15].

New frontier in biomedical research and clinical diagnostics looks at the possibility through the control of cell manipulation to perform experiments in so called lab-on-chip (LoC) thanks to the advent of new field of the microfluidics. Although different examples of microfluidic systems exist in nature (e.g., channel networks in paper), in scientific literature the terms microfluidics or microchannels are generally employed for microfabricated fluidic networks that have characteristic dimensions below 100 μm.

Nowadays, there is the tendency to emulate biological systems on a chip, in order to reduce reagents, costs and to work with small volume of fluids, which is highly beneficial in many biomedical and clinical research scenarios which deal with limited amounts (e.g., cerebrospinal fluid) or numbers (e.g., research in rare disease) of samples. Especially in neuroscience research there is a great interest in developing microfluidic devices that provide a highly adaptable cell culture platform and may find applications in modelling central nervous system (CNS) injury and neurodegeneration [16]. Importantly, the overall reduction of chip size holds a great potential for portability as well as integration of sensors and actuators, which is an important factor in current lab-on a-chip and point-of-care diagnostics.

1.2 Biological significance of cell manipulation studies

In the life sciences, particularly in cell biology, a technique is needed to manipulate structures inside closed objects - for example inside living cells without opening them, since otherwise their viability would be impaired. The scientific merit of the micromanipulation of biological cells is the combination of this moderately difficult physical task with sometimes sophisticated biochemical techniques. It is a truly interdisciplinary approach, based on physical principles.

A cell is an extremely complex system comprising many different classes of biomolecules. Among those particularly proteins, lipids, and metabolites are highly dynamic and therefore key to the adaptability of cells to immediately respond to external stimuli. The human body comprises more than 100 different cell types and tissues, each evolutionary and individually tailored to fulfil specific tasks, individually or in concert with other cells and tissues. Indeed, this complexity is not limited to different cell types, but is also reflected in the heterogeneity among populations of the same cell type. Even minor dysregulation of specific cells or cell–cell interactions can have dramatic effects on the homeostasis of a tissue or even the entire organism. Consequently, the detailed and quantitative study of cellular processes and their dynamics to understand causes and consequences of (dys)regulation is imperative to combat diseases such as cancer, cardiovascular and neurodegenerative disorders. It is furthermore one of the major goals of system biology research. To elucidate these processes and to reveal their underlying principles, one needs to investigate adaptations of cells on the level of proteins, lipids and metabolites under a large variety of conditions. Indeed, microfluidic applications hold a great potential to boost systems biology research, as they offer incomparable possibilities to manipulate and perturb cells, starting from minute sample amounts, in an automated, reproducible, fast and efficient way. Therefore in the future microfluidics might be a cornerstone of sample preparation for disciplines such as (clinical) proteomics which aim at quantifying a large number of biomolecules from complex samples, i.e. body fluids, with high reproducibility, precision and accuracy. Moreover, microfluidics offers a higher throughput, as well as novel opportunities for temporal and spatial analysis of samples, which are

otherwise not achievable. In principle, cell manipulation studies have four major goals: (i) separation of cells, (ii) single cell analysis, (iii) subcellular analysis, as well as (iv) temporal analysis of cellular processes and signalling.

The first goal is the separation of cells, particularly for blood samples, which are often used in clinical diagnostics, there is a significant interest to separate and analyse specific cell types. This is not only limited to the components of blood such as erythrocyte, leucocyte, or platelets, but it could be applied also to microparticles, CTC, or even bacteria. Standard biochemical methods are based on differential and/or density centrifugation are rather slow and laborious, and even more importantly cannot be automated and therefore lack reproducibility. The last technologies such as FACS and MACS are more powerful, however, may require specific fluorescence labelling of cells, interfering with physiology of sample and this could give some artefacts, can be time and cost intensive or have limited capacity. Therefore, in this framework microfluidics represents a most promising alternative that may allow a fast, comparably cheap, automated and high-throughput method to separate different cell types for subsequent analysis with accuracy at the single cell level.

The second goal of manipulation studies is single cell analysis. The main interest for individual cell analysis derives from cancer research, [17,18] where precise methods are needed to define cellular phenotypes from average population data. For this purpose, many imaging technique are developing in order to identify cancer cells based on their optical and biophysics properties. Javidi's research group has demonstrated to be able to distinguish cancer cells from normal cells through comparison of optical path length differences, in synthesis, a high-dynamic-range phase measurement system that does not need unwrapping processing was used for cancer cell identification. The important property of their system was that it could measure transparent objects without using the phase unwrapping process even if the thickness of the object is more than one wavelength. Moreover, the system can provide the quantitative phase information with high accuracy and it may be used for advanced cell analyses, such as quality control, functional inspection of cells and dynamics [19]. In the 2010 S. Kim and B. H. Lee reported the results for the feasibility of identifying cancer cells by measuring the refractive

index (RI) distribution across a single live cell with ultrahigh resolution full-field optical coherence microscopy (FF-OCM) [20]. This work showed that cancer cells had higher RI than normal ones. Recently, RI of a live cell has gained much attention as an attractive indicator of cell abnormality. The cell RI attributable to optical interaction of light field with cellular organelles is informative for quantifying chemical composition within cellular structures, so that the potential application has been considered in cell physiology and pathology. In cancer biology, it is well known that the RIs of cancer cells are relatively higher than normal cells [21-23]. This approach using the FF-OCM has significant potential for cancer diagnosis and dynamic cell analysis as in situ label-free biophysical assay. However, many significant studies have underline the importance to define cellular phenotypes from average population data, particularly, in stem cell research, separate analyses of individual cells led to the characterization of varying levels of proteins abundance depending on time and differentiation of cells [24]. The biggest challenge in the field still remains the selective and robust isolation of single cells out of a tissue, cell culture or body fluid, often characterized by poor efficiency and reproducibility. Indeed, recent advances in single cell analysis make use of microfluidics and optical microscopy to overcome some of the limitations. Over the past decades a large number of high quality studies on single cell analysis using microfluidic chips have been published in the literature [25-31]. The field of single cell analysis, as can be assessed in the recommended literature, is vast and is starting to translate into successful industrial products, such as the case for the Fluidigm®C1 equipment, [32] an automated solution for single cell genomics being capable of handling up to 800 cells individually in a single run, a considerable throughput capability.

The third goal of manipulation studies is subcellular analysis. In fact, one of the most striking limitations of -omics technologies typically used for the in-depth analysis of cells is the lack of spatial information. Even so, it is well verified the dynamic process of proteins inside a cell, many proteins have multiple subcellular localizations that reflect different functions, or may translocate in response of a specific intracellular or external stimuli [33] or in pathological conditions [34]. However, information such as the spatial distribution of proteins is lost in standard large-scale proteome analysis. Although these studies can provide quantitative

information on expression levels for thousands of proteins, they cannot discriminate whether the distribution of proteins between different organelles or sub-compartments has changed. Therefore, the separate analysis of isolated organelles and their content is of major interest as it allows studying the subcellular localization and distribution of proteins, representing a critical step towards a better understanding of their individual functions and dynamics. Regarding proteomic studies for example, the standard methods to analyse isolated organelles, [35–37] or sub-compartments [38–40] provide for classical, laborious and non-automated protocols. Typically, they encompass the mechanical rupture of the plasma membrane, homogenization of cellular matrix, and separation of its components by differential/density centrifugation. Alternative techniques, e.g. MACS, rely on the use of affinity tags or antibodies against specific epitopes present on the organelle's surface. Thus, microfluidics may play an important role and many recent publications have demonstrated different possibilities and prototypes for cell and organelle separations, [41,42] some of which will be further described later in this doctoral dissertation.

To conclude, the fourth goal of manipulation studies is temporal analysis of cellular processes and signalling, which represents another significant issue. Recently, increasingly powerful mass spectrometry-based studies considerably improved our knowledge about cellular signalling, its complexity and dynamics [43-45]. However, it concurrently became more and more evident, that the detailed elucidation of such dynamic processes as well as the underlying and intertwined networks requires more powerful sample preparation techniques. Notably, in cells different situations involve different timescale dimensions: processes such as regulatory protein phosphorylation upon kinase activation, or ion transport can occur within milliseconds to seconds, while others, such as changes in protein expression during cell cycle, require minutes to hours. Whereas rather slow processes can be easily followed in a time-resolved manner using conventional and mainly manual sample preparation methods, such strategies are not sufficiently reproducible and robust to study fast and short term processes. Initial signaling events are too fast to tolerate imprecise sampling and consequently measuring points; studying such fast processes demands for sub-second time resolution in combination with high accuracy and precision during sampling.

1.3 Cell handling techniques

Cells are the basic units of living organisms that regulate all life activities. Different types of cells are responsible for their specific biological processes which are relevant to cell metabolism, migration, growth, apoptosis and even cancerization in the cellular microenvironment. In this context, the ability to isolate specific types of cells from a large population of cells is highly important for disease diagnosis, intracellular analysis, and stem cell studies. Considering cell sizes are about 10 microns in diameter, conventional methods cannot easily manipulate the cells at a micro-sized scale in standard tissue culture dishes; precise control and efficient capture of target cells in the cell mixture are greatly challenged in this regard.

Nowadays, microfluidic devices for cell manipulation, for the study of cell properties and/or cellular processes analysis emerged constantly. Microfluidics is the growing field embracing all the techniques and instruments aimed to confine liquids in small regions of space, providing accurate control of fluid streams. In particular, it has become more and more apparent as the study of biological samples can benefit from the use of this technology (Figure 1).

Optimizing existing protocols and/or developing original research are the main motivation drawing researchers' interest to the microfluidic field. Different microfluidic technologies for cell manipulation have been described in literature. These can be divided into passive, active or integrated strategies. The cells' position within microchannels can be controlled either by (i) rational design of the microfluidic structures, which results in deflection of cells' trajectories, as for the passive strategies, or (ii) as a result of a force generated by an actuator, taking into account the cells' electrical, magnetic and mechanical properties, as for active strategies. Often it is advantageous to combine different strategies to improve performance and functionalities within a single chip, referred to as integrated systems. However, integration is challenging, especially concerning handling simplicity, such as the need for alignment of micrometer-sized structures or fluidic and electronic connections [46–48].

General approaches developed for cell handling and isolation in the microfluidic devices including affinity-based approaches for cell recognition and typical physical principles for cell isolation by microfabrication structures such as hydrophoresis, dielectrophoresis, and acoustophoresis, etc [8]. In this thesis will be discuss mainly two cell handling techniques: optical tweezers and dielectrophoresis.

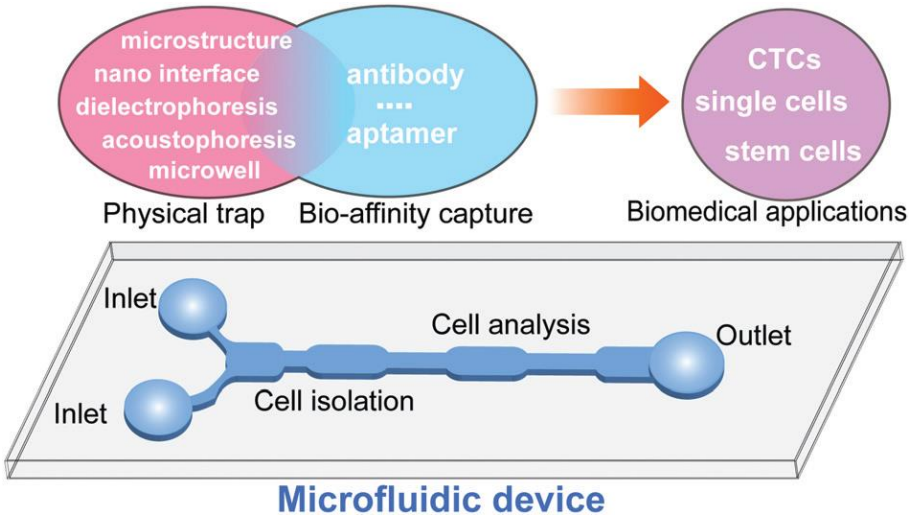

Figure 1: Example of microfluidic device for cell isolation and analysis for biomedical applications. Microfluidic technologies based on physical trapping and bioaffinity capture of target cells are developed for efficient cell isolation and followed with cell analysis on a single microchip.

1.3.1 Optical tweezers

In every day life, light is perceived to be a gentle physical entity. Thus, it may appear as a surprise that transporting objects with light or working deep in the interior of closed objects is lab routine in the world of biological microscopy. There, light is used as a quasi-mechanical working tool. Light does not only transmit heat (energy) but also exerts force and pressure. When combined with a microscope, the light of a comparably small (a few hundred milliwatt (mW)) desktop laser can be focused to such high intensities that it will produce temperatures such as those that prevail in the interior of the sun and can generate plasma (laser microbeams).

Objects which would be difficult to penetrate with a mechanical tool (optical tweezers) can be moved, even behind a wall.

For single cell manipulation, some optical techniques have been developed.

Among these, optical tweezers represent a quite new technique where a laser beam focused on a small area generates forces able to trap micrometer sized objects (viruses, bacteria and eukaryotic cells) [49]. OTs allow the manipulation of cells directly in suspension, in a contact-less and non-invasive manner [50-53]. OTs have been widely exploited for studying cells in a suspended state, such as red blood cells, where the great elasticity of their membranes permits easy deformability, stretching and rotation [54-57].

In particular, Guck and coworkers created a microfluidic cell stretcher able to measure the deformability of membranes of suspended cells by using two counter-propagating laser beams inside a microfluidic channel [58]. The apparatus was able to trap the cells under test and induce a deformation on the whole cell population. The ability of their apparatus to discern between healthy and cancer cells as a consequence of the different deformability was proven. Schmidt and coworkers proposed for the first time a dual trap system able to promote cell adhesion in a suspended configuration [59,60]. The experiments demonstrated that the mechanical responses of the acto-myosin cortical network are responsible for equilibrating cell internal osmotic pressure and shape fluctuations. Moreover, OT allows accurate three-dimensional control with nanometer accuracy by an all-optical approach.

In particular, Jordan and coworkers [2] have demonstrated the manipulation of multiple bacteria in 3D volume by holographic OT.

However, the number of samples that is possible to control with OT is limited. To this end, another technique named holographic optical tweezer, which enables the generation and the high-precise control of an arbitrary number of 3D optical traps. HOT have already been used for mechano-biophysical analysis of the inner structure of living cells, [61,62] cell identification, manipulation and tracking [51, 63–71]. Sometime the combination of HOT and DHM has been already exploited to study the propagation of the strain inside adherent cells induced by locally applied forces [72].

1.3.2 Dielectrophoresis

An alternative for cell handling to the mentioned methods above in the paragraph 1.1 is dielectrophoresis; a technique that eliminates extensive sample preparation (no antibody labeling, one needs only to prepare a single sample) and provides a high selectivity at separating rare cells.

DEP is the motion of a polarizable particle in a suspending medium due to the presence of a non-uniform electric field [73–75]. With no needs to know the surface properties of the desired cells, DEP can noninvasively sort populations through differences with in the interior of cells, as well as their exterior. In conventional DEP techniques, metallic microelectrodes with various geometries are patterned on a microfluidic device using conventional lithography techniques [76–78].

DEP has been used for the isolation of several rare cell types including human cervical, breast and colorectal cancer and leukemia cells [73, 79, 80]. Cell isolation has been done through both batch separation [81– 83], where rare cells population is trapped by positive DEP force while background cells pass through the microdevice, and continuous separation [79], where rare cells continuously separate from background cells. Among the several applications of the DEP technique in biology, great interest has been focused on the immobilization of microbial organisms where the study of the early stage development of biofilms is desirable [84–86].

In literature, it has been largely demonstrated that DEP through local micro/nano-electrodes allows a time dependent accumulation of bacteriophages; thus resulting an excellent technique not only to immobilize but also to concentrate microorganisms [87–92].

Recently, new DEP principles have been demonstrated based on electrode-free approaches that allow to realize devices with great versatility in terms of liquid/polymer patterning geometries. The electric fields able to manipulate liquids and immobilize particles are generated by exploiting the properties of ferroelectric crystals avoiding external electric circuits and voltage generators. In particular, it has been successfully proved that pyroelectric (PE) and photorefractive (PR) fields can be employed for dispensing liquid droplets down to atto-liter volumes [93], for

trapping microparticles [94] and for creating liquid/polymer structures such as biodegradable polymer microneedles [95], tunable micro-lenses [96] or microfluidic channels [97]. The driving stimuli for PE and PR fields generation are thermal and optical, respectively.

Miccio et. Al. demonstrated that is possible to apply such electrode-free DEP cues for immobilization and orientation of biological objects [98]. In particular, such fields are used to manipulate bacteria cells maintaining them alive. In order to test the applicability of this innovative technique they tested the ability of Escherichia coli, Gram negative bacteria, to respond to the external electric field on the surface of ferroelectric iron-doped lithium niobate crystals (Fe: LiNbO3) [99]. The PR effect is the best choice as the high temperature reached in the PE devices could alter the normal conditions and damage the samples. In the recent years DEP trapping of nano-particles by PR induced electric fields has been largely studied [100] and supported by experimental validations [101,102]. In literature, the interaction of PR field with biological sample has been investigated to induce death in tumor cell cultures [103]. In the present work such fields are used to manipulate bacteria cells and fibroblasts maintaining them alive.

The experimental results and discussion on advantages and drawbacks will be described in the section 5.

References

[1] Melamed S, et al. A printed nanolitre-scale bacterial sensor array. Lab Chip; 11(1):139–46, 2011.

[2] Jordan P, et al. Creating permanent 3D arrangements of isolated cells using holographic optical tweezers. LabChip; 5(11):1224–8, 2005.

[3] Parvin Abraham, Tessy Thomas Maliekal, Single cell biology beyond the era of antibodies: relevance, challenges, and promises in biomedical research, Cell. Mol. Life Sci., review, DOI 10.1007/s00018-016-2382-z, 2016.

[4] Griffin DR, et al. Hybrid photopatterned enzymatic reaction (HyPER) for in situ cell manipulation. Chembiochem; 15(2):233–42, 2014.

[5] Lostumbo A, et al. Flow cytometry: a new approach for the molecular profiling of breast cancer. Exp Mol Pathol; 80(1):46–53, 2006.

[6] Kato K, Radbruch A. Isolation and characterization of CD34+ hematopoietic stem cells from human peripheral blood by high-gradient magnetic cell sorting. Cytometry;14(4):384–92, 1993.

[7] Nagrath S, et al. Isolation of rare circulating tumour cells in cancer patients by microchip technology. Nature; 450(7173):1235–9, 2007.

[8] Pedro Novo, Margherita Dell'Aica, Dirk Janasek and René P. Zahedi, High spatial and temporal resolution cell manipulation techniques in microchannels, Analyst, 141, 1888, 2016.

[9] Y. Hu, L. Fan, J. Zheng, R. Cui, W. Liu, Y. He, X. Li and S. Huang, Detection of circulating tumor cells in breast cancer patients utilizing multiparameter flow cytometry and assessment of the prognosis of patients in different CTCs levels, Cytometry, Part A, 2010, 77A(3), 213–219.

[10] T. Hristozova, R. Konschak, V. Budach and I. Tinhofer, A simple multicolor flow cytometry protocol for detection and molecular characterization of circulating tumor cells in epithelial cancers, Cytometry, Part A, 2012, 81A(6), 489–495.

[11] P. Li, Z. S. Stratton, M. Dao, J. Ritz and T. J. Huang, Probing circulating tumor cells in microfluidics, Lab Chip, 2013, 13(4), 602–609.

[12] A. Lenshof and T. Laurell, Continuous separation of cells and particles in microfluidic systems, Chem. Soc. Rev., 39(3), 1203–1217, 2010.

[13] F. Merola, L. Miccio, P. Memmolo, G. Di Caprio, A. Galli, R. Puglisi, D. Balduzzi, G. Coppola, P. Netti and P. Ferraro, Digital holography as a method for 3D imaging and estimating the biovolume of motile cells, Lab Chip, 13, 4512, 2013.

[14] F. Merola, P. Memmolo, L. Miccio, V. Bianco, M. Paturzo, and P. Ferraro, Diagnostic Tools for Lab-on-Chip Applications Based on Coherent Imaging Microscopy Proceedings of the IEEE | Vol. 103,No. 2, February 2015.

[15] G. M. Whitesides, The origins and the future of microfluidics, NATURE, Vol 442, doi:10.1038/nature05058, 27 July 2006.

[16] J. W. Park, B. Vahidi, A. M Taylor, S. W. Rhee and N. L. Jeon, Microfluidic culture platform for neuroscience research, Nature Protocols 1, 2128 – 2136, 2006.

[17] M. Niepel, S. L. Spencer and P. K. Sorger, Non-genetic cell-to-cell variability and the consequences for pharmacology, Curr. Opin. Chem. Biol., 13(5–6), 556–561, 2009.

[18] A. A. Cohen, N. Geva-Zatorsky, E. Eden, M. Frenkel - Morgenstern, I. Issaeva, A. Sigal, R. Milo, C. Cohen-Saidon, Y. Liron, Z. Kam, L. Cohen, T. Danon, N. Perzov and U. Alon, Dynamic proteomics of individual cancer cells in response to a drug, Science, 322(5907), 1511–1516, 2008.

[19] E. Watanabe, T. Hoshiba, and B. Javidi, High-precision microscopic phase imaging without phase unwrapping for cancer cell identification, OPTICS LETTERS, Vol. 38, No. 8, 2013.

[20] W. J. Choi, D. I. Jeon, S.-G. Ahn, J.-H. Yoon, S. Kim, and B. H. Lee, Full-field optical coherence microscopy for identifying live cancer cells by quantitative measurement of refractive index distribution, OPTICS EXPRESS, Vol. 18, No. 22, 23285, 2010.

[21] V. Backman, M. B. Wallace, L. T. Perelman, J. T. Arendt, R. Gurjar, M. G. Müller, Q. Zhang, G. Zonios, E. Kline, J. A. McGilligan, S. Shapshay, T. Valdez, K. Badizadegan, J. M. Crawford, M. Fitzmaurice, S. Kabani, H. S. Levin, M. Seiler, R.

R. Dasari, I. Itzkan, J. Van Dam, M. S. Feld, and T. McGillican, “Detection of preinvasive cancer cells,” Nature 406(6791), 35–36, 2000.

[22] D. Bourgaize, T. R. Jewell, and R. G. Buiser, Biotechnology: Demystifying the Concepts (Addison Westly Longman, San Francisco, 1999.

[23] X. J. Liang, A. Q. Liu, C. S. Lim, T. C. Ayi, and P. H. Yap, “Determining refractive index of single living cell using an integrated microchip,” Sens. Actuator A 133(2), 349–354, 2007.

[24] H. H. Chang, M. Hemberg, M. Barahona, D. E. Ingber and S. Huang, Transcriptome-wide noise controls lineage choice in mammalian progenitor cells, Nature, 453(7194), 544–547, 2008.

[25] M. Junkin and S. Tay, Microfluidic single-cell analysis for systems immunology, Lab Chip, 2014, 14, 1246–1260.

[26] A. Rakszewska, J. Tel, V. Chokkalingam and W. T. S. Huck, One drop at a time: toward droplet microfluidics as a versatile tool for single-cell analysis, NPG Asia Mater, 2014, 6, e133.

[27] H. Yin and D. Marshall, Microfluidics for single cell analysis, Curr. Opin. Biotechnol., 2012, 23(1), 110–119. Analytical biotechnology.

[28] T. A. Duncombe, A. M. Tentori and A. E. Herr, Microfluidics: reframing biological enquiry, Nat. Rev. Mol. Cell Biol., 2015, 16(9), 554–567.

[29] P. K. Chattopadhyay, T. M. Gierahn, M. Roederer and J. Christopher Love, Single-cell technologies for monitoring immune systems, Nat. Immunol., 2014, 15(2), 128–135.

[30] T. P. Lagus and J. F. Edd, A review of the theory, methods and recent applications of high-throughput single-cell droplet microfluidics, J. Phys. D: Appl. Phys., 2013, 46(11), 114005.

[31] C. Gawad, W. Koh and S. R. Quake, Single-cell genome sequencing: current state of the science, Nat. Rev. Genet., 2016, DOI: 10.1038/nrg.2015.16

[32] See https://www.fluidigm.com/products/c1-system (consulted on the 1st february 2016).

[33] P. E. Stenberg, R. P. McEver, M. A. Shuman, Y. V. Jacques and D. F. Bainton, A platelet alpha-granule membrane protein (GMP-140) is expressed on the plasma membrane after activation, J. Cell Biol., 101(3), 880–886, 1985.

[34] 55 E. D. Klootwijk, M. Reichold, A. Helip-Wooley, A. Tolaymat, C. Broeker, S. L. Robinette, J. Reinders, D. Peindl, K. Renner, K. Eberhart, N. Assmann, P. J. Oefner, K. Dettmer, C. Sterner, J. Schroeder, N. Zorger, R. Witzgall, S. W. Reinhold, H. C. Stanescu, D. Bockenhauer, G. Jaureguiberry, H. Courtneidge, A. M. Hall, A. D. Wijeyesekera, E. Holmes, J. K. Nicholson, K. O'Brien, I. Bernardini, D. M. Krasnewich, M. Arcos- Burgos, Y. Izumi, H. Nonoguchi, Y. Jia, J. K. Reddy, M. Ilyas, R. J. Unwin, W. A. Gahl, R. Warth and R. Kleta, Mistargeting of peroxisomal EHHADH and inherited renal fanconi's syndrome, N. Engl. J. Med., 370(2), 129–138. PMID: 24401050, 2014.

[35] A. Sickmann, J. Reinders, Y. Wagner, C. Joppich, R. Zahedi, H. E. Meyer, B. Schönfisch, I. Perschil, A. Chacinska, B. Guiard, P. Rehling, N. Pfanner and C. Meisinger, The proteome of Saccharomyces cerevisiae mitochondria, Proc. Natl. Acad. Sci. U. S. A., 100(23), 13207–13212, 2003.

[36] S. W. Taylor, E. Fahy, B. Zhang, G. M. Glenn, D. E. Warnock, S. Wiley, A. N. Murphy, S. P. Gaucher, R. A. Capaldi, B. W. Gibson and S. S. Ghosh, Characterization of the human heart mitochondrial proteome, Nat. Biotechnol., 21(3), 281–286, 2003.

[37] J. R. Yates III, A. Gilchrist, K. E. Howell and J. J. M. Bergeron, Proteomics of organelles and large cellular structures, Nat. Rev. Mol. Cell Biol., 6(9), 702–714, 2005.

[38] M. Niemann, S. Wiese, J. Mani, A. Chanfon, C. Jackson, C. Meisinger, B. Warscheid and A. Schneider, Mitochondrial outer membrane proteome of Trypanosoma brucei reveals novel factors required to maintain mitochondrial morphology, Mol. Cell. Proteomics, 12(2), 515–528, 2012.

[39] R. P. Zahedi, A. Sickmann, A. M. Boehm, C. Winkler, N. Zufall, B. Schönfisch, B. Guiard, N. Pfanner and C. Meisinger, Proteomic analysis of the yeast mitochondrial outer membrane reveals accumulation of a subclass of preproteins, Mol. Biol. Cell, 17(3), 1436–1450, 2006.

[40] F.-N. Vögtle, J. M. Burkhart, S. Rao, C. Gerbeth, J. Hinrichs, J.-C. Martinou, A. Chacinska, A. Sickmann, R. P. Zahedi and C. Meisinger, Intermembrane space proteome of yeast mitochondria, Mol. Cell. Proteomics, 11(12), 1840–1852, 2012.

[41] H. Lu, S. Gaudet, M. A. Schmidt and K. F. Jensen, A microfabricated device for subcellular organelle sorting, Anal. Chem., 76(19), 5705–5712. PMID: 15456289, 2004.

[42] M. Moschallski, M. Hausmann, A. Posch, A. Paulus, N. Kunz, T. T. Duong, B. Angres, K. Fuchsberger, H. Steuer, D. Stoll, S. Werner, B. Hagmeyer and M. Stelzle, MicroPrep: Chip-based dielectrophoretic purification of mitochondria, Electrophoresis, 31(15), 2655–2663, 2010.

[43] K. Sharma, R. C. J. D'Souza, S. Tyanova, C. Schaab, J. R. Wiśniewski, J. Cox and M. Mann, Ultradeep human phosphoproteome reveals a distinct regulatory nature of Tyr and Ser/Thr-based signaling, Cell Rep., 8(5), 1583–1594, 2014.

[44] Y. Zheng, C. Zhang, D. R. Croucher, M. A. Soliman, N. St- Denis, A. Pasculescu, L. Taylor, S. A. Tate, W. Rod Hardy, K. Colwill, A. Y. Dai, R. Bagshaw, J. W. Dennis, A.-C. Gingras, R. J. Daly and T. Pawson, Temporal regulation of EGF signalling networks by the scaffold protein Shc1, Nature, 499(7457), 166–171, 2013.

[45] F. Beck, J. Geiger, S. Gambaryan, J. Veit, M. Vaudel, P. Nollau, O. Kohlbacher, L. Martens, U. Walter, A. Sickmann and R. P. Zahedi, Time-resolved characterization of cAMP/PKA-dependent signaling reveals that platelet inhibition is a concerted process involving multiple signaling pathways, Blood, 123(5), e1–e10, 2013.

[46] P. Novo, F. Volpetti, V. Chu and J. P. Conde, Control of sequential fluid delivery in a fully autonomous capillary microfluidic device, Lab Chip, 13, 641–645, 2013.

[47] P. Novo, V. Chu and J. P. Conde, Integrated optical detection of autonomous capillary microfluidic immunoassays: a hand-held point-of-care prototype, Biosens. Bioelectron., 57, 284–291, 2014.

[48] E Tavares da Costa, M F. Mora, P A. Willis, C L. do Lago, H Jiao and C D. Garcia, Getting started with open-hardware: Development and control of microfluidic devices, Electrophoresis, 35(16), 2370–2377, 2014.

[49] Dholakia K, Cizmar T. Shaping the future of manipulation. NatPhoton; 5 (6):335–42, 2011.

[50] H. Zhang and K.-K. Liu, J. R. Soc., Interface, 2008, 5, 671–690.

[51] D. G. Grier, Nature, 2003, 424, 810–816.

[52] D. J. Odde and M. J. Renn, Trends Biotechnol., 1999, 17, 385–389.

[53] A. D. Franck, A. F. Powers, D. R. Gestaut, T. Gonen, T. N. Davis and C. L. Asbury, Nat. Cell Biol., 2007, 9, 832–837

[54] M. Gu, S. Kuriakose and X. Gan, Opt. Express, 2007, 15, 1369–1375.

[55] N. Cardenas, L. Yu and S. K. Mohanty, Proc. SPIE, 2011, 7906, DOI: 10.1117/12.876001.

[56] S. Raj, M. Marro, M. Wojdyla and D. Petrov, Biomed. Opt. Express, 2012, 3, 753–763.

[57] S. Mohanty, K. Mohanty and P. Gupta, Opt. Express, 2005, 13, 4745–4751.

[58] J. Guck, S. Schinkinger, B. Lincoln, F. Wottawah, S. Ebert, M. Romeyke, D. Lenz, H. M. Erickson, R. Ananthakrishnan and D. Mitchell, Biophys. J., 2005, 88, 3689–3698.

[59] D. Mizuno, R. Bacabac, C. Tardin, D. Head and C. F. Schmidt, Phys. Rev. Lett., 2009, 102, 168102.

[60] F. Schlosser, F. Rehfeldt and C. F. Schmidt, Philos. Trans. R. Soc., B, 2015, 370, 20140028.

[61] A . Barroso, M. Woerdemann, A. Vollmer, G. von Bally, B. Kemper and C. Denz, Small, 2013, 9, 885–893.

[62] S. A. Ermilov, D. R. Murdock, F. Qian, W. E. Brownell and B. Anvari, J. Biomech., 2007, 40, 476–480.

[63] P. Jordan, J. Leach, M. Padgett, P. Blackburn, N. Isaacs, M. Goks¨or, D. Hanstorp, A. Wright, J. Girkin and J. Cooper, Lab Chip, 2005, 5, 1224–1228.

[64] L. Miccio, P. Memmolo, F. Merola, S. Fusco, V. Embrione, A. Paciello, M. Ventre, P. Netti and P. Ferraro, Lab Chip, 2014, 14, 1129–1134.

[65] M. DaneshPanah, S. Zwick, F. Schaal, M. Warber, B. Javidi and W. Osten, J. Disp. Technol., 2010, 6, 490–499.

[66] P. Memmolo, L. Miccio, F. Merola, A. Paciello, V. Embrione, S. Fusco, P. Ferraro and P. Antonio Netti, Optic. Laser. Eng., 2014, 52, 206–211.

[67] K. Uhrig, R. Kurre, C. Schmitz, J. E. Curtis, T. Haraszti, A. E.-M. Clemen and J. P. Spatz, Lab Chip, 2009, 9, 661–668.

[68] M. Padgett and R. Di Leonardo, Lab Chip, 2011, 11, 1196–1205.

[69] G. Thalhammer, R. Steiger, M. Meinschad, M. Hill, S. Bernet and M. Ritsch-Marte, Biomed. Opt. Express, 2011, 2, 2859–2870.

[70] A. Jesacher, C. Maurer, A. Schwaighofer, S. Bernet and M. Ritsch-Marte, Opt. Express, 2008, 16, 4479–4486.

[71] G. R. Kirkham, E. Britchford, T. Upton, J. Ware, G. M. Gibson, Y. Devaud, M. Ehrbar, M. Padgett, S. Allen and L. D. Buttery, Sci. Rep., 2015, 5, 8577.

[72] J. Reed, J. J. Troke, J. Schmit, S. Han, M. A. Teitell and J. K. Gimzewski, ACS Nano, 2008, 2, 841–846.

[73] Salmanzadeh A, et al. Isolation of rare cancer cells from blood cells using dielectrophoresis. Conf Proc IEEE Eng Med Biol Soc 2012; 2012:590–3.

[74] Qian C, et al. Dielectrophoresis for bioparticle manipulation. Int J Mol Sci 2014; 15(10):18281–309.

[75] Dash S, Mohanty S.Dielectrophoretic separation of micron and submicron particles: a review. ELECTROPHORESIS 2014; 35(18):2656–72.

[76] Vykoukal J,et al. Enrichment of putative stem cells from adipose tissue using dielectrophoretic field-flow fractionation. LabChip 2008; 8(8):1386–93.

[77] Huang Y,et al. Dielectrophoretic cell separation and gene expression profiling on microelectronic chip arrays. Anal Chem 2002; 74(14):3362–71.

[78] Sabuncu AC, et al. Dielectrophoretic separation of mouse melanoma clones. Biomicrofluidics 2010; 4:2.

[79] Moon HS, et al. Continuous separation of breast cancer cells from blood samples using multi-orifice flow fractionation (MOFF) and dielectrophoresis (DEP). LabChip2011;11(6):1118–25.

[80] Becker FF, et al.The removal of human leukemia cells from blood using interdigitated microelectrodes. JPhyD: ApplPhys1994; 27(12):2659.

[81] Yang J, et al. Cell separation on microfabricated electrodes using dielectrophoretic/gravitational field-flow fractionation. Anal Chem 1999; 71(5):911–8.

[82] Gascoyne PR, et al. Isolation of rare cells from cell mixtures by dielectrophoresis. Electrophoresis 2009; 30(8):1388–98.

[83] Huang Y, et al. The removal of human breast cancer cells from hematopoietic CD34+ stem cells by dielectrophoretic field-flow-fractionation. J Hematother Stem CellRes1999; 8(5):481–90.

[84] Kano T, et al. A microfluidic device for bacteria immobilization in a microporous carrierby dielectrophoresis. J Micro-Nano Mechatron 2012; 7 (1–3):61–8.

[85] Sharma S, Conrad JC. Attachment from flow of Escherichia coli bacteria onto silanized glass substrates. Langmuir 2014; 30(37):11147–55.

[86] Hutchison JB, et al. Single-cell control of initial spatial structure in biofilm development using laser trapping. Langmuir 2014; 30(15):4522–30.

[87] Syed LU, et al. Dielectrophoretic capture of E. coli cells at micropatterned nanoelectrode arrays. Electrophoresis 2011; 32(17):2358–65.

[88] Castellarnau M,et al. Dielectrophoresis as a tool to characterize and differentiate isogenic mutants of Escherichia coli. Biophys J 2006; 91 (10):3937–45.

[89] Lapizco-Encinas BH, et al. Aninsulator-based(electrodeless) dielectrophoretic concentrator for microbes in water. J Micro boil Methods 2005; 62(3):317–26.

[90] Braff WA, et al. Dielectrophoresis-based discrimination of bacteria at the strain level based on their surface properties. PLoSOne 2013; 8(10):e76751.

[91] Cai D,et al. An integrated microfluidic device utilizing dielectrophoresis and multiplexarray PCR for point-of-care detection of pathogens. LabChip 2014;14(20):3917–24.

[92] Madiyar FR, et al. Manipulation of bacteriophages with dielectrophoresis on carbon nanofiber nanoelectrodearrays. Electrophoresis2013;34(7):1123–30.

[93] Ferraro P, et al. Dispensing nano-pico droplets and liquid patterning by pyroelectrodynamic shooting. Nat Nanotechnol 2010; 5(6):429–35.

[94] Miccio L,et al. All-optical microfluidic chips for reconfigurable dielectro-phoretic trapping through SLM light induced patterning. LabChip 2012;12 (21):4449–54.

[95] Vecchione R,et al. Electro-drawn drug-loaded biodegradable polymer microneedles as a viable route to hypodermic injection. Adv Funct Mater 2014; 24(23):3515–23.

[96] Grimaldi IA, et al. Graded-size microlens array by the pyro- electro hydrodynamic continuous printing method. Appl Opt 2013; 52 (32):7699–705.

[97] Miccio L,et al. Light induced patterning of poly(dimethylsiloxane) micro-structures. Opt Express 2010; 18(11):10947–55.

[98] L. Miccio, V. Marchesano, M. Mugnano, S. Grilli, and P. Ferraro, “Light induced DEP for immobilizing and orienting Escherichia coli bacteria,” Opt. Lasers Eng., vol. 76, pp. 34–39, 2014.

[99] Arizmendi L. Photonic applications of lithium niobate crystals. Phys Status Solidi A 2004; 201(2):253–83.

[100] Burgos H, et al. Role of particle anisotropy and deposition method on the patterning of nano-objects by the photovoltaic effect in LiNbO3. Opt Mater 2013; 35(9):1700–5.

[101] Esseling M, et al. Two-dimensional dielectrophoretic particle trapping in a hybridcrystal/PDMS-system. Opt Express 2010; 18(16):17404–11.

[102] Esseling M, et al. Charge sensor and particle trap based on z-cut lithium niobate. Appl Phys Lett 2013; 103(6):0611151–4.

[103] Blazquez-CastroA, et al. Tumour cell death induced by the bulk photovoltaic effect ofLiNbO3:Fe under visible light irradiation. Photochem Photo boil Sci 2011;10(6):956–63.

2.2 Optical multifunctional platform

2.1 Digital holography for cell imaging characterization

Nowadays, the imaging analysis of complex processes in living cells with light microscopy is important for many research areas in biology and medicine. This includes in particular the ranges of stem cell, development, and cancer sciences as well as the analysis of infection and inflammation processes.

For these reasons, there is a high demand for fast and label-free methods for online monitoring. Microscopic life cell imaging can give new insights and open revolutionary scenarios into cell motility, biomechanical properties on the cellular or subcellular level, and the response of cells to drugs and toxins. In order to affect the living specimen under investigation as little as possible, ideal imaging methods for the investigation of life cell processes should be minimally invasive. Moreover, quantitative measurement data should be provided.

Widely used fluorescence methods require specific labeling and are often restricted to chemically fixated samples. On a molecular level, live cell imaging aspects have been widely addressed by using a variety of fluorescence microscopy techniques [1,2]. These methods have been found highly suitable for 3D imaging of subcellular structures like, for example, the cell membrane, proteins of the cytoskeleton, mitochondria, or vesicles, with a resolution down to several nanometers [3,4]. However, although the specificity of fluorescence signals is high due to a large number of available dyes [5], specific auto fluorescence mechanisms [6], fluorescence lifetime imaging (FLIM) [7], and a wide experience with the techniques, there still remain challenges in the application of these methods for live cell imaging. For example, long-term in vitro investigations and *in vivo* applications are restricted as many fluorescence dyes are toxic. The engineering of fluorescent proteins like the green fluorescent protein (GFP) [8] allow extended investigations of living cells.

However, for this purpose cells have to be (genetically) modified, e.g., by chemical [9] or optical [10] transfection with the high risk to change the physiology of the

biological sample in analysis and to obtain some artefacts. Furthermore, in several cases, a low quantum efficiency of, for instance, the available dyes or the relevant auto fluorescence mechanisms results in the need for long exposure times or a high light intensity. This limits the temporal resolution and the application on living specimens. In this framework, methods that offer label-free and minimally invasive detection of live cell dynamics and cell state alterations are of particular interest. Thus, in the past years other label-free methods like Optical Coherence Tomography (OCT) [11, 12] and Coherent Amplified Raman Spectroscopy (CARS) [13] have been transferred to biomedical sciences. In addition, to make use of the high accuracy of diffraction and interferometry-based metrology, the activities of a growing number of research groups focus on techniques for quantitative phase imaging (QPI). QPI provides label-free data with low demands on light exposure and high data acquisition rates. As opposed to the above-mentioned fluorescence techniques, such methods detect changes of the optical path length (OPL) that are caused by the specimen under investigation.

Hai et al, were able to detect and quantify in a label-free high-throughput modality circulating melanoma tumor cell clusters using linear-array-based photoacoustic tomography approach (LA-PAT) [14]. Their data showed the capability of LA-PAT to detect and quantify melanoma CTC clusters in rat *in vivo* and showed its potential application in tumor metastasis study and cancer therapy. However, it is worth pointing out that currently LA-PAT detects only CTCs originating from primary tumors in which cells express melanin. Exploiting the strong optical absorption of melanin in the melanoma tumor cells, LA-PAT can achieve label-free detection of melanoma CTC clusters *in vivo*. By analyzing the contrast-to-noise-ratios (CNR) of the photoacoustic signals, this approach can quantify the number of cells in the CTC clusters and study their circulating kinetics in the bloodstream. To detect CTCs originating from amelanotic melanoma tumors, other tumor specific physiological properties, such as size and surface biomarkers, can be utilized. The quantification of CTC cluster sizes is indeed based on the assumption that the melanin content is relatively uniform in the tumor cells. LA-PAT has the potential to be a powerful tool for both preclinical tumor metastasis study, clinical cancer diagnosis and therapy. As a useful technique for researchers and scientists to better understand the relationship between CTCs and tumor metastasis. LA-PAT

can also be used by clinicians to monitor the changes of CTC concentrations in patients' circulatory systems and to evaluate the outcome of cancer therapy. In addition, photoacoustic imaging can measure other important biological parameters, including the oxygen saturation of hemoglobin, metabolic rate, and tumor stiffness [15-17].

This paragraph focuses on quantitative phase imaging with digital holographic microscopy (DHM). Holographic interferometric metrology is well established in industrial nondestructive testing and quality control [18–20].

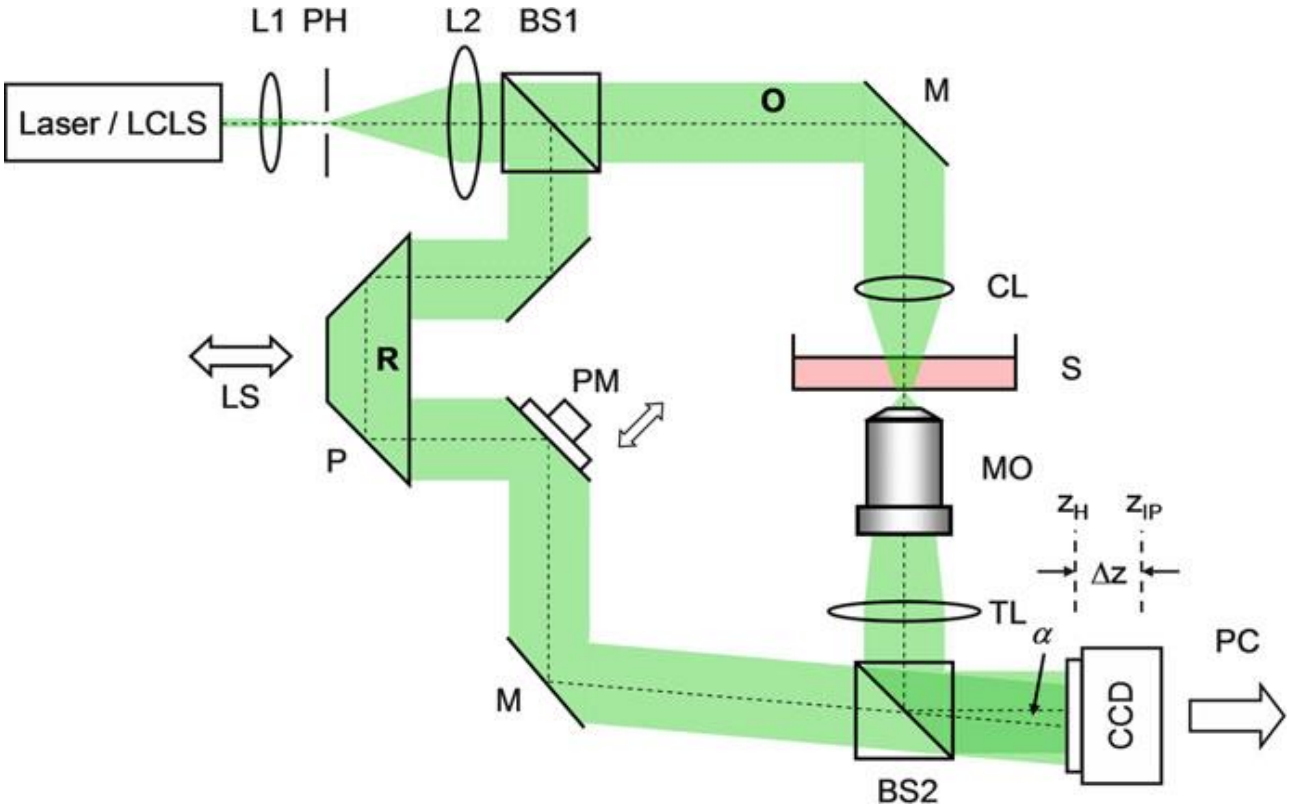

Figure 1: Mach-Zehnder setup for digital holographic microscopy in transmission mode. LCLS: low coherence light source; O: object wave; R: reference wave; α: phase gradient between O and R; M: mirror; BS1, BS2: non-polarizing beam splitter cubes; CL: condenser lens; MO: microscope lens; CCD: hologram recording device (CCD image sensor); L1, L2: lenses; PM: piezo actuated mirror; P: Porro prism; LS: motorized linear translation stage; PH: pin-hole aperture (spatial filter); TL: tube lens; Δz: distance between the hologram plane at $z = z_H$ and the image plane at $z = z_{IP}$; S: sample; PC: computer [43,44].

In combination with microscopy, digital holography provides label-free, quantitative phase imaging [21–26] that is also suitable for modular integration

into common research microscopes [27]. In this way, DHM facilitates a combination with other microscopy techniques like laser scanning microscopy, fluorescence imaging, and optical laser micromanipulation [28–30]. The reconstruction of digitally captured holograms is performed numerically. Thus, in comparison with other phase contrast methods [31, 32], related interferometry-based techniques [33–36], and optical coherence tomography or microscopy (OCM) [37–42], DHM provides quantitative phase contrast with subsequent numerical focus correction (multi-focus imaging) from a single recorded hologram.

In Figure 1 is depicted the principle of a Mach-Zehnder-based digital holographic microscopy setup [45]. The shown transmission mode setup enables investigations on transparent samples such as living cell cultures. The emitted light of a laser (e.g., a frequency doubled Nd:YAG, λ = 532 nm) or a low-coherence light source LCLS (e.g., a light emitting diode (LED) or a superluminescence diode (SLD)) is spatially filtered (L1, PH), collimated (L), and divided into an object illumination wave (O) and a reference wave (R). The intensity ratio between O and R is adjusted by adequately chosen optical density filters (not shown) or, alternatively, by substituting BS1 by a polarizing beam splitter cube in combination with two $\lambda/2$-wave plates. A condenser lens (CL) provides an optimized illumination of the sample. The reference wave is guided directly by a beam splitter to the image recording device (typically a charge coupled device sensor, CCD), which is applied for the digitization of the holograms in the hologram plane located at $z = z_H$. Holographic off-axis geometry is achieved by a phase gradient of the reference wave front relative to the object wave front, which can be performed by a slight tilt of a mirror (see angle α in Fig. 1) or by the beam splitter BS2. The adjustment of the optical path length difference for the LCLS can be performed by a Porro prism that is mounted onto a translation stage. For temporal phase shifting-based digital holographic reconstruction, a calibrated piezo-actuated mirror (PM) is applied. To enhance the lateral resolution, the object wave is magnified by a microscope lens (MO). The digital holograms are recorded with a digital image recording device and transferred to a computer (PC). The piezo-actuated mirror PM and the translation stage are synchronized with the hologram acquisition by a digital interface. The potentials of multi-focus DHM quantitative phase imaging are illustrated by selected applications.

DHM technique has many applications, it is shown that DHM is suitable for automated tracking of migrating cells and cell thickness monitoring as well as for refractive index determination of cells and particles.
Moreover, the use of DHM for label-free flow analysis in fluidics and for micro-injection monitoring is demonstrated. The results prove that DHM is highly relevant to achieve novel insights in dynamic cell biology, in cancer research, and in drugs and toxicity testing.

2.2 Set-Up of Holographic OT, DH and fluorescent moduli

Optofluidics is the use of light to control the flow of fluids, particularly at the micrometre scale. A notable application of this technology is in so-called lab-on-a-chip devices: miniature systems for analysing and sorting particles and cells. Optofluidics also uses liquids to guide the flow of light.
The optofluidic platform from our laboratory is depicted in fig. 2. Concerning the holographic optical tweezers modulus, the infrared (IR) trapping laser emitted at 1064 nm, the beam was expanded to fit the aperture of a Spatial Light Modulator or SLM (Holoeye - PLUTO-NIR phase only) operating in reflection mode. Then, the laser beam was injected into a Microscope Objective MO (100x N.A.=1.2) through a standard 4f optical configuration.
The sample was positioned beyond the MO in a temperature and CO_2 controlled chamber. By HOT, we trapped and manipulated biological samples but also micrometer latex beads in order to anchor them to suspended cells. Doing so, the optical forces were exerted on the microspheres, thus avoiding the direct interaction of the laser beam with cells. Specifically, by functionalizing the microbeads with Arginine–Glycine–Aspartic acid (RGD) peptides, we gave the cell n points of adhesion and stimulation (where n is the number of HOT trapped microbeads) – this point is described in details in chapter 4. Then the cell had the chance to assemble its cytoskeleton and react to mechanical stimuli applied by HOT. For our purposes we designed trapping sites able to trap polystyrene beads 8 μm-sized. A fiber-coupled, solid state laser emitting at 532 nm was used to build

the Mach-Zehnder interferometer, allowing recording a sequence of digital holograms of the sample during the experiment (light green path in Figure 2 (a)). From these sequences we reconstructed the Quantitative Phase Maps (QPMs) of the samples.

The third part of the setup is the fluorescence modulus for control studies. Light from a fluorescence lamp (X-cite series 120pc Lumen Dynamics) was directed on the sample with a combination of excitation and emission (Tritc) filters, suited for the fluorophore used in the experiment. All images were recorded with an USB U-Eye Camera (from IDS), 1280x1024 pixels (pixel size 5.3 µm), recording at 25fps.

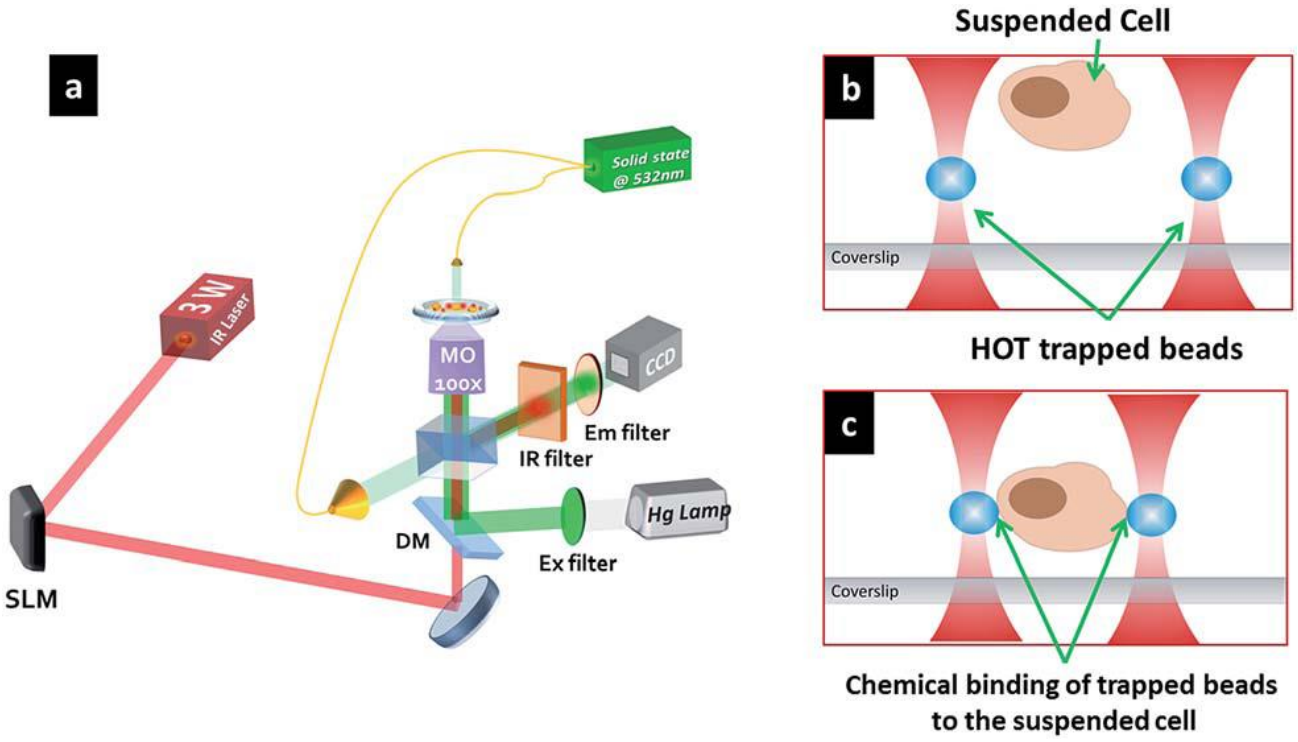

Figure 2: (a) Experimental setup made of HOT, DH and fluorescence moduli. Design of the experiment: one or more beads are optically trapped (b) and attached to a single floating fibroblast (c).

References

[1] E.M. Goldys (ed.), Fluorescence Applications in Biotechnology and the Life Sciences (Wiley-Blackwell, New-Jersey, 2009)

[2] V. Ntziachristos, Fluorescence molecular imaging. Annu. Rev. Biomed. Eng. 8, 1–33 (2006)

[3] L. Schermelleh, R. Heintzmann, H. Leonhardt, A guide to super-resolution fluorescence microscopy. J. Cell Biol. 190, 165–175 (2010)

[4] B. Huang, M. Bates, X. Zhuang, Super-resolution fluorescence microscopy. Annu. Rev. Biochem. 78, 993–1016 (2009)

[5] The Molecular Probes® Handbook, 11th edn. (2011). www.invitrogen.com

[6] M. Monici, Cell and tissue autofluorescence research and diagnostic applications, in Biotechnology Annual Review, ed. by M.R. El-Gewely (Elsevier, Amsterdam, 2005), pp. 227–256

[7] C.W. Chang, D. Sud, M.A. Mycek, Fluorescence lifetime imaging microscopy. Methods Cell Biol. 81, 495–524 (2007)

[8] O. Shimomura, The discovery of aequorin and green fluorescent protein. J. Microsc. 217, 3–15 (2005)

[9] P.L. Felgner et al., Lipofection: a highly efficient, lipid-mediated DNA-transfection procedure. Proc. Natl. Acad. Sci. U.S.A. 84, 7413–7417 (1987)

[10] X. Tsampoula et al., Fibre based cellular transfection. Opt. Express 16, 17007–17013 (2008)

[11] A.F. Fercher, Optical coherence tomography. J. Biomed. Opt. 1, 157–173 (1996)

[12] W. Drexler, Ultrahigh-resolution optical coherence tomography. J. Biomed. Opt. 9, 47–74 (2004)

[13] L.G. Rodriguez, S.J. Lockett, G.R. Holtom, Coherent anti-stokes raman scattering microscopy: a biological review. Cytometry A 69, 779–791 (2006)

[14] Pengfei Hai, Yong Zhou, Ruiying Zhang, Jun Ma, Yang Li, Jin-Yu Shao, and Lihong V. Wang, Label-free high-throughput detection and quantification of circulating tumor cell clusters by linear-array-based photoacoustic tomography. Journal of Biomedical Optics 22(4), 041004, 2017

[15] G. P. Luke and S. Y. Emelianov, Label-free detection of lymph node metastases with US-guided functional photoacoustic imaging, Radiology 277(2), 435-442, 2015

[16] Y. Fong et al., Breast-cancer-secreted miR-122 reprograms glucose metabolism in premetastatic niche to promote metastasis, Nat. Cell Biol., 17(2), 183-194, 2015

[17] J. Fenner et al., Macroscopic stiffness of breast tumors predicts metastasis, Sci Rep. 4, 5512, 2014

[18] T. Kreis, in Holographic Interferometry: Principles and Methods, ed. by W. Osten, vol. 1 (Akademie-Verlag, Berlin, 1996)

[19] V.P. Shchepinov, V.S. Pisarev, Strain and Stress Analysis by Holographic and Speckle Interferometry (Wiley, New York, 1996)

[20] M.-A. Beeck, W. Hentschel, Laser metrology – a diagnostic tool in automotive development processes. Opt. Lasers Eng. 34, 101–120 2000

[21] E. Cuche, P. Marquet, C. Depeursinge, Simultaneous amplitude-contrast and quantitative phase-contrast microscopy by numerical reconstruction of Fresnel off-axis holograms. Appl. Opt. 38(24), 6694–7001, 1999

[22] F. Charrie`re et al., Characterization of microlenses by digital holographic microscopy. Appl. Opt. 45, 829–835, 2006

[23] D. Carl et al., Parameter-optimized digital holographic microscope for high-resolution living-cell analysis. Appl. Opt. 43, 6536–6544, 2004

[24] P. Marquet et al., Digital holographic microscopy: a noninvasive contrast imaging technique allowing quantitative visualization of living cells with subwavelength axial accuracy. Opt. Lett. 30, 468–470, 2005

[25] C.J. Mann et al., High-resolution quantitative phase-contrast microscopy by digital holography. Opt. Express 13, 8693–8698, 2005

[26] B. Kemper, G. von Bally, Digital holographic microscopy for live cell applications and technical inspection. Appl. Opt. 47, A52–A61, 2008

[27] B. Kemper et al., Modular digital holographic microscopy system for marker free quantitative phase contrast imaging of living cells. Proc. SPIE 6191, 61910T, 2006

[28] G. von Bally et al., New methods for marker-free live cell and tumor analyis, in Biophotonics: Vision for Better Healthcare, ed. by J. Popp, M. Strehle (Wiley, Berlin, pp. 301–360, 2006

[29] B. Kemper et al., Monitoring of laser micromanipulated optically trapped cells by digital holographic microscopy. J. Biophoton. 3, 425–431, 2010

[30] M. Esseling et al., Multimodal biophotonic workstation for live cell analysis. J. Biophoton. 5, 9–13, 2012

[31] L.G. Alexopoulos, G.R. Erickson, F. Guilak, A method for quantifying cell size from differential interference contrast images: validation and application to osmotically stressed chondrocytes. J. Microsc. 205, 125–135, 2001

[32] A. Barty et al., Quantitative optical phase microscopy. Opt. Lett. 23(11), 817–819, 1998

[33] J. Farinas, A.S. Verkman, Cell volume and plasma membrane osmotic water permeability in epithelial cell layers measured by interferometry. Biophys. J. 71, 3511–3522, 1996

[34] T. Ikeda et al., Hilbert phase microscopy for investigating fast dynamics in transparent systems. Opt. Lett. 30(10), 1165–1167, 2005

[35] G. Popescu et al., Fourier phase microscopy for investigation of biological structures and dynamics. Opt. Lett. 29, 2503–2505, 2004

[36] V.P. Tychinskii, Coherent phase microscopy of intracellular processes. Phys. Usp. 44, 617–629, 2001

[37] A.D. Aguirre et al., High-resolution optical coherence microscopy for high-speed, in vivo cellular imaging. Opt. Lett. 28, 2064–2066, 2003

[38] E.A. Swanson et al., In vivo retinal imaging by optical coherence tomography. Opt. Lett. 18, 1864–1866, 1993

[39] Y. Zhao et al., Real-time phase-resolved functional optical coherence tomography by use of optical Hilbert transformation. Opt. Lett. 27, 98–100, 2002

[40] C.G. Rylander et al., Quantitative phase-contrast imaging of cells with phase-sensitive optical coherence microscopy. Opt. Lett. 29(13), 1509–1511, 2004

[41] A.K. Ellerbee, T.L. Reazzo, J.A. Izatt, Investigating nanoscale cellular dynamics with crosssectional spectral domain phase microscopy. Opt. Express 15, 8115–8124, 2007

[42] C. Joo, K.H. Kim, J.F. de Boer, Spectral-domain optical coherence phase and multiphoton microscopy. Opt. Lett. 32, 623–625, 2007

[43] P. Langehanenberg, G. von Bally, B. Kemper, Application of partial coherent light in live cell imaging with digital holographic microscopy. J. Mod. Opt. 57, 709–717, 2010

[44] B. Kemper, P. Langehanenberg, S. Kosmeier, F. Schlichthaber, C. Remmersmann, G. von Bally, C. Rommel, C. Dierker, and J. Schnekenburger, Digital Holographic Microscopy: Quantitative Phase Imaging and Applications in Live Cell Analysis, Handbook of Coherent-Domain Optical Methods, DOI 10.1007/978-1-4614-5176-1_6, Springer Science+Business Media New York 2013

[45] P. Langehanenberg, G. von Bally, B. Kemper, Application of partial coherent light in live cell imaging with digital holographic microscopy. J. Mod. Opt. 57, 709–717, 2010

3 Quantitative phase imaging for cell analysis: 3D shape and dynamics

3.1 Lab-on-chip analysis of biological samples

Today, fast and accurate diagnosis through portable and cheap devices is in high demand for the general healthcare. Lab-on-chips have undergone a great growth in this direction, supported by optical imaging techniques more and more refined [1]. A LoC device is a pocket platform consisting in microfluidic channels designed in order to form more or less complex circuits.

The LoC paradigm can be resumed in the will to emulate all the functionalities of a modern analysis lab on-board a portable device, realizable at contained costs. In particular, it has become more and more apparent as the study of biological samples can benefit from the use of a LoC environment. Thus, the typical behaviour of a cell, e.g. the growth rate, duplication, migration, adhesion to substrates, mechanical interactions with the extracellular matrix and other cells, reaction to drugs, and death, strongly depends on the 3D shape and composition of its surrounding environment.

A LoC is nowadays the most appropriate site to recreate the cellular environment and mimic all the external cues and forces affecting the cell behaviour, taking advantage from the microfluidic flow control, as well as the miniaturization of components like valves, pumps, mixers and sorters. These features make a LoC extremely promising as a novel device to embed diagnostics tools to be used at the point-of-care, allowing first screenings or accurate analysis in absence of adequate facilities and with untrained personal, e.g. in developing countries and low-resource settings.

Recent progresses in developing imaging tools based on quantitative phase imaging can be very useful when applied into biomicrofluidics. In some cases, the optical tweezers technique is combined with digital holography (DH), thus offering the possibility to manipulate, analyze, and measure fundamental parameters of

different kinds of cells. This approach can open the route for rapid and high-throughput analysis in label-free microfluidic devices and for an early diagnosis and prognostic based on cell examination, thus allowing advancements in biomedical science.

3.1.1 Red blood cells as optofluidic microlens

Recent discoveries about the optical properties of red blood cells (RBCs) and the perspective of using them as liquid micro-lenses can now be used to explain, and may eventually be used to predict erythrocyte shape and to screen for blood disease [2].

Nowadays, blood smear test represents a simple and cheap method to estimate the morphology of blood components and to achieve qualitative information regarding the red cell hemoglobinization. Although blood smear is an important analysis for blood disorders, it provides two dimensional morphometric values of cells and it is related to the subjective expertise of the doctor, this could mislead regarding the real shape of red blood cells. Thanks to the elastic properties of the plasmatic membrane, the RBCs can swell up and wrinkle by changing the osmotic conditions of the medium in which they are suspended, thereby varying focal length from negative to positive values.

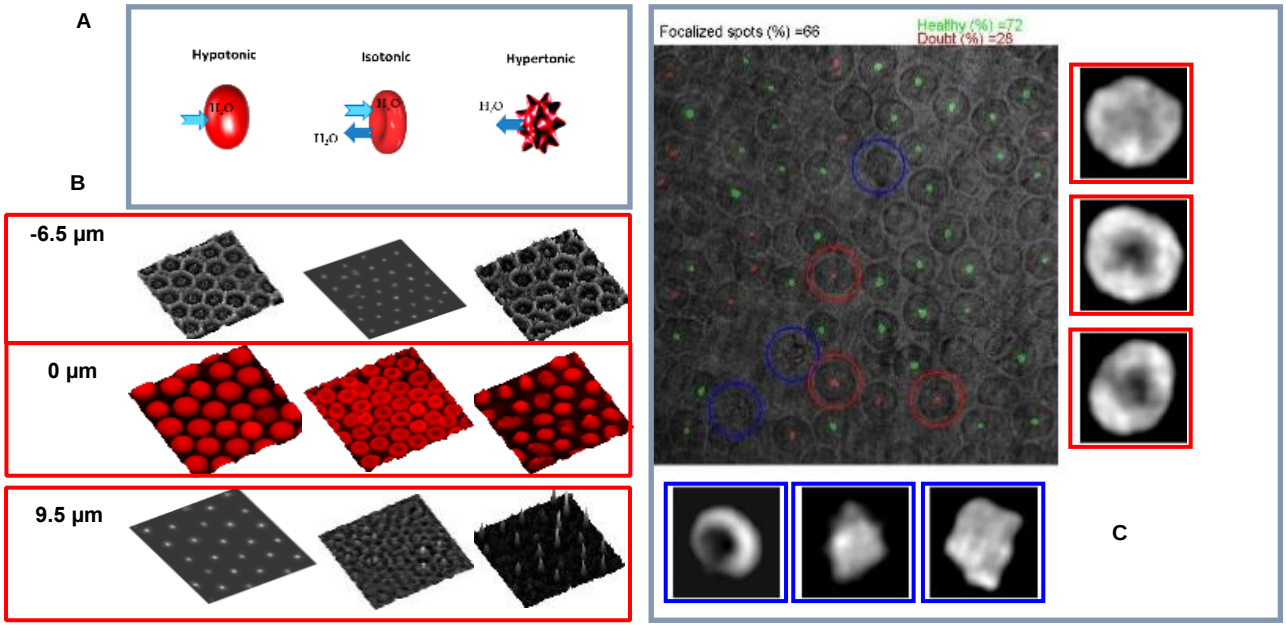

Figure 1: RBC pre-screening process.

Blood diagnosis is demonstrated by screening abnormal cells through focal-spot analysis applied to an RBC ensemble as a micro-lens array (Figure 1).

When RBCs are in different solutions (hypotonic, isotonic and hypertonic), cross-membrane water exchange modifies cell shape, from a disk volume of 90 fl to a spherical volume of 150 fl and vice versa, depending on salt concentration of the medium (Figure 1a).

The innovative diagnostic aspect is demonstrated in Fig. 1b, by analyzing the intensity spots in the virtual focus plane (z= -6.33μm). In the second row of Fig. 1b is shown the quantitative phase map reconstructions of the three samples of (1A); while in the first and in the third rows is reported the intensity reconstructions in the planes at -6.5μm and 9.5μm from the RBC, respectively. It is simple to establish that the isotonic sample presents several healthy RBCs due to their focalization in the "virtual" plane, while the other two samples don't focalize in such a plane.

A real-time RBC diagnosis, as depicted in Fig. 1c, is performed by analyzing the focalizing spots of each of them. Healthy discocyte correspond to a quasi-circular intensity spot (green); red spots correspond to doubtful cases. The distinction between healthy and doubtful is obtained by evaluating the ratio between minor and mayor axes of a best-fit ellipse of each spot (ellipticity). In the case of healthy discocyte RBCs, a suitable intensity pattern of the spots is observed in the plane at -6.5μm (green spots), while when RBC shape is deformed (blue circles), the corresponding focus spot presents a different form with respect to the "healthy" one. Red spots correspond to ambiguous cases because the cells focalize but the spots are not uniform. In the blue and red frames, QPMs corresponding to blue and red circles are respectively shown.

Thanks to this new and revolutionary discovery regarding the possibility of using red blood cells as lenses, we have reveal a fast in-line cyto-tomographic method for full characterization of erythrocytes operating in a microfluidic channel at lab-on-a-chip scale. Whereas RBCs are flowing and rolling along a micro channel, each tomogram can be obtained without any *a priori* knowledge of the rotation angle of the cell that instead is retrieved from its focusing properties.

In the next paragraph we will demonstrate an accurate and complete 3D classification of RBCs thus adding a new label-free diagnostic tool for fast blood analysis and effective disease screening. Thanks to the possibility of using red

blood cells as lenses, it was possible to easily detect blood disorders involving shape abnormalities, for example, sickle-cell disease, spherocytosis, elliptocytosis by screening abnormal cells through focal-spot analysis applied to an RBC ensemble as a microlens array.
Moreover, it is expected that the device for such a diagnostic tool – well described in the section 2 - could be adapted at lab-on-chip scale, because the optical set-up is very easy as it uses only a camera and a laser light source in the visible range that indeed nowadays are very compact and of low cost.

3.2 Tomographic flow cytometry by DHM

The working conditions and the adopted optical system are depicted in Fig. 2(a). Cells tumble while flowing along a microfluidic chip probed by a single fixed laser beam. A second beam is used as a reference to generate interference fringes on the CCD camera. More details regarding the optical setup are given in ref [3].
Hundreds of cells per minute have been analysed and, for each one, hologram's sequence is recorded and the corresponding QPMs retrieved. Firstly, 3D holographic tracking is performed to re-align each cell with respect to its centre of mass [4-6]. Then, rotation angles are numerically estimated by using two strategies, depending on the kind of the cell under analysis. In Fig.2(b) we report the conceptual block diagram resuming the main steps of the two proposed strategies. Finally, we use the optical projection tomography method to calculate the 3D refractive index distribution of the sample [7]. Complete proofs of both mathematical relationships for angles retrieving are reported in Supplementary Information of ref [3] together with the holographic 3D tracking algorithm

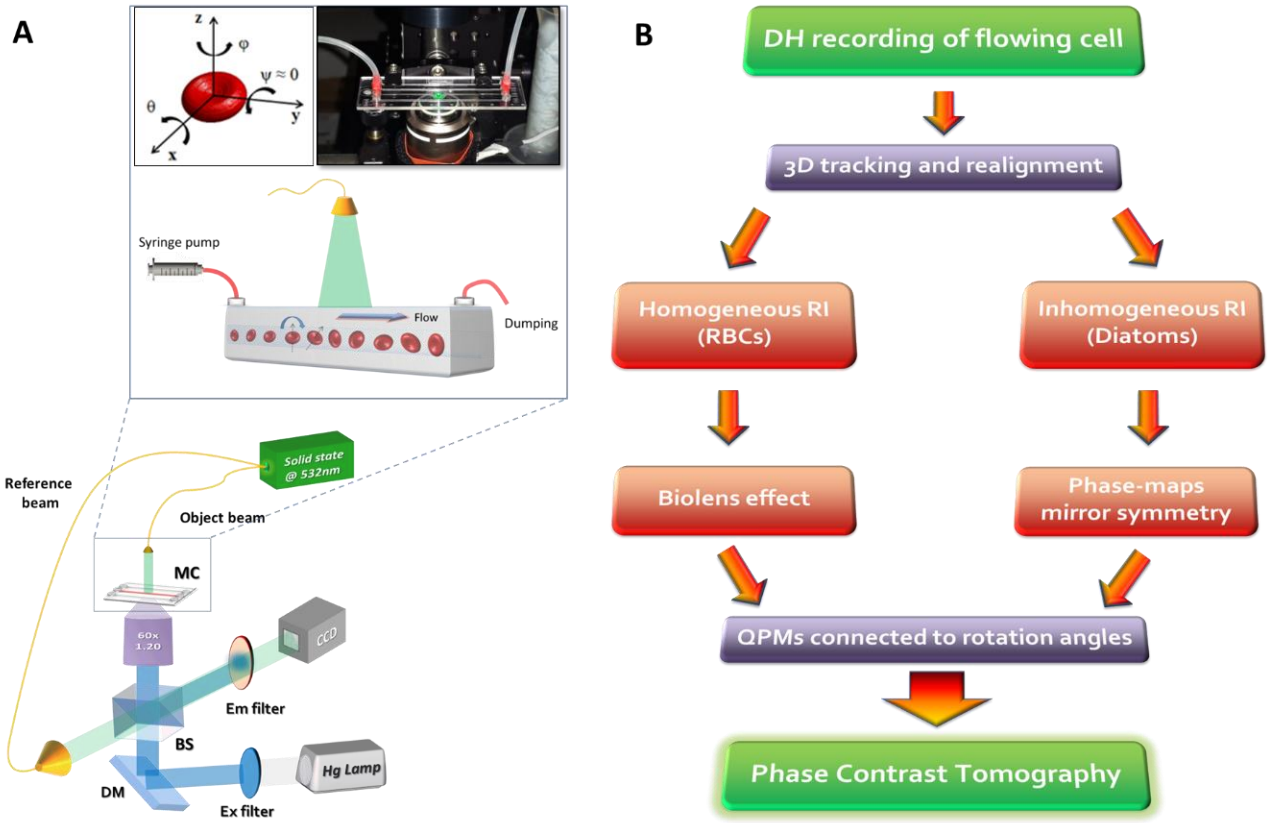

Figure 2: Working principles of R-TPM paradigm. (a) Sketch of the experimental R-TPM set-up. Cells are injected into a microfluidic channel and tumble when flowing along their path (inset of (a)). At the same time, a holographic image sequence is acquired. In the top-left corner of the inset the reference system for cell tumbling is reported, while in the top-right corner a photo of the real setup is shown. (b) Flow chart representing the main steps of the two proposed algorithms for angle recovery and tomographic reconstruction [ref. 3].

3.2.1 Cyto-tomography as a diagnostic tool in haematological disorders

Results of Rolling-Tomographic Phase Microscopy (R-TPM) applied on RBCs, are reported in Fig. 3. There, four interesting cases are revealed. In particular, we have examined both healthy (Fig.3 (a,b)) and pathological (Fig.3 (c,d)) RBCs such as iron-deficiency anemia and thalassemia, that are two highly diffused blood

disorders. Specifically, some of QPMs with the corresponding measured angles are illustrated on the top row of each sub-Figure 3. The inner plots show the rotating angle recovery approach.

The final cyto-tomography results are displayed on the bottom side together with a picture of the correspondent central slices (z=0 and y=0 planes). In addition, insets red boxes report a plastic model obtained by a 3D printer for educational purposes. In particular, we report the complete 3D RI distribution and the inner RI map corresponding to the hemoglobin distribution. Figure 3 a) shows an abnormal RBC detected in the healthy sample, an one-side concavity is present resembling the shape typically observed in the hereditary stomatocytosis. Figure 3b) reports one of the RBCs analyzed for the healthy sample in hypertonic solution, where the shape modification, induced by the medium, provides typical burr shape. We compare real cases with the simulated one (see Supplementary Information ref. 3) by means of the healthiness parameter, *H*, that is the correlation coefficient between the measured and ideal 3D RI distributions. We assume that for $0.9 \leq H \leq 1$ a RBC can be considered normal, otherwise deviation from discocyte shape is not negligible. *H* values are reported for all the cases presented in Fig.3 together with other global morphometric parameters, namely the Average RI (ARI), the bio-volume (V), and the corpuscular hemoglobin (CH).

In order to verify the correctness of the proposed approach, we have tested the R-QPM for two highly diffused blood disorders.

The first sample, represented in Fig.3(c), is from a patient affected with an iron refractory iron deficiency anemia (IRIDA) due to mutations in TMPRSS6 gene (L63Pfs13- W590R in compound heterozygosity) [8].

The second sample, in Fig. 3(d), is from a patient affected with alpha-thalassemia due to a heterozygous deletional event of both in-cisHBA1 genes (--CAMPANIA in heterozygosity) [9]. Complete Blood Count (CBC) reveals that mean corpuscular volume (MCVs) are equal to 62.6 and 67.5 fL, and MCHs are 18.5 and 21pg, respectively. (Analysis performed by DAI.Med.Lab AOU Federico II University, Naples).

In case of anemia due to an inherited defect in iron metabolism and Thalassemia, CH and V values are in good agreement with the analysis reported in literature and by comparison with CBC from patients with similar genotype [8-10].

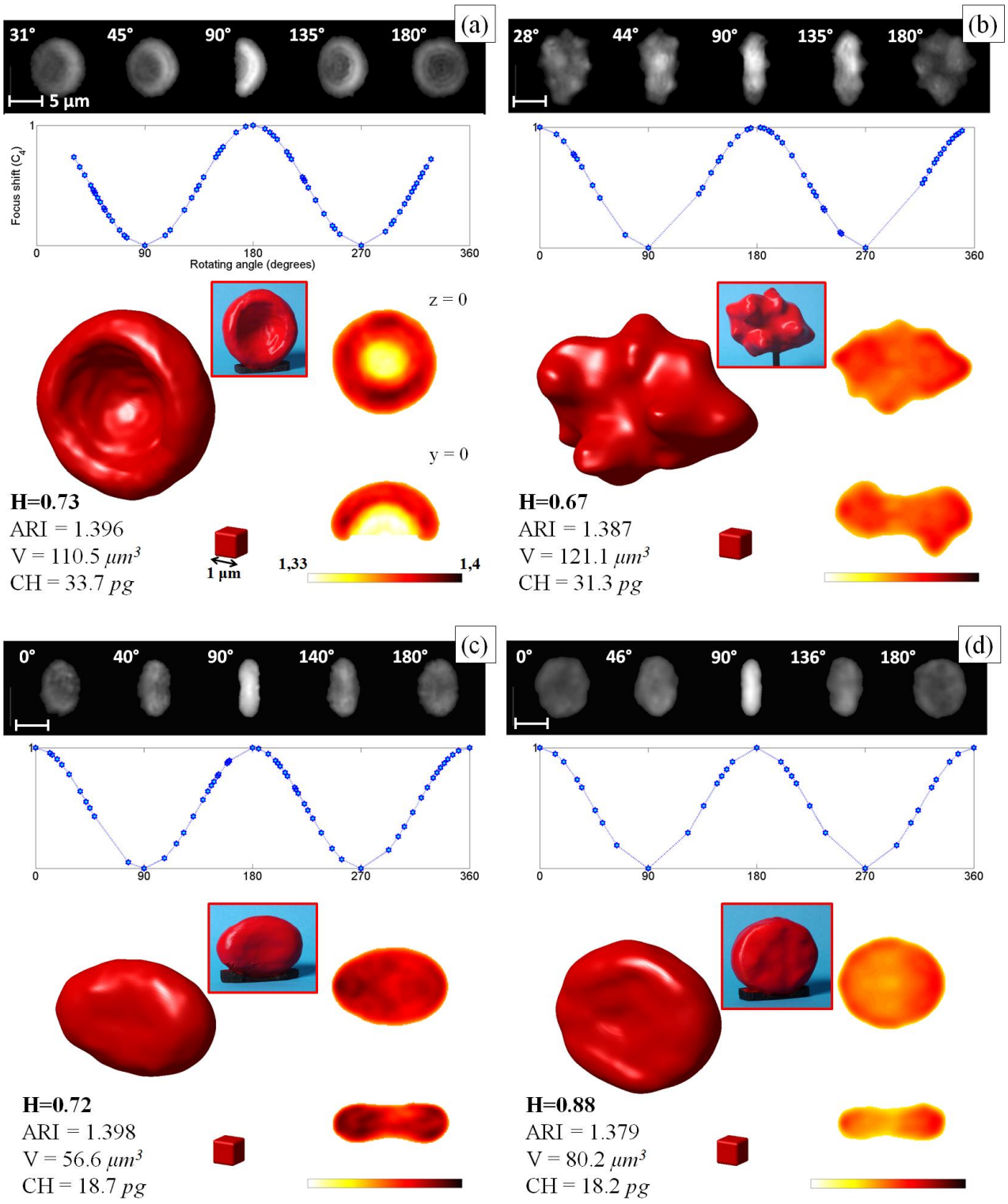

Figure 3: R-TPM for RBCs. (a-d) Results of R-TPM, applied on RBCs presenting morphological anomalies (H<0.9) with respect to the ideal healthy one: (a) one-side concavity, (b) speculated, (c) iron-deficiency anemic and (d) thalassemic RBC. For each of them we report the QPIs and the mathematical dependence of the defocus coefficient from the rotation angle, the tomogram retrieved by the QPIs and the RI distributions at z=0 and y=0 planes. ARI, V and CH are also reported together with plastic 3D representations realized by a 3D printer [ref. 3].

3.3 Cell dynamics studies by digital holographic microscopy

In recent years, the digital holography in microscopy configuration has been proved to be suitable for bio physics experiments to evaluate quantitatively forces, positions and biovolumes [11–17].

Different works have been published in the last few years where DH is used for investigating the variations of cell morphology under *in-vitro* invasive stimulations. Pavillon et al. used DH for monitoring the transient swelling phenomena occurring in neuronal cells when stimulated by glutamate applications, but without leading to death [18]. A couple of works used DH for measuring the temporal evolution of cell volume changes during cell death induced by chemical treatments: neuronal cells stressed by glutamate overdoses [19] and human epithelial cells stimulated by staurosporine [20].

More recently Wingren's group proposed DH for monitoring morphologically cell cycle arrest and death under specific chemical treatments, but without real time information about the cell volume changes during death [21–22].

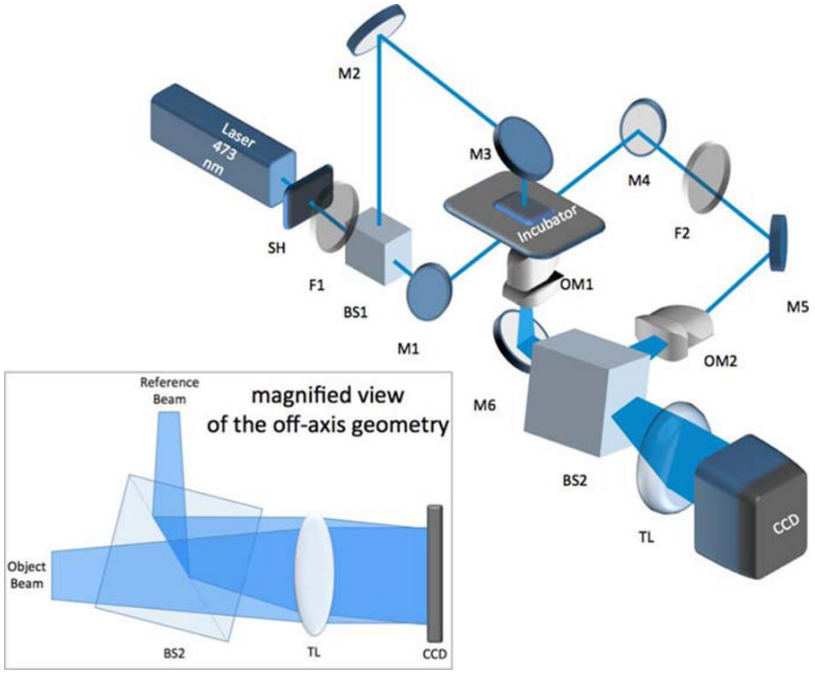

Figure 4: Schematic view of the DH set-up. SH, shutter; F, filters; BS, beam-splitters; M, mirrors; OM, optical microscope objectives (long working distance, Nikon Plan Fluor 20×, N.A. = 0.5); TL, tube lens (focal length 350 mm) [ref. 23].

3.3.1 Cell death characterization induced by blue light

Here we propose an innovative DH configuration (Fig.4) able to monitor the cell dynamics and volume variations induced by blue light exposure at different cell adhesion stages, thus giving quantitative information about the cell death pathways occurring under this kind of injurious stimulation. Figure 4 shows the off-axis DH set-up used for monitoring the cell volume changes during blue light exposure. It is the same optical set-up described above to perform the RBC tomogram but with some adjustments. It is based on a Mach-Zehnder interferometer mounted under transmssion configuration.

The beam exiting a CW laser diode (Melles Griot), emitting 5 mW @ 473 nm, has a diameter of 0.75 mm and is splitted by the beam-splitter BS1 into two beams called object and reference beams. The object beam is deviated vertically and redirected downward on the sample holder through the mirrors M2 and M3. The 20× microscope objective OM1 magnifies the sample image, while the beam splitter BS2 recombines the two beams and addresses the interference pattern onto the sensitive chip of a conventional CCD camera (1628 × 1236 pixels, 4.4 μm sized, JAI). The glass WillCo-dish (glass bottom dish, size 35 × 10 mm, WillCo Wells) with living cells is mounted into a conventional micro-incubator chamber (Warner Scientific) in order to maintain the appropriate temperature and atmosphere conditions (37 °C and air mixed at 5% CO_2). A small angle between the reference and the object beams is introduced to spatially separate the first order spectral components from the zero-order term to enable effective filtering in the Fourier domain. DH allowed us to retrieve the phase shift data Δφ arising from the difference in refractive index between the specimen and the surrounding medium [17, 19]:

$$\Delta\varphi(x,y) = \frac{2\pi}{\lambda}\,(nc - nm)\,h\,(x,y) \tag{1}$$

where λ is the laser wavelength, n_c is the mean cellular refractive index, n_m is the refractive index of the surrounding solution, and h is the cell height at position (x,

y) in the field of view. We considered, in the first approximation, n_c = 1.375 for the cellular refractive index [15] and n_m = 1.337 for the refractive index of the medium [14]. In the reconstructed images of the phase distribution we selected the areas belonging to the cells and we calculated the cell height h by Eq. (1). We calculated the volume above each pixel in these areas by multiplying the height h by the XY size of the pixel (px = 0.128 μm) and finally we retrieved the cell volume by summing the volumes above all of the pixels in the cell area.

The evolution of the cell volume was monitored in real time thanks to multiple image acquisitions and, in particular, was performed here during different stages of the cell adhesion. It is worth noting that the refractive index of the cell may be considered approximately the same during the experiment [20], thus allowing one to consider the volume change as the main contribution to the phase variations. As already mentioned in the first section, we use here for the first time a DH set-up with a blue laser source for cell morphology investigation, thus improving the spatial resolution, compared to traditional DH methods with red sources.

The operation conditions were controlled accurately in order to assess the threshold between what we call here safe exposure and injurious exposure (SE, IE), by evaluating the integrity of both cell body and membrane reconstructed by DH. In the first case, the best performance in terms of both DH reconstruction and cell integrity was obtained by using a laser power attenuated down to about 200 μW and an exposure window ΔT about 1 s long, in correspondence of which 1 hologram is acquired, at regular intervals ΔT of 150 s.

These parameters allowed us to exposure the cells up to 48 h without any significant damage onto the cell body, thus allowing us to inspect all of the typical adhesion stages of the cells from seeding till the early and the late adhesion stages (ESA and LSA). The SE was achieved by using a homemade programmable electronic system able to trigger appropriately the mechanical shutter and the CCD camera up to 48 h long operation. The IE consisted simply in switching the laser emission to continuous mode at about 4 mW. The SE conditions implied a dose of about 5×10^8 photons/$\mu m^2 \times s$, while the IE corresponded to about 10^{12} photons/$\mu m^2 \times s$. The IE was applied to both ESA and LSA, in order to investigate the cell volume evolution under two main different cell adhesion conditions.

The figure 5 shows the phase map evolution of live cells under SE from the ESA till the LSA. The cells appear clearly to spread completely onto the glass surface of a WillCo dish in a couple of hours, without any significant anomaly, thus demonstrating the non-invasive nature of the SE modality. Successively, another experiment was performed for monitoring the cell volume changes during IE in correspondence of the ESA. The laser source was switched on continuous wave (CW) just a few minutes after seeding the cells into the WillCo dish. The image acquisition started around 10 minutes after seeding and continued for about 9 hours with an acquisition rate of 0.4 frames/min, namely one frame every 150 s.

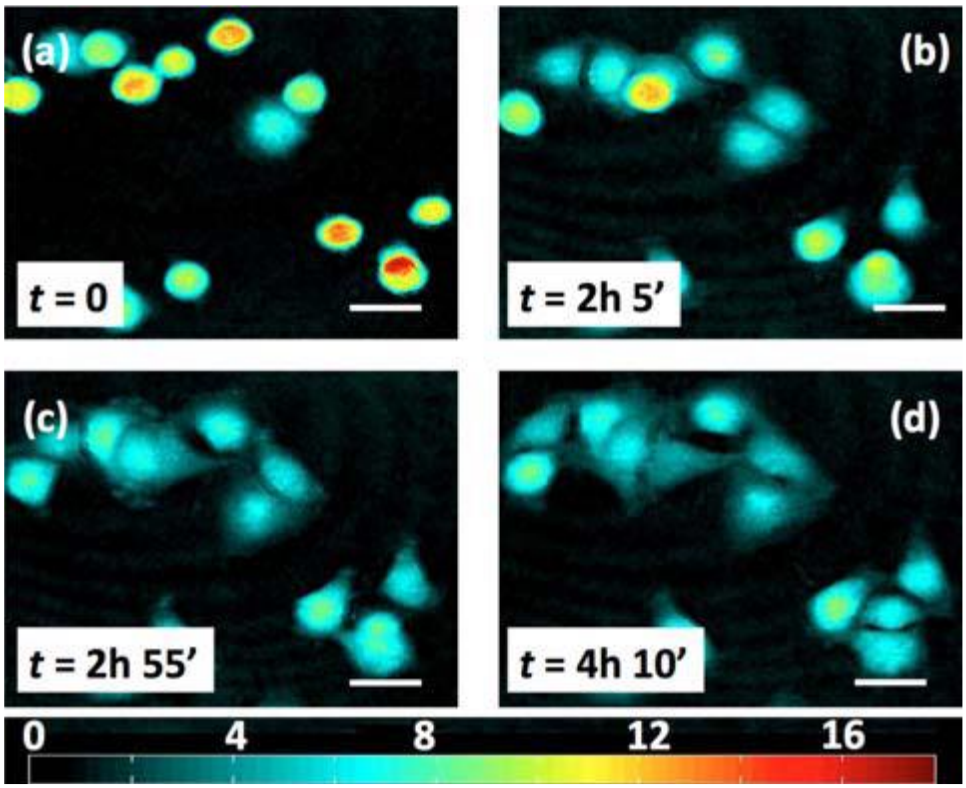

Fig. 5: Typical phase map images of live cells under SE at different time intervals. The scale bar is 20 μm. The colour bar corresponds to μm units [ref. 23].

The Figure 6 shows the typical phase map evolution of cells during IE. The phase images show clearly how the cells try to adhere to the substrate and, before spreading, exhibit a swelling effect with the formation of "balloon- like" and blebs structures, typical of necrotic cells.

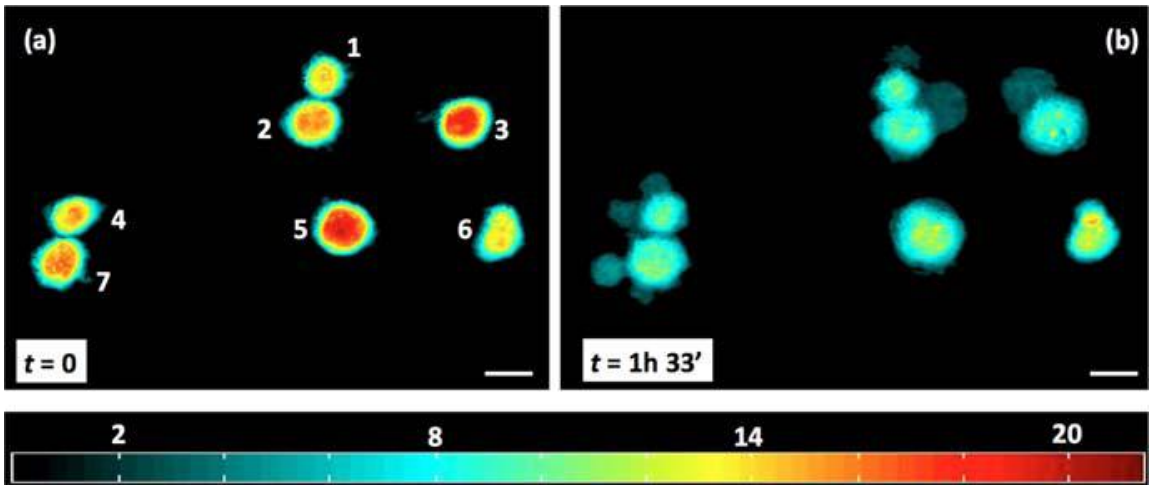

Fig. 6: Reconstructed phase map images of cells acquired under IE during ESA. The scale bar corresponds to 20 μm. The colour bar corresponds to μm units [ref.23].

Successively the cell membrane rupture occurs and the intracellular fluid flows out the cell body, with a consequent volume decrease. The volume was evaluated for each cell in Figure 6 and the corresponding temporal evolutions are shown in Figure 1 of the Supplementary Information of ref [23]. The experimental data of the cell volumes are represented by the dispersed dots and appear clearly distributed according to an elongated reversed S-shaped curve. Therefore, these data were fitted with the following sigmoidal function (SF) generated by the Boltzmann model (OriginLab):

$$V(t) = \boldsymbol{V_0} + \frac{\boldsymbol{V_f - V_0}}{\boldsymbol{1 + e^{(t - t_0)/\tau}}} \qquad (2)$$

where V_0 and V_f are the initial and final volume of the cell reconstructed through the corresponding phase maps, t_0 is the mean temporal point of the SF, namely the centre of the SF where the volume reaches the maximum value, and τ is the time constant. The volume data show clearly the volume increase of the cell before membrane rupture, typically occurring in necrosis. The variability of cell volume variation was due to the slight different adhesion stage in each cell. The R-squared results (see Table 1 in Supplementary Information of ref 23) show clearly that the

SF definitely fits well the volume data, thus providing a significant model for predicting the temporal evolution of the cell volume during light-induced necrosis. The same kind of experiment was performed onto another cell culture sample by magnifying digitally a single cell, in order to demonstrate the reliability of the technique and to observe more details about the single cell morphology. Figure 7 shows the typical temporal evolution of the reconstructed phase maps under 3D representation of a single cell during blue laser exposure on ESA.

The morphological changes experienced by the cell are clearly visible with high spatial resolution during the entire cell death process. The figure 1A) corresponds to the state in which the cell is alive just after seeding and observed under SE.

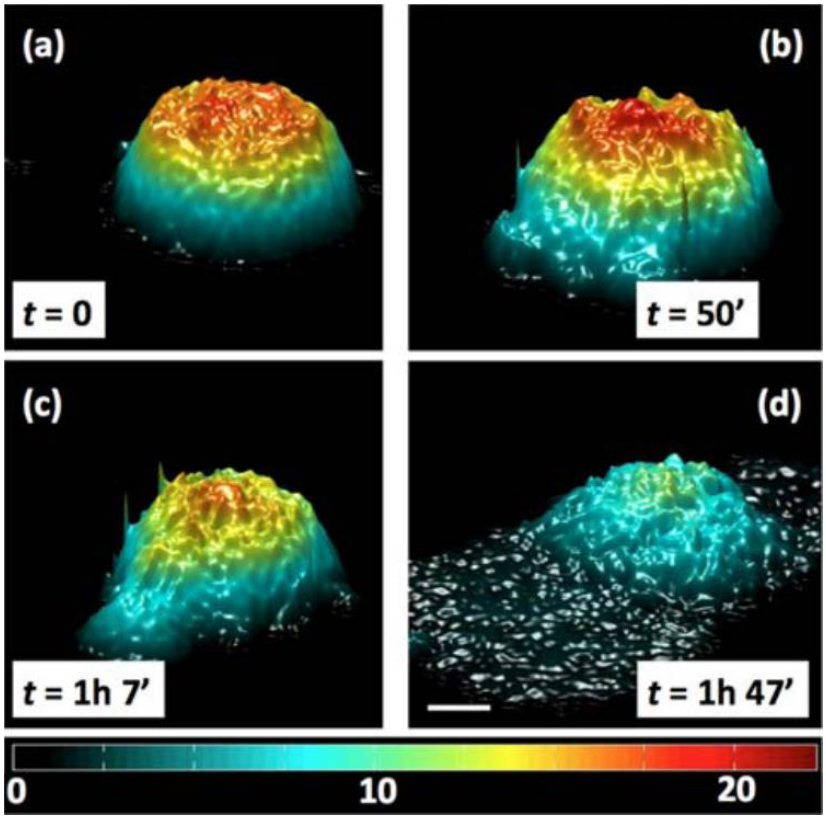

Fig. **7**: Temporal evolution of the reconstructed phase map under 3D representation in case of a single cell during ESA when subjected to IE. The scale bar is 6 µm. The colour bar corresponds to µm units [ref. 23].

The cell morphology appears stable and un-perturbated. Conversely, the cell motion and vibrations appear to rise significantly when switching to IE,

corresponding to the early stages of the necrosis, when the cell tries to regulate its volume desperately till death. In this case we evaluated the temporal evolution of both cell volume and cell area, and Figure 8 shows the corresponding results.

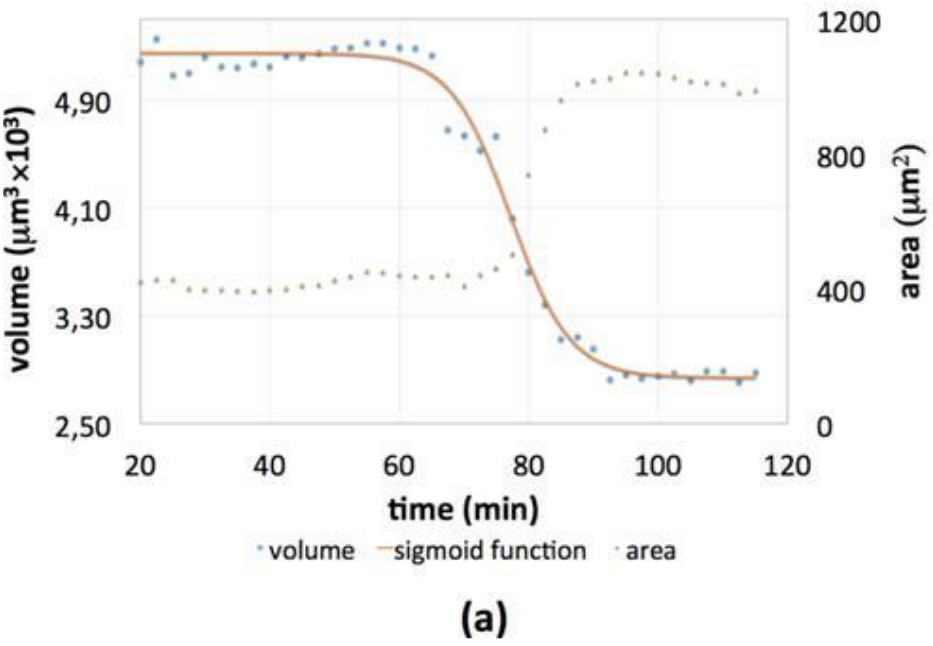

(a)

Fitting parameter	Value
V_0	5252
SD (V_0)	24
V_f	2842
SD (V_f)	39
ΔV (%)	32
t_0	77,2
SD (t_0)	0,5
τ	4,6
SD (τ)	0,4
R-square	0,99

(b)

Figure 8 (a) Temporal evolution of cell volume and area during ESA when subjected to IE. The data refer to the cell shown in Figure 7; (b) list of parameter values resulting from fitting the volume data with the sigmoid function [ref. 23].

The cell volume initially oscillates according to the regulatory mechanisms that compensate the physiogocial volume variations in order to maintain an appropriate balance of ions across their cell membrane. Then, the volume data exhibit the upward slope corresponding to the swelling just before the membrane rupture, while the area data arise correspondingly. The intracellular liquid flowed out of the cell, the volume dropped down rapidly by about 32%, following the SF behaviour. The blue light exposure was investigated also during the LSA by switching the DH modality from SE to IE after cell spreading onto the WillCo dish.

The Figure 9 show the temporal evolution of the reconstructed phase maps under 2D and 3D representation. The phase images clearly show how the spread cells release intracellular liquids with a consequent decrease of the volume.

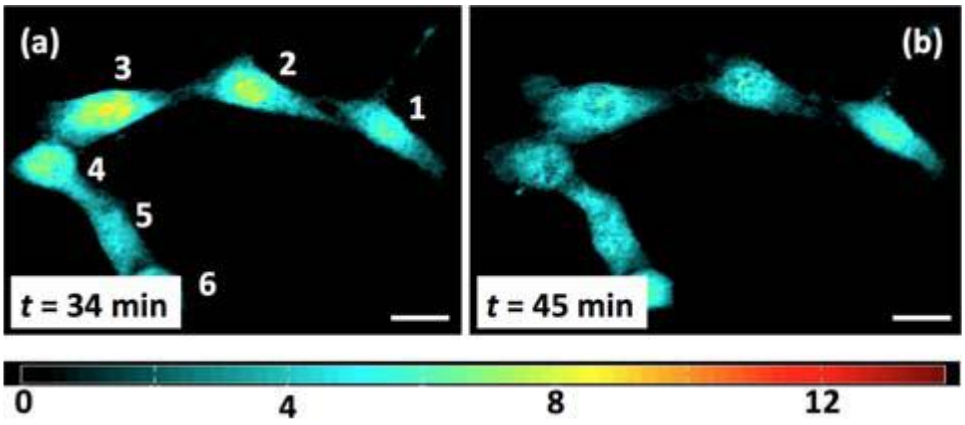

Fig. 9: Phase map images of cells under LSA during IE. The colour bar corresponds to μm units. The scale bar is 20 μm [ref. 23].

Figure 10 shows the phase maps reconstructed in case of LSA of more dense cells.

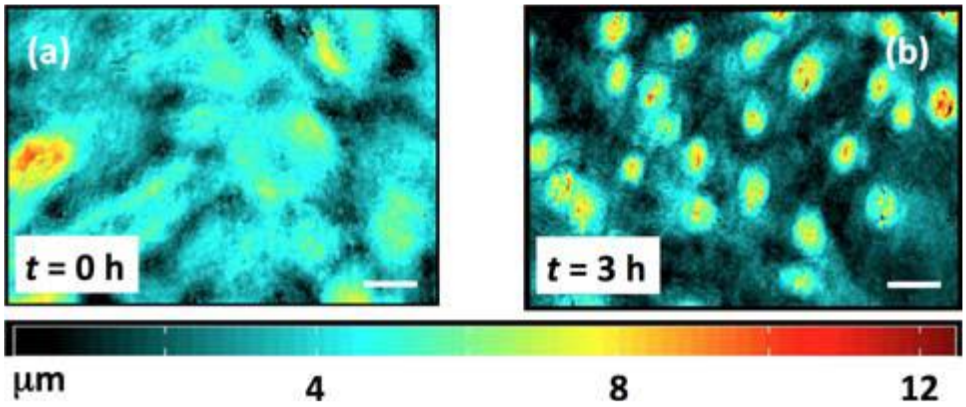

Fig. 10: Phase map images of cells under LSA during IE, in case of higher density. The colour bar corresponds to μm units. The scale bar is 20 μm [ref. 23].

In conclusion, we performed a novel quantitative study for investigating real time the cell volume changes during blue light exposure under both early and late adhesion of fibroblast cells. We adopted a holographic microscopy technique for obtaining quantitative data. Furthermore, we added an innovative approach if compared to the standard DH techniques as here for the first time we develop a DH set-up that uses a blue laser source that simultaneously serves as reading and tool for inducing phototoxicity, by switching the DH operation between what we call

here “safe” and “injurious” exposure. The results show that the cell morphology and volume evolve with characteristics that are typical of necrotic cells, with swelling, balloon-like structures and successive membrane rupture and leakage of intracellular liquids.

This technique allows one to extract information about the interaction of blue light with live adherent cells, establishing the threshold conditions between healthy and damaged cells. This study could open the route to further investigations on light induced mechanisms in living specimen and, thanks to the possibility of structuring the light pattern, even at the interface between live and dead samples.

References

[1] F. Merola, P. Memmolo, L. Miccio, V. Bianco, M. Paturzo, and P. Ferraro, Diagnostic Tools for Lab-on-Chip Applications Based on Coherent Imaging Microscopy, Proceedings of the IEEE, Vol.103, No.2, 2015.

[2] Miccio L, Memmolo P, Merola F, Netti PA, Ferraro P. Red blood cell as an adaptive optofluidic microlens. *Nat Commun* 2015; 6: 6502.

[3] F. Merola, P. Memmolo, L. Miccio, R. Savoia, M. Mugnano, A. Fontana, G. D'Ippolito, A. Sardo, A. Iolascon, A. Gambale, P. Ferraro, Tomographic Flow Cytometry by Digital Holography, *Light: Science & Applications* accepted article preview 17 October 2016; doi: 10.1038/lsa.2016.241.

[4] P. Memmolo, L. Miccio, M. Paturzo, G. Di Caprio, G. Coppola, P. A. Netti, and P. Ferraro, "Recent Advances in Holographic 3D Particle Tracking," *Adv. Opt. Photon.* 7, 713-755 (2015).

[5] P. Memmolo, M. Iannone, M. Ventre, P.A. Netti, A. Finizio, M. Paturzo, P. Ferraro. On the holographic 3D tracking of in vitro cells characterized by a highly-morphological change. *Opt. Express* 20, 28485-28493 (2012).

[6] P. Memmolo, C. Distante, M. Paturzo, A. Finizio, P. Ferraro, B. Javidi, Automatic focusing in digital holography and its application to stretched holograms. *Opt. Lett.* 36, 1945-1947 (2011).

[7] J. Sharpe, U. Ahlgren, P. Perry, B. Hill, A. Ross, J. Hecksher-Sørensen, R. Baldock, D. Davidson, Optical Projection Tomography as a Tool for 3D Microscopy and Gene Expression Studies. *Science* 296, 541 (2002).

[8] L. De Falco et al., Functional and clinical impact of novel TMPRSS6 variants in iron-refractory iron-deficiency anemia patients and genotype-phenotype studies. *Hum. Mutat.* 35, 1321-9 (2014).

[9] R. Sessa, S. Puzone, M. Ammirabile, C. Piscopo, L. Pagano, S. Colucci, P. Izzo, M. Grosso, Identification and molecular characterization of the --CAMPANIA deletion, a novel α^0-thalassemic defect, in two unrelated Italian families. *Am. J. Hematol.* 85, 399 (2010).

[10] R. Origa, P. Moi, R. Galanello, A. Cao, Alpha-Thalassemia. GeneReviews® (2013).

[11] B. Javidi, I. Moon, S. Yeom, and E. Carapezza, Opt. Express 13, 4492–4506 (2005).

[12] A. El Mallahi, C. Minetti, and F. Dubois, Appl. Opt. 52, 68–80 (2013).

[13] B. Rappaz, P. Marquet, E. Cuche, Y. Emery, C. Depeursinge, and P. J. Magistretti, Opt. Express 13, 9361–9373 (2005).

[14] B. Kemper, S. Kosmeier, P. Langehanenberg, G. von Bally, I. Bredebusch, W. Domschke, and J. Schnekenburger, J. Biomed. Opt. 12, 054009 (2014).

[15] M. Kemmler, M. Fratz, D. Giel, N. Saum, A. Brandenburg, and C. Hoffmann, J. Biomed. Opt. 12, 064002 (2014).

[16] G. Di Caprio, A. Galli, R. Puglisi, D. Balduzzi, G. Coppola, P. Netti, F. Merola, L. Miccio, P. Memmolo, and P. Ferraro, P Digital holography as a method for 3D imaging and estimating the biovolume of motile cells, Lab on a Chip 13, 4512–4516 DOI:10.1039/c3lc50515d (2013).

[17] G. Coppola, G. Di Caprio, M. Gioffré, R. Puglisi, D. Balduzzi, A. Galli, L. Miccio, M. Paturzo, S. Grilli, A. Finizio, and P. Ferraro, Digital self-referencing quantitative phase microscopy by wavefront folding in holographic image reconstruction, Opt. Lett. 35, 3390–3392 (2010).

[18] N. Pavillon, A. Benke, D. Boss, C. Moratal, J. Kühn, P. Jourdain, C. Depeursinge, P. J. Magistretti, and P. Marquet, J. Biophotonics 3, 432–436 (2010).

[19] N. Pavillon, J. Kühn, C. Moratal, P. Jourdain, C. Depeursinge, P. J. Magistretti, and P. Marquet, LoS One 7, e30912 (2012).

[20] A. Khmaladze, R. L. Matz, T. Epstein, J. Jasensky, M. M. Banaszak Holl, and Z. Chen, J. Struct. Biol. 178, 270–278 (2012).

[21] Z. El-Schich, A. Mölder, H. Tassidis, P. Härkönen, M. Falck Miniotis, and A. Gjörloff Wingren, J. Struct. Biol. 189, 207–212 (2015).

[22] M. F. Miniotis, A. Mukwaya, and A. Gjörloff Wingren, PLoS One 9, e106546 (2014).

[23] A. Calabuig, M. Mugnano, L. Miccio, S. Grilli, and Pietro Ferraro, J. Biophotonics 1–9 DOI 10.1002/jbio.201500340 (2016).

4 Cell mechanics by optical manipulation

The combination of holographic optical tweezers and digital holography gives the possibility to manipulate and study complex processes in living cells. Here, we will focus on cell mechanics studies, in particular the role of actin filaments in response of forces applied by optical tweezers. To confirm the formation of the cytoskeleton structures (actin filaments) after the stimulation, a fluorescence imaging system was added as a control.

4.1 Cell mechanics and cell surface interactions: state of art

Investigating the mechanical crosstalk between cells and their surrounding environment is fundamental to understand the influence of forces on cell functions and responses [1,2]. Indeed, the correlation between cells and forces (sensed and generated by cells) has been receiving increased interest in biological and biomedical research. In particular, the ability of cells to sense forces is strictly correlated to cytoskeleton dynamics [3–5].

Generally, force transmission is accomplished via focal adhesions (FAs) [6]. Cells anchor onto the extracellular substrate through trans-membrane proteins, i.e. integrins, which form bonds with various extracellular protein-receptors, e.g. the adhesive signal Arg-Gly-Asp. Depending on the magnitude and the distribution of the transmitted forces, cells trigger different cascade pathways of biochemical signals that regulate short and long-term cellular responses and behaviors [7].

It is noteworthy that a quantitative determination of the transmitted forces would significantly contribute in shedding light on this mechanism, known as mechanotransduction. Until now, the correlation between forces and cell mechanotransduction has been carried out through techniques like traction force microscopy or by using flexible polydimethylsiloxane pillars [8,9]. Such techniques have helped us to understand the nature of the forces exerted by cells on the extracellular surroundings and to quantitatively measure them. This kind of experimental campaign has been conducted on adherent cells, by averaging the generated forces on the substrate contact points (FAs) [10,11].

4.2 Integrated optical platform for cell mechanics studies

Here, the optical system (well described in detail in paragraph 2.2) was used to manipulate micrometer latex beads, to anchor them to suspended cells in a predefined configuration and to induce mechanical stimuli and thus cell deformation.

In particular, the case presented in this work as a proof of concept is the simplest configuration of a single cell suspended between two rigid beads. The corresponding static deformation induced by a single stretching stimulus, kept constant in time, was investigated using a holographic particle tracking approach [12]. The cell mechanical response is discussed in terms of the mechanical contributions from cortical and cytoskeletal actin structures.

DH imaging was used to measure the forces generated in a quantitative, label free and non-invasive way. Furthermore, using DH imaging, an increase of the refractive index in the inner volume of the cell was revealed, along the direction connecting the two anchoring points on the beads, as discussed and shown below. We believe that such a detected increase in the quantitative phase imaging is due to the assembly of the cytoskeletal actin structure. In fact, fluorescence imaging allowed us to confirm the presence and reorganization of such inner structures, as clearly revealed by the experimental results presented herein.

4.2.1 Nanomechanics of a fibroblasts

In an attempt to better elucidate the material-cytoskeleton crosstalk during the initial stage of cell adhesion, here we report how suspended cells anchored to point-like bonds are able to assemble their cytoskeletons when subjected to mechanical stress. The combination of holographic optical tweezers and digital holography gives the cell footholds for adhesion and mechanical stimulation, and at the same time, acts as a label-free, force-revealing system over time, detecting the cell nano-mechanical response in the pN range.

To confirm the formation of the cytoskeleton structures after the stimulation, a fluorescence imaging system was added as a control. The strategy here proposed portends broad applicability to investigate the correlation between the forces applied to cells and their cytoskeleton assembly process in this or other complex configurations with multiple anchor points.

In particular, a mixture of RGD functionalized beads and cells (NIH/3T3 murine fibroblast) was introduced in a temperature and CO_2 controlled chamber (Petridish) with optimized concentrations to perform the experiments. The Petri-dish was opportunely pre-treated to avoid cell adhesion. First, the beads were trapped using HOT (Fig. 1b) and then moved in contact with the cells (Fig. 1c) to promote attachment.

Digital holograms were numerically processed to simultaneously track the trapped microspheres and recover the quantitative phase-contrast map of the entire field of view in order to monitor the Optical Path Difference (OPD) induced on the cell by the mechanical stresses.

The analysis consisted of the following steps: (i) characterization of trapped bead motion in time, by a previously proposed method, [12] to detect statistical changes in bead movements before and after static deformation of the cell; (ii) QPM reconstructions for cell monitoring to detect shape changes; (iii) fluorescence imaging to correlate bead motion and cell shape modifications with cytoskeleton assembly. Holographic particles tracking method is applied to recorded digital holograms by calculating the displacement of moving object from two subsequent holographic reconstructions, as specified in ref. 12.

In particular, the minimum displacement that it is able to detect is defined as $p_x/2$, where p_x is the pixel size in the image plane. In the current implementation px = 54 nm, allowing an accuracy equal to 27 nm. The main steps of the experiment, which lasted about 1 h, are presented in Fig. 2 and 3. Specifically, Fig. 2a shows two optically trapped microbeads, for which we recorded the displacements in the first 5 min after trapping (3000 points, blue dots of Fig. 2e).

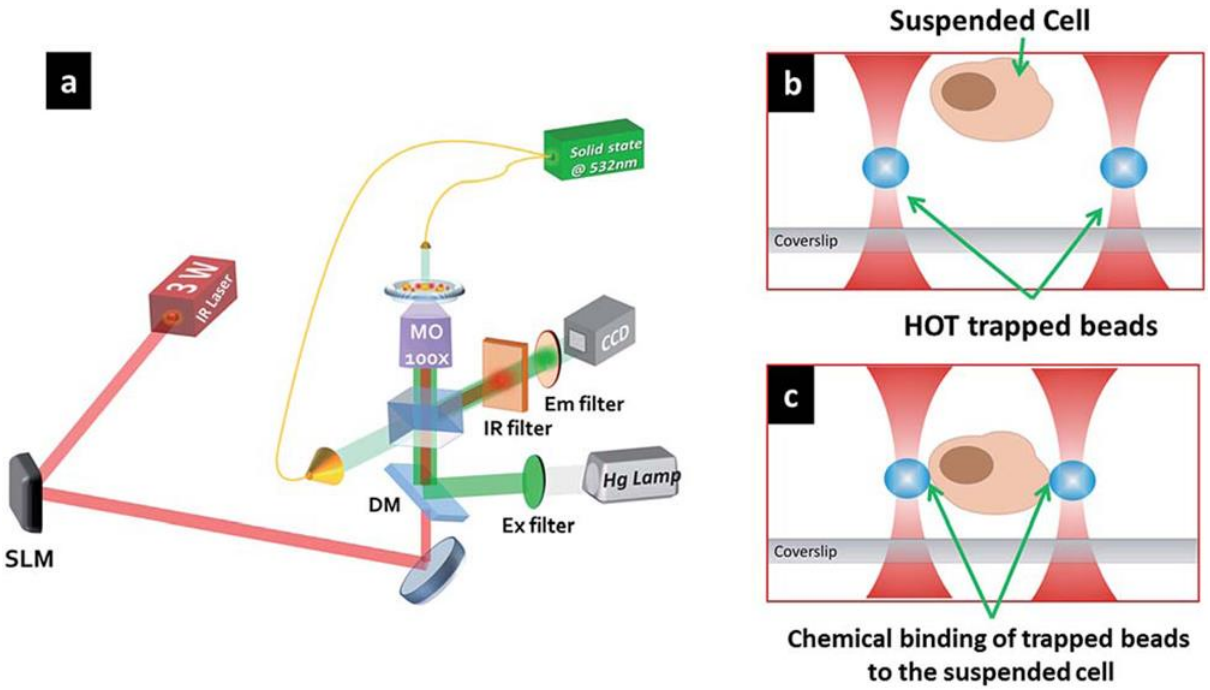

Figure 1: Experimental setup made of HOT, DH and fluorescence moduli. Design of the experiment: one or more beads are optically trapped (b) and attached to a single floating fibroblast (c) [ref. 17].

Similarly, the displacement trend immediately after the particle approach and during the attachment phase to the cell membrane is shown in Fig. 2b–f. The statistical behaviors of the displacement values reported in Fig. 2e and f are very similar, however, an average damping of 3% was calculated in the case of the attached beads. Nonetheless, we find that this perturbation is completely recovered in the first 5 min after bead attachment. At this time point (20th min), mechanical stretching was imposed on the right side bead shifting it 2 μm along the x-axis. Then, by monitoring the beads after stretching for 10 min (Fig. 2c–g), no damping of their displacements was observed with respect to the case reported in Fig. 2f. After this time interval, the tracking measurements revealed that the effect of static stress was a damping in the right bead displacements (Fig. 2d–h). Because no other stimuli occurred during the experiment, the cell reacted by stiffening itself into a static tensional state, as shown by the envelope in the bead displacements.

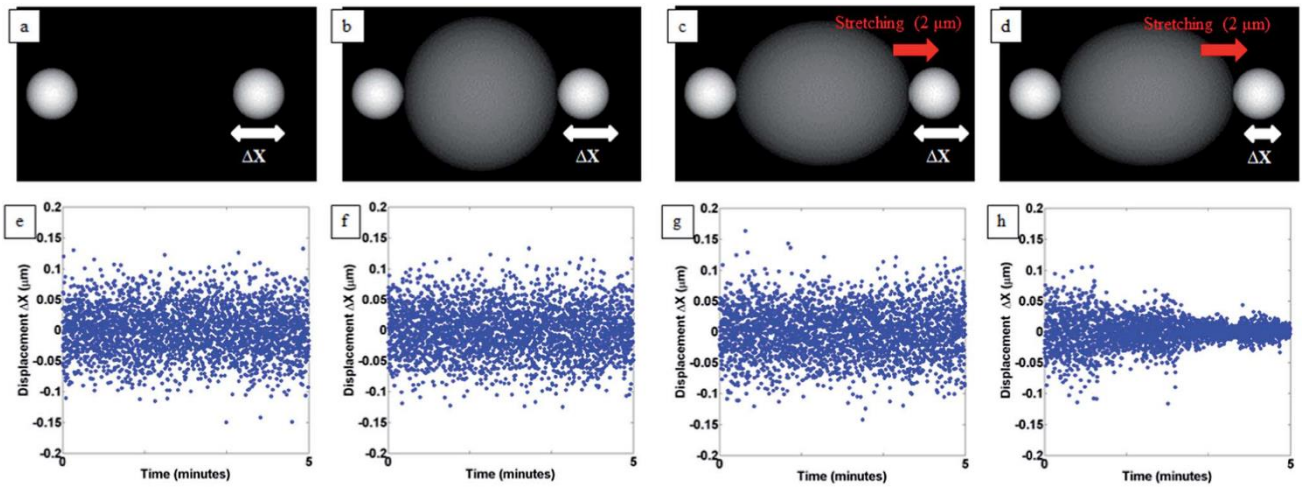

Figure 2: Time evolution windows (5 min) of the bead displacements (blue points) along the x-axis before and after stretching (held for the rest of the experiment) by shifting the right bead by 2 µm; (a) when the beads are trapped by HOT they present the classical Brownian motion of a particle in a potential well (e), the same happens immediately after attaching the beads to the cell (b–f).
Once stretched, the bead still presents the classical Brownian motion of a particle in a potential well (c g). Conversely, after 10 min from stretching (d–h) the amplitude of the displacements is considerably reduced [ref. 17].

This was confirmed by calculating the trap stiffness (k_{trap}) from the bead displacement over time (see Fig. 3a and b). Since we calculated an accuracy of 27 nm in the displacement measurements, the corresponding stiffness precision is 0.16 pN µm^{-1}.

We found that, before the beads adhere to the cell, the trap stiffnesses were 2.7 pN µm^{-1} and 2.1 pN µm^{-1} along the x and y-axes, respectively, i.e. trapped bead displacements in this first stage presented typical Brownian behavior. We observed that the stiffness along the x-axis did not change after the attachment to the cell membrane. If we assume that in the bead–cell–bead system, the composed elastic constant of the trapped beads was $k = k_{trap} + k_{mem}$, where k_{mem} is the membrane stiffness, then soon after attachment the total stiffness returned to a comparable value to that before the cell bead engagements ($k = k_{trap} + k_{mem} \approx k_{trap}$).

However, a variation in the trap stiffness was calculated along the y-axis, allowing for a 6% increase in the total stiffness.

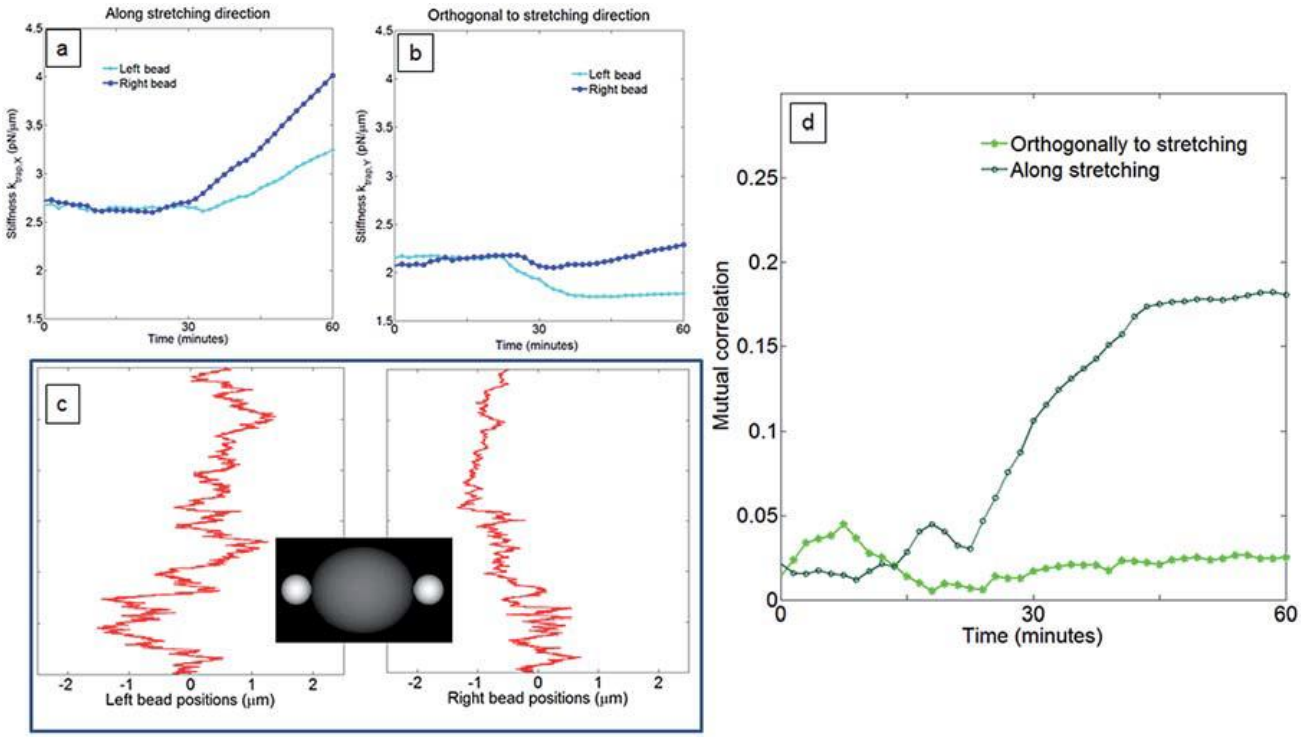

Figure 3: Trap elastic constant measured as a function of time for both beads along the x-axis (a) and y-axis (b), where x is the stretching direction. (c) Drift displacements of the left and right beads, respectively, demonstrate a cell contraction after mechanical stimulation. In (d) the mutual correlations between the left and right displacements along both the x and y-axis are reported [ref. 17].

In addition, we evaluated the exerted force on the cell, which was found to be about 5 pN. Surprisingly, considering the amount of deformation on RBCs previously reported, [13,14,15] the application of forces with the same order of magnitude (tens of pN) on a suspended fibroblast did not produce any detectable deformation, as previously observed [16]. This led to the consideration that different mechanical properties and different values of membrane tension were involved. However, at around the 30th minute (see Fig. 3a), the trap stiffness started to increase reaching values of about 40% and 25% higher than at the beginning, for the right and left beads, respectively. It is noteworthy that the trap elastic constants reported in Fig. 3a were the result of the numerical envelope of the data collected during the experiment. Additionally, a stiffness variation was observed along the y-axis, equal to 9% and 13%, for the right and left beads, respectively, as shown in Fig. 3b. As a consequence, such results produced a correlated displacement between the beads,

evaluated during the experiment and reported in Fig. 3d. Interestingly, the mutual correlation factors followed the same trend as the trap stiffness over time. In fact, in the time interval before and after bead attachment, their motions were completely uncorrelated, with a correlation factor ranging between 0 and 0.05. After mechanical stimulation, the correlation factor increased to ~0.2, thus indicating that the bead oscillation around the trap equilibrium position had begun to decrease. No correlation was observed orthogonal to the stretching. The previous evaluation was devoted to understanding the temporal evolution of cell behaviour through its stiffness and the correlation between the trapped beads. However, in order to calculate the instantaneous forces exerted by the fibroblasts we considered independently the different intervals of time reported in Fig. 2 and the corresponding displacement measurements. This analysis furnished a different stiffness value with respect to that of Fig. 3a and b, because no temporal correlation was considered.

In particular, we calculated an increment of the absolute elastic constant from 2.6 to 29.4 pN μm^{-1} for the right bead along the stretching direction (see Table S1 of ref 17). Another interesting effect is reported in Fig. 3c, where the drift displacement values of the beads are reported. Both microspheres show a displacement of ~0.5 μm (left bead) and ~1 μm (right bead) towards the cell nucleus, indicating a cell contraction after mechanical stimulation. Furthermore, combining such displacement values with the elastic constants of both traps along the stretching axis (8.1 and 29.4 pN μm^{-1} from Table S1 of ref 17) we evaluated the forces generated by the cell as ~4 pN and ~30 pN, respectively. Asymmetric values could arise from different adhesions of cells on the microspheres. When adherent cells detach from their own substrates, they curl up and their cytoskeleton is less structured. In particular, the actin cortex of the cell remains, whereas the contracting actin stress fibers are only present in the adherent state. Through our setup we recreated cell adhesions, in a point-like manner, giving the cell the chance to reassemble actin structures. The resulting values of the measured forces exceeded those needed to stall approximately eight actin parallel polymerizing filaments (1 pN) [18]. It has been proved that the average pulling force generated by a single myosin molecule interacting with a single actin filament is 3–4 pN [19]. Then, considering the direction of the bead displacements and the force range

measured, we were able to exclude the fact that actin pushes against the trapped microspheres. Taken all together, these results suggested that the damping motion we collected for the beads attached to a fibroblast might be the direct consequence of cell stiffening. In an attempt to understand if such a phenomenon is associated with the assembly of cellular actin structures, we performed the same experiment with fibroblasts after transfection treatment (see Appendix A.2.5).

First, cell adhesion on a point-like foothold (trapped microbeads) was conformed using the fluorescence modulus (Fig. 4). Then, we investigated the cytoskeleton assembly at three instants of time, i.e. suspended cell without beads (t = 0), 20 min after cell-bead attachment (t = 20 min), and 30 min after stretching (t = 50 min), using both DH and fluorescence moduli. As expected, we found that at t = 0 and t = 20 min no actin organization was detected, as confirmed by the DH-QPMs and fluorescence images reported in Fig. 5 a, b, d and e. Contrarily, in the time interval in which we recorded the displacement damping, i.e. after stretching (t = 50 min), structured actin filaments were clearly visible (Fig. 5c and f).

In Fig. 5c the QPM of the cell in false colour at t = 50 min reveals an enhancement of the OPD along the axis connecting the two microspheres, not present in the previous situations, indicating a modification of the internal cellular structure. In order to investigate such an arrangement, we recorded a fluorescence image at the same instant of time (Fig. 5f). Surprisingly, we found evidence of a signal corresponding to the actin filaments, suggesting a cytoskeleton assembly inside the cell volume. In fact, the cytoskeleton modified its assembly over time and polarized the fluorescent filaments in the direction connecting the two external beads, as proved by the QPMs (Fig. 5c–f). At this early stage, taking into account only the QPMs, it was not possible to confirm the presence of the cytoskeleton for two reasons: the low resolution and the lack of specificity in the OPD signal retrieved. However, it is difficult to imagine different causes that can produce such phase variation inside the cell in the particular setup we fabricated. Consequently, we believe that the enhancement found in the OPD, together with the cell stiffening and fluorescence observations were ascribable to attempts of early cytoskeleton assembly by the cell.

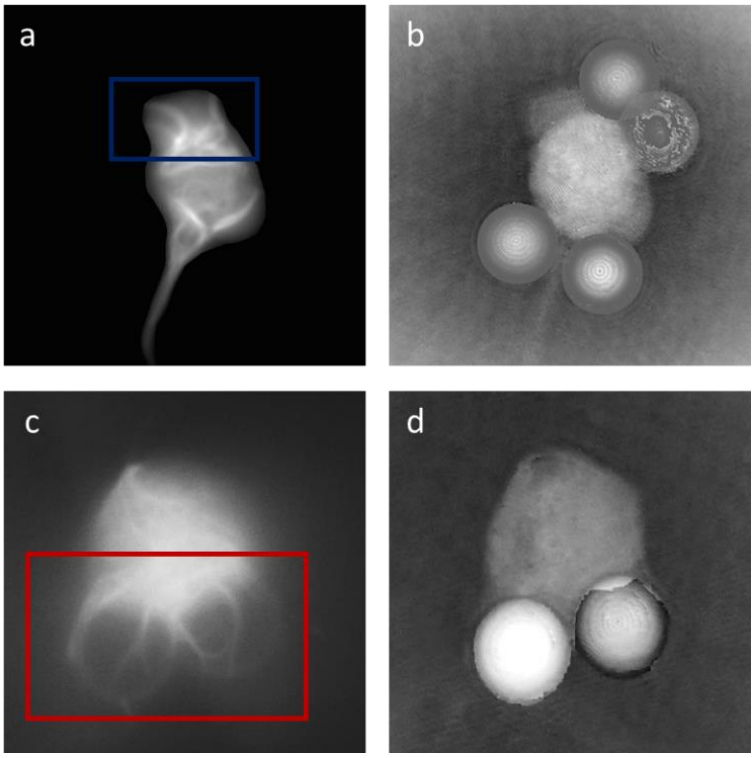

Figure 4: (a,c) Fluorescence images and (b,d) QPM of different trap configurations. (a,b) four beads and (c,d) two beads are attached to the fibroblast, in suspension. The cell feels as only foothold the beads, reorganizing itself consequently. Frame in images a and c configurations shows actin accumulation and filaments on microsphere surfaces indicating cell anchor points (focal adhesions) [ref. 17].

In summary, we developed a promising proof of concept/setup that gives cells, generally living in adhesion on 2D substrates, the possibility to adhere and mount their cytoskeleton in a 3D suspended configuration.

In particular, our approach is able to detect the cytoskeleton and force generation in response to mechanical stimuli by nanomechanical characterization.

The combined fluorescence imaging confirms cell stiffening by direct observation of the actin filament-bundles, thus demonstrating the capability of our framework to investigate the material–cytoskeleton crosstalk in the early (a few hours) adhesion time and for different shape configurations. Moreover, the preliminary QPM results are promising and permit us to consider DH as a label-free technique for cell nanomechanic investigations in the future.

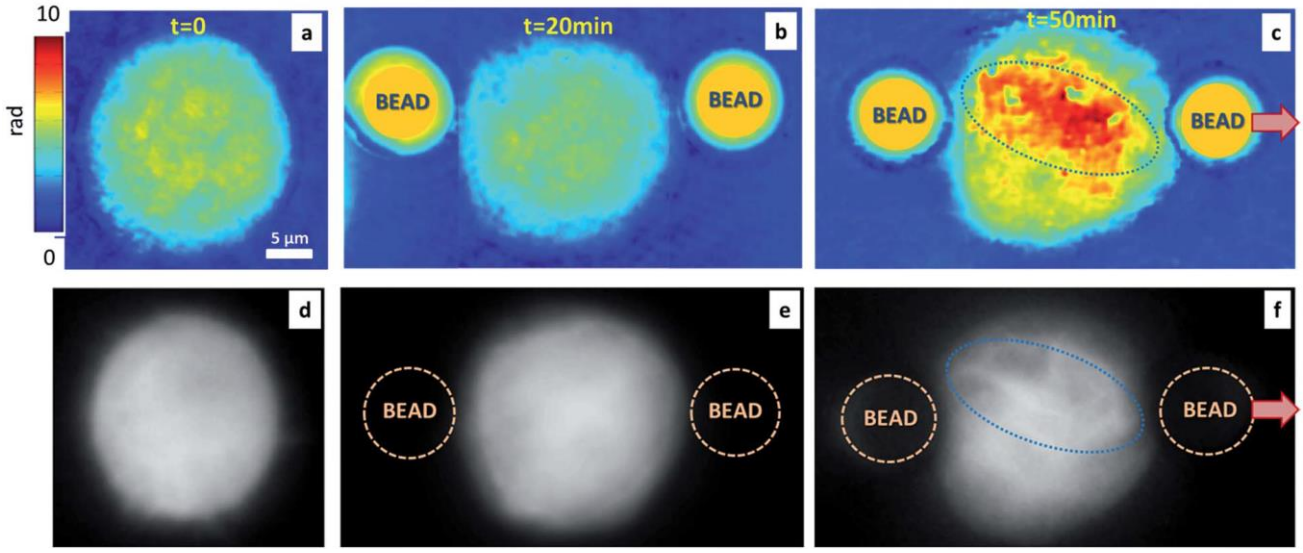

Figure 5: (a and d) are QPM and fluorescence images of a LifeAct-RFP transfected cell in suspension before microbead approach (t = 0) and (b and e) clamped between two microbeads (t = 20 min). (c and f) QPM and fluorescence image at t = 50 min of the experiment (30 min after stretching), showing the presence of actin aggregates. (c) QPM of the cell shows an enhancement of the OPD signal corresponding to the area connecting the two microspheres (the dotted line is just a guide for the eye), confirmed by the fluorescence image (f) of the assembling cytoskeleton [ref. 17].

References

[1] S. Olof, J. Grieve, D. Phillips, H. Rosenkranz, M. Yallop, M. Miles, A. Patil, S. Mann and D. Carberry, Nano Lett., 2012, 12, 6018–6023.

[2] S. Fusco, V. Panzetta, V. Embrione and P. A. Netti, Acta Biomater., 2015, 23, 63–71.

[3] D. A. Fletcher and R. D. Mullins, Nature, 2010, 463, 485–492.

[4] A. R. Bausch and U. S. Schwarz, Nat. Mater., 2013, 12, 948–949.

[5] E. Battista, F. Causa, V. Lettera, V. Panzetta, D. Guarnieri, S. Fusco, F. Gentile and P. A. Netti, Biomaterials, 2015, 45, 72–80.

[6] B. Geiger, J. P. Spatz and A. D. Bershadsky, Nat. Rev. Mol. Cell Biol., 2009, 10, 21–33.

[7] A. W. Orr, B. P. Helmke, B. R. Blackman and M. A. Schwartz, Dev. Cell, 2006, 10, 11–20.

[8] W. R. Legant, C. K. Choi, J. S. Miller, L. Shao, L. Gao, E. Betzig and C. S. Chen, Proc. Natl. Acad. Sci. U. S. A., 2013, 110, 881–886.

[9] I. Schoen, W. Hu, E. Klotzsch and V. Vogel, Nano Lett., 2010, 10, 1823–1830.

[10] S. Schlie, M. Gruene, H. Dittmar and B. N. Chichkov, Tissue Eng., Part C, 2012, 18, 688–696.

[11] D. Stamenovi´c and D. E. Ingber, Biomech. Model. Mechanobiol., 2002, 1, 95–108.

[12] L. Miccio, P. Memmolo, F. Merola, S. Fusco, V. Embrione, A. Paciello, M. Ventre, P. Netti and P. Ferraro, Lab Chip, 2014, 14, 1129–1134.

[13] H. Zhang and K.-K. Liu, J. R. Soc., Interface, 2008, 5, 671–690.

[14] S. Raj, M. Marro, M. Wojdyla and D. Petrov, Biomed. Opt. Express, 2012, 3, 753–763

[15] G. Tomaiuolo, Biomicrofluidics, 2014, 8, 051501.

[16] F. Schlosser, F. Rehfeldt and C. F. Schmidt, Philos. Trans. R. Soc., B, 2015, 370, 20140028

[17] S. Fusco, P. Memmolo, L. Miccio, F. Merola, M. Mugnano, A. Paciello, P. Ferraro and P. A. Netti, RSC Adv., 2016, 6, 24245.

[18] M. J. Footer, J. W. Kerssemakers, J. A. Theriot and M. Dogterom, Proc. Natl. Acad. Sci. U. S. A., 2007, 104, 2181–2186.

[19] D. Mehta and S. J. Gunst, J. Physiol., 1999, 519, 829–840.

5 Dynamic platform for cell handling and polarization by optically-induced electric fields

Here, we present a novel platform for cell handling, in particular for inducing ordered alignment and elongation in cells by exploiting optically-induced electric fields.

The response of bacteria and fibroblasts on ferroelectric lithium niobate is studied in terms of the orientation and morphological differences induced by the field gradients generated by photorefractive effect on its surface.

Controlling cell alignment is one of the most fascinating challenge in biotechnology field and tissue engineering. For example in native myocardial tissue, the complex organization of cardiomyocytes and fibroblasts within the cardiac extracellular matrix is critical to the electrical and mechanical properties of the heart [1]. Musculoskeletal tissue is similarly organized, with myoblasts forming highly aligned muscle fibers through fusion into multi-nucleated myotubes [2]. This specific arrangement of differentiated myocytes within the musculoskeletal ECM is essential for the generation of contractile force. In a broad range of additional tissue of the human body, from the vasculature to connective tissue, tissue function is also dictated by cellular organization [3].

However, in previous studies, the inability to control cell behaviour has often resulted in poor cell and ECM organization within engineered constructs. Such tissue constructs had limited ability to recreate complex tissues characterized by precise cell and ECM alignment. Microscale technologies have been successfully integrated into many tissue engineering applications and have allowed for enhanced control of cell behaviour and function through control of the cellular microenvironment [4-8].

On the other hand, the capacity of cells to sense and respond to physiological electric fields (established by a trans-epithelial potential difference in tissues) is a very important issue, because several processes such as wound healing, development, cell migration and nerve regeneration are under the effect of endogenously generated electric fields. In culture, many epithelial and endothelial cells respond to an external electric field of magnitude similar to the endogenous, by moving preferentially either parallel or antiparallel to the field vector, a process

known as galvanotaxis [9-11]. Moreover, electric fields influence cell division, polarity, shape and morphology. Cell movements and migration under the effects of electric fields relies on the ability of the cells to interact with a given substrate thanks to the process known as cell adhesion, a fundamental process for the maintenance of cell architecture [12]. It guarantees the right tissue structure, necessary for the correct functioning of tissue. Cell adhesion (the physical interaction of a cell with another cell or with the extracellular matrix) is essential also for cell migration. Cell-cell adhesion maintains epithelial tissues, supports functional contacts between specialized cells, and can facilitate directed migration. Furthermore, it has been well described the importance of the substrates, independently of substrate chemistry, for cell adhesion and cell migration [13-16]. In the last years several methods have been developed for controlled cell alignment and patterning devoted at ordered tissue growth or for studying cells in isolated state or, ultimately, for guiding cell migration, differentiation and fate. Mainly they can be classified depending on the type of interaction involved, i.e chemical, mechanical, electrical or a combination of them. Smart polymeric structure have been realized to force cell in ordered geometries both in 2D and 3D [17-18] and cell morphological changes have been quantified also in reversible topographic pattern geometries [19].

5.1 Dielectrophoretic approach based on lithium niobate

A well-established technique for cell handling in microfluidics is dielectrophoresis [20,21] a non-invasive technique used for many different purposes, such as drug discovery and delivery [22], detection and separation of cancer cells [23], medical diagnostics and quantitative cell analysis. DEP is the motion of a polarizable particle in a non-uniform electric field usually generated by printed electrodes properly designed for the experiment.

DEP in combination with suitable cellular adhesive has been employed for alignment of single mammalian cells [24]. A further class of methods for cell manipulation is based on the light interaction usually employed to activate a photo-responsive material that selectively interact with the biological sample [25-28].

Recently the development of new DEP based techniques allowed the establishment of electrode-free approaches, useful for their high degree of versatility and for the possibility to avoid the use of external electric field sources. These methods have been demonstrated to be able to manipulate micro-particles as well as to drive liquid and polymer [29-33]. They exploit the evanescent electric fields generated on ferroelectric crystals by means of light interactions.

Here we report the response of bacteria and mouse fibroblasts NIH-3T3, on the surface of ferroelectric iron doped lithium niobate (Fe:LN) where virtual-electrode are generated by photorefractive (PR) effect, starting from the first interaction with the material, until the full spreading, in order to understand the dynamics of adhesion and cell migration and their effects on the morphology of actin cytoskeleton.

A combination of two innovative approaches, electrode-free dielectrophoresis and a digital holographic microscopy was used to monitor these phenomena. The light induced DEP is achieved through ferroelectric iron-doped lithium niobate crystals used as substrates. Due to the photorefractive property of such material, charge distribution inside its volume is generated by using light and the resulting electric fields are able to induce a preferential orientation of the cells.

This new technology may thus be used to investigate most of the electric field driven events such as cell migration, cell division, wound healing and all the processes linked to cell-substrate interaction. The novelty of this device is the possibility not only to generate electric fields with light in absence of electrodes but also to reversibly control cell behavior in time and space. The biocompatibility of LN has been proved in literature where the interactions of in vitro cells on poled and unpoled crystals has been characterized [33-35].

Here LN is exploited to generate evanescent fields whose strength is able to modify the cellular morphology. We demonstrate that PR fields have a double function. At the first stage where cells are seeding on the surface the fields are responsible of a positive DEP trapping in correspondence of the regions where the higher gradients are present. After trapping the fibroblasts start the adhesion process with subsequent spreading. We reveal that after 24 hours the 80% of cells present an elongated shape whose major axis is oriented perpendicularly to the linear virtual-electrodes. Here, we report also that is possible to apply such electrode-free DEP

cues to pattern biological objects such as eukaryotic cells (NIH-3T3 mouse fibroblasts) and bacteria. Cells oriented perpendicularly to the charged pattern generated by light, also assuming a peculiar shape. Once the charge pattern is erased, again by light, the cells re-orient and change their morphology. This phenomenon highlight the possibility to control cell shape, movement, orientation and behavior by means of light.

5.1.1 General properties of Lithium niobate crystal

The response of a material to the application of an external electric field is strictly regulated by its electrical properties. In the presence of available free carriers (unbounded charges, either electrons or ions) the material will exhibit an electric current proportional to the applied voltage, hence performing as a *conductor*.

Metals and electrolytes are examples of conductive materials. If the activation of charge transport necessitates a minimum energy to be provided to the system, the material is classified as a *semiconductor*. Silicon, germanium and alloys of the III-V groups of the periodic table belong of the semiconductor material family, and well known platforms for electronics. Finally, if no free carriers are available for conduction, the material is defined as a *dielectric*, or simply an *insulator*. Dielectrics represent a broad family of materials, which can be polarized by external electric fields. In general, such a property arises from their atomic structure, which upon the application of external electric fields shows spatially-separated complexes of charges of opposite sign, called dipoles.

However, some dielectrics are made of polar molecules; hence already possess intrinsic electric dipoles.

Dielectrics which possess dipoles are called pyroelectrics and show a polarization, called spontaneous polarization Ps**,** even in absence of external electric field. In particular, as shown in Figure 1, ferroelectrics represent a subgroup of pyroelectric materials in which such polarization can be reoriented by the application of external electric fields [36]. As a consequence of their intrinsic nature, we can

define, for these ferroelectric crystals, the electric displacement vector D as a superimposition of different contributes:

$$D = \varepsilon_0 E + Pi + Ps$$

where ε_0 is the dielectric permittivity of vacuum, E the electric field, Pi the induced polarization and Ps the spontaneous polarization. Among the others, the lithium niobate has gained a prominent role in research and applications of ferroelectric crystals and is one of the most used electro-optic (EO) materials. $LiNbO_3$ is characterized by large pyroelectric, piezoelectric (PZ), nonlinear and EO coefficients and has useful acoustic and acousto-optic properties. This richness of large-magnitude physical effects has caused LN to become widely used in applications such as acoustic wave transducers, optical amplitude modulators, second-harmonic generators, beam deflectors, dielectric waveguides, memory elements, holographic data processing devices, and others [37]. LN is a human-made dielectric material (Czochralski growth technique [38]) that doesn't exist in nature and it was first discovered to be ferroelectric in 1949 [39]. It is a rhombohedral crystal that consists of planar sheets of oxygen atoms in a distorted hexagonal close-packed configuration [40].

Octahedral interstices are formed, one third of which is occupied by niobium (Nb) atoms, one third by lithium (Li) atoms, while the rest is vacant. Above the Curie temperature Tc (around 1210°C) the phase is para-electric (no spontaneous polarization), while in the ferroelectric phase, below Tc, LN exhibits spontaneous polarization Ps along the c axis, resulting in a c+ and a c- face.

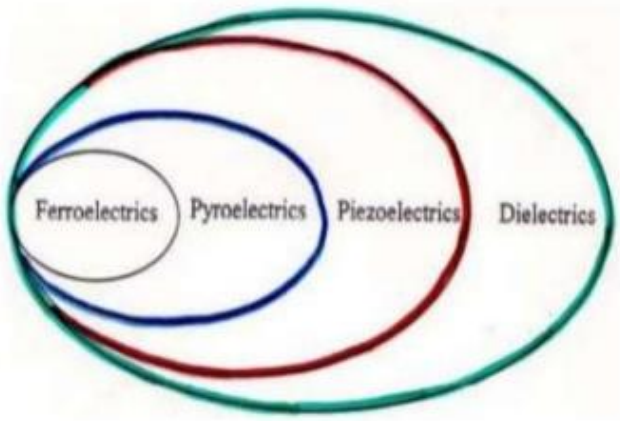

Figure 1: Classification of ferroelectrics.

The c+ face corresponds to the positive end of the dipole and, vice versa, the c- face corresponds to the negative end of the dipole. In the para-electric phase the Li atoms lie in an oxygen layer that away from the Nb atom while the Nb atoms are centered between oxygen layers. Conversely, in the ferroelectric phase the elastic forces of the crystal become dominant and force the lithium and niobium ions into new positions.

The spontaneous polarization Ps changes according to $\Delta Pi=\xi i \cdot \Delta T$, where ξi is the pyroelectric coefficient and ΔT is the temperature variation. At equilibrium ($\Delta T = 0$) all Pi_s in the crystal are fully screened by the external screening charges and no electric field exists. The polarization change perturbs such equilibrium causing a lack or excess of surface charge, thus generating a high electric field, the pyroelectric field.

5.1.2 Photorefractive effect

This effect consists in a non-instantaneous and non-local refractive index change induced by light in the crystal [41-42]. In fact, this is due to a combination of some other effects.

First, one has to account with the presence of certain impurities or color centers which could be optically ionisable. In lithium niobate the most active photorefractive impurities are Fe, Cu and Mn. When they are present in the crystal, appear simultaneously in two valence states: Fe^{2+}/Fe^{3+}, Cu^{+}/Cu^{2+}, and Mn^{2+}/Mn^{3+} [43]. The reduced valence ions act as charge donors whereas the oxidized valence ions act as acceptors.

Second, inhomogeneous light of the proper wavelength produce ionisation of some donors.

Third, the released charges move along the crystals by means of one of the charge transport processes: diffusion in the band, photovoltaic current, or drift in an external electric field.

Forth, charge is trapped in acceptors. As the trapping occurs in a different place than ionization (darker places in average), a distribution of internal electric field is created.

Fifth, finally this electric field distribution induces a refractive index change distribution via the electrooptic effect.

The charge distribution remains in the crystal for some time when it is not illuminated. In this case, only the crystal dark conductivity contributes to redistribute the charge. By contrast, upon uniform illumination the charge is redistributed homogeneously after some time depending on light intensity and spectrum, due to photoconductivity. Consequently the refractive index change is erased.

Photorefractive effect is very dangerous for most optical applications because the light itself modifies with time the refractive index of the material just in its own way path. The result is a perturbation of propagation, as for example a fanning effect. Then, usually it is known as optical damage of the material. It can be avoided by propagation at high temperature or by doping with damage resistant impurities.

Considered this effect positively, one can make good use of it. This can be used to write with light and store for some time information in the material. This is what is done to produce optical memories.

Alternatively one can produce a useful optical element, as a phase grating, by changing the distribution of refractive indices. For lithium niobate, a thermal fixing process is known [43] to make these changes quasi-permanent at room temperature. Then, the optical element produced by this effect can be included in a practical setup. The uncontrolled residual photorefractive impurities and point defects provide of enough number of donors and acceptors to produce the unwanted damage effect.

In contrast, crystals are intentionally doped with photorefractive impurities when one seeks photorefractive applications. Most common is iron doping, and the usual concentration varies depending on the application from 0.01 mol% up to about 0.2 mol%.

5.2 Optical setup for "light writing process"

We tested on the *E. coli* bacteria and fibroblsts the effects of PR fields induced on the surface of *x*-cut Fe:$LiNbO_3$ (Altechna, dopant level 0.05%, 500 μm thickness (*x* axis), 20 x 20 mm in *y*–*z* plane). The PR field was generated by the optical arrangement well-described in Refs. [44,47]. A light source (Argon laser beam at 514 nm) with structured intensity was transmitted through the crystal to generate internal phase grating and surface electric field gradients that were exploited to immobilize and orient the bacteria and fibroblasts. Phase gratings with different periodicity were inscribed inside the crystal volume. Specifically, we tested 12.5 μm, 25 μm, 50 μm and 100 μm grating periods for bacteria cells, and 25 μm and 50 μm grating for fibroblasts.

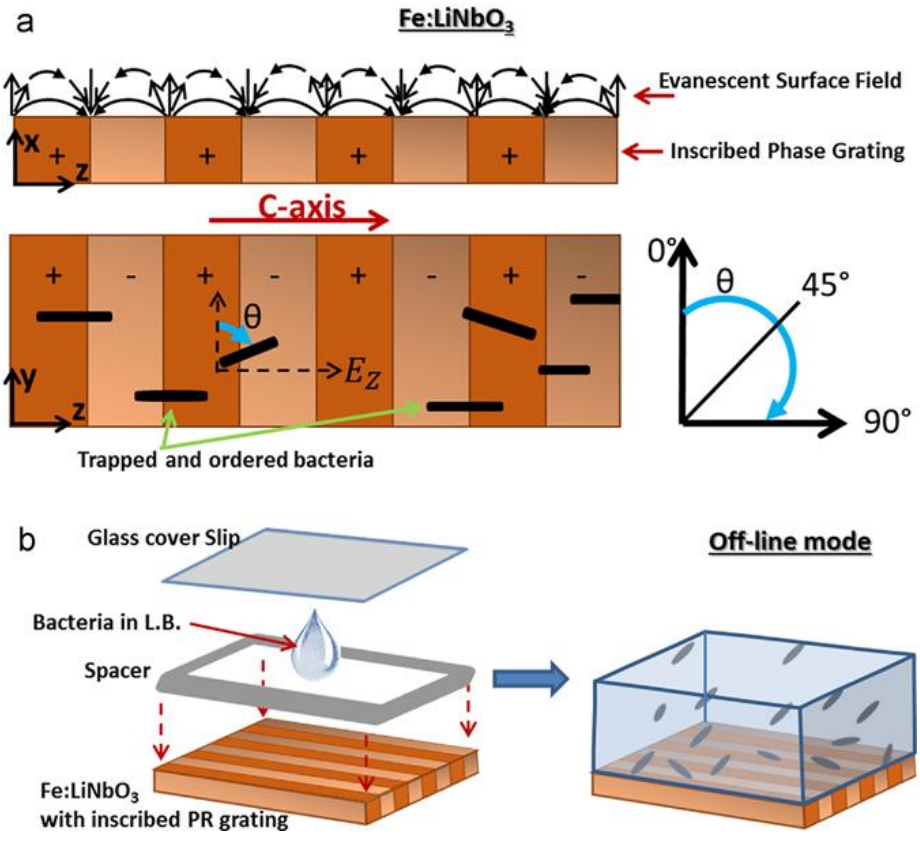

Figure 2: (a) Schematic representation of evanescent field and consequent E. coli orientation. The angle, θ, between each bacterium and the direction of grating planes, is measured. (b) Drawing of the sample: a closed chamber containing about 30 μl of bacteria suspended in LB, the bottom surface of the chamber is Fe:$LiNbO_3$ [ref. 32].

The polarization of the laser beam and the grating vector $\vec{k}$ are parallel to the *z*-axis (*c*-axis) of the crystal for all the experiments. A schematic drawing of the charge distribution and correspondent evanescent field is reported in Fig. 2(a).
In case of bacteria cells, the experiments were carried out in two modalities:

(i) *in line*: A small volume of bacteria suspended in Luria-Bertani (LB) broth medium (10 g/l NaCl, 10 g/l tryptone, 5 g/l yeast extract) (30 μl—about 6 x 10^5 cells) was placed on crystal surface. Then such system was exposed to the laser light to generate the surface DEP forces. In this case the bacteria are on the crystal during the grating formation.

(ii) *off line*: Only the crystal was exposed to laser light. The *E. coli* drop was laid on it after the grating formation.

Adhesive spacer and coverslip were used to realize a close chamber to avoid liquid evaporation in both modalities, Fig. 2 (b) reports a sketch for the *off line* case.
For both the experimental procedures, image recording and processing were performed to analyze the bacteria arrangement related to the inscribed phase gratings. For each grating period, a complete image mapping of the samples was performed under a bright field microscope (Axio Imager. M1m, Zeiss-Germany) using 20 x and 40 x objectives.
All of the images were recorded under phase-contrast mode in order to best visualize both the PR phase grating and the bacteria cells. The recording of all images was performed, at maximum, 15 min after light exposure and 20 min after the measurement of *E. coli* concentration. Subsequently, measurements of the orientation angles were accomplished by ImageJ, a freely available software for image handling (http://imagej.nih.gov/ij/).
We measured the angle, θ, between each single bacterium and the direction of the grating planes (see Fig. 2(a)). The histograms shown in the following section were realized by Excel and Matlab. In particular, the Cartesian histograms display the percentage of bacteria whose angle is in the range 45–90° respect to the grating planes while the polar histograms represent the number of bacteria in 70 angular intervals between 0° and 90°.

5.3 Control of cell behavior in time and space by photorefractive effect

The average length of E. coli bacteria is 1–2 μm but during our experiments we observed a higher alignment in case of bacteria chains. This observation leads us to hypothesize that it is possible to operate a control during the bacteria duplication in terms of ordered growth. We performed a preliminary experiment to prove this possibility so that, after the light exposition, the sample is incubated at 37 °C for 2 h. Some pictures are recorded and reported in Fig. 3 confirming our hypothesis where a significant ordered arrangement of bacteria is present in the sample. In particular, we calculate the alignment percentage of the bacteria chains longer than 10 μm. The percentage increased from 68.5% to 77.8% in case of 25 μm grating in *off-line* mode.

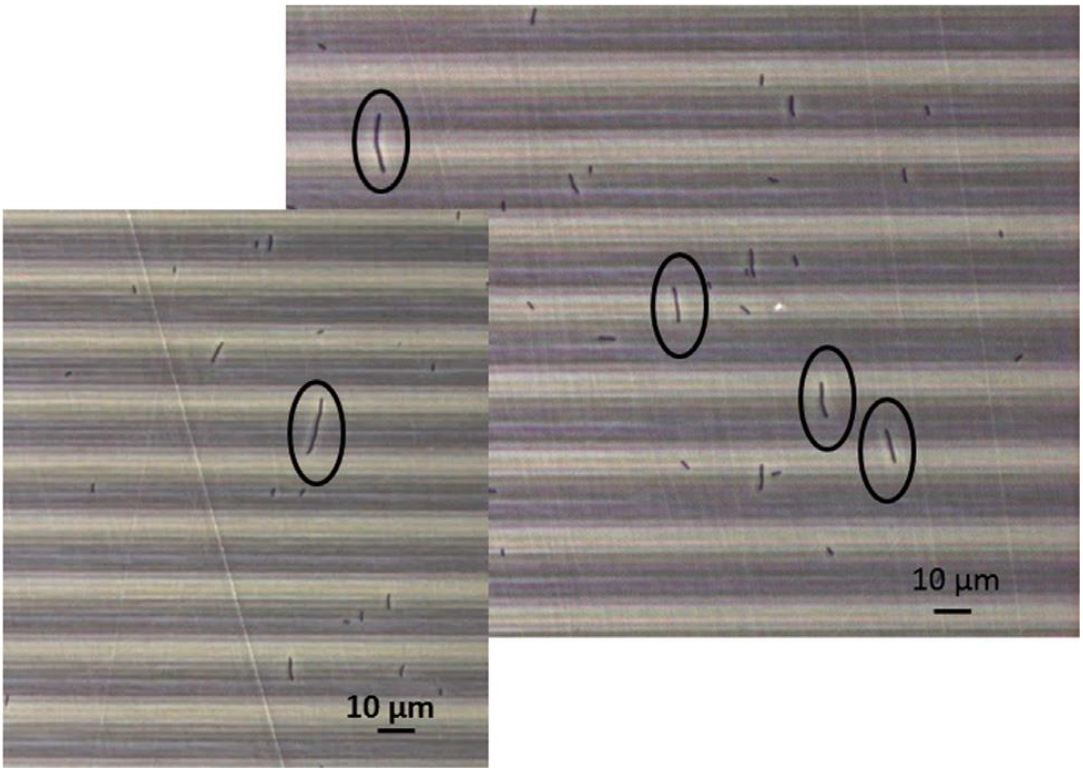

Figure 3: Two pictures of bacteria chains longer than 10 μm aligned perpendicularly to the grating planes. Image are recorded in *off-line* mode for 25 μm grating [ref. 32].

5.4 Cell pattering: bacteria and fibroblasts

For all the tests performed a significant high percentage of bacteria were arranged in a perpendicular way respect to the grating planes i.e. they were elongated in the direction parallel to the grating vector $\vec{k}$. We repeated the experiments 20 times for each one of grating period and for both modalities described before. In Fig. 4 some pictures are displayed proving these results that, for the first time, demonstrate the possibility to manage live biological sample by exploiting PR fields. Such images refer to different samples, different grating periods and also diverse *E. coli* concentration.

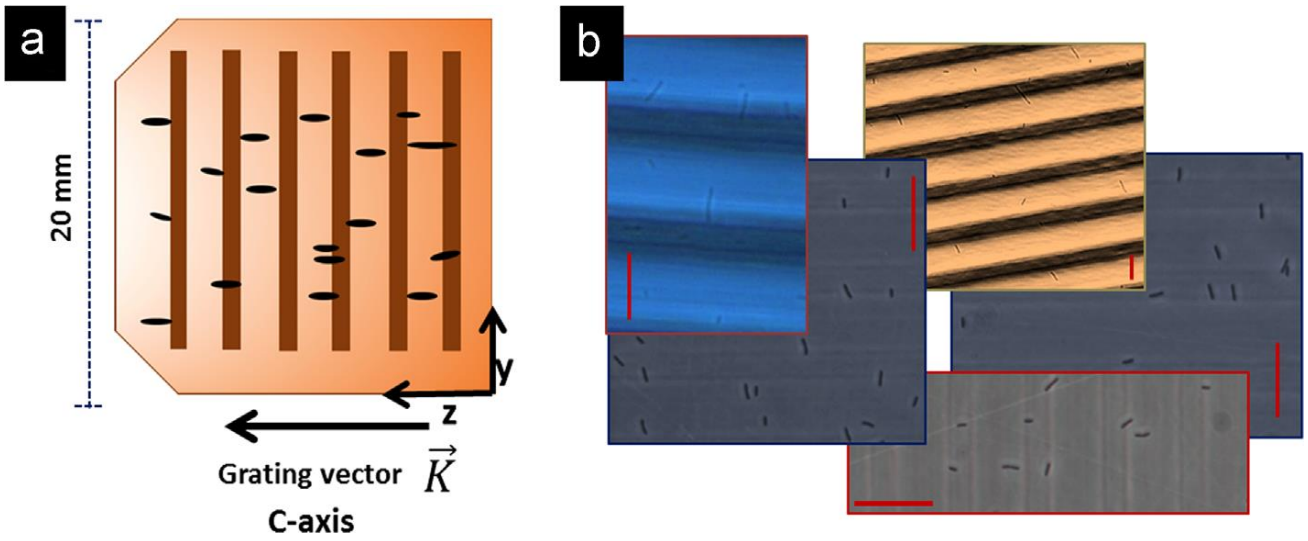

Figure 4: (a) Drawing of bacteria arrangement on the whole crystal surface. (b) Pictures of aligned bacteria on different grating periods and with different magnification. All scale bars are 20 μm [ref. 32].

The photovoltaic evanescent field and the corresponding DEP potentials on the surface of Fe:$LiNbO_3$ are well-known and characterized in literature [48–50]. We performed the experiments with periodic laser light intensity, $I = I_0(1+m \cos kz)$ where m is the modulation ratio and K the wavevector of intensity profile. For $m \sim 1$ the evanescent field has harmonic terms with grating vector $K_n = nK$ (n=1,2,3…) and a good approximation is to keep only terms correspondent to grating vectors K and $2K$ (i.e. the fundamental and the second harmonic terms): E_z

$(x;z) = -E_K e^{-Kx} \cos Kz - E_{2K} e^{-2Kx} \cos 2Kz$, $E_x = (x;z) = E_K e^{-Kx} \sin Kz + E_{2K} e^{-2Kx} \sin 2Kz$, where E_K depends on the bulk field amplitude and E_{2K} is the amplitude of the second harmonic term [51].

Bacteria are first trapped by the DEP potential and, because of their cylindrical shape, the evanescent field induces a dipole moment $\vec{p}$ on each bacterium that is responsible for a torque $\tau = \vec{p} \times \vec{E}$ able to orient them in the direction of the *z*-component of the photovoltaic field (Fig. 2(a) and Fig. 4). By means of standard interferometric technique, we measure the value of the refractive index difference associated to the field and consequently we calculate the photovoltaic field induced by the electro-optic effect to be ~ 6 kV/mm [49,51].

Concerning the *in-line* experiments, Fig. 5(a) shows the percentage of bacteria oriented in a range 45–90° for all the grating periods analyzed with the corresponding standard deviations. The highest percentage alignment in these experimental conditions is obtained for 100 μm and 25 μm grating periods. For these two cases we report in Fig. 5(b and c) the polar histograms of bacteria orientation angles in the range 0–90°. For 100 μm case the percentage in the range 45–90° is 80%, from the polar histogram it is clear that a great number of bacteria are oriented with angle between 60° and 90° and a peak is present at 90° (Fig. 5(b)). For 25 μm period the percentage is 75% but a higher number of bacteria are completely oriented and perpendicular to the grating planes as clearly shown in the angular distribution of Fig. 5(c).

After laser irradiation, we monitored the effects of the laser light on bacteria viability by incubating separately, irradiated and not-irradiated bacteria, in fresh LB medium. The growth was monitored until the log phase and, although a short delay was appreciable in irradiated cells at 2 h, no differences were observed at later time points (4–6 h) between the two samples. These results demonstrate that laser irradiation did not have deleterious effects onto the bacteria viability.

The behaviour of bacteria cells when exposed to PR field is very different from that experienced from the HeLa cells investigated in Ref. [52]. We believe that the differences in terms of biological species are a crucial point.

Bacteria are prokaryote cells with cell membrane and cell wall that feel the environment and move in the surrounding bath by swimming.

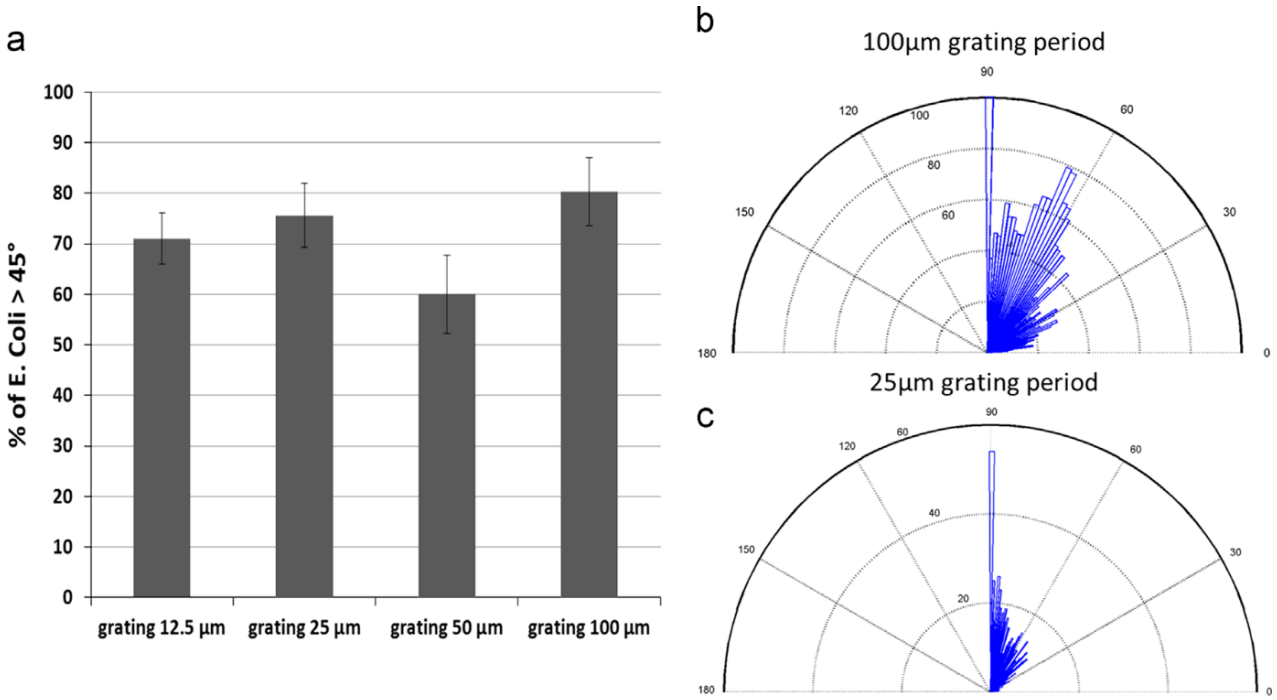

Figure 5: (a) Histograms representation of percentage *E. coli* alignment in case of *in line* mode. (b)–(c) rose-wind plots for the case of 100 mm and 25 mm, respectively [ref. 32].

Cells employed in Ref. [52] are tumoral cell line, they are eukaryotic cell with only cell membrane and they adhere to the surface to move and to reproduce. Bacteria present a simpler structure and are in general more resistant respect to adherent cells. In addition, the experimental conditions are different because in the present experiments we illuminate the sample for 2 min while in Ref. [52] the illumination is kept on the sample for 30 min. Moreover in Ref. [52] the light used to illuminate the sample is no-structured and the crystal is thicker with higher dopant level. Our results prove that PR effect can interact in different way with the biological world respect to the results presented in Ref. [52]. Depending on the experimental parameters, PR fields can be tailored for applications ranging from therapeutic purposes as in Ref. [52] to controlled patterning as in the present work.

The *in-line* tests need the sample placed in the optical setup that is quite bulky and not easily transportable. It would be desirable having a compact and efficient system that could be used for example in microfluidic devices out of the laboratory. For this reason we tested the feasibility of the *E. coli* alignment on Fe: $LiNbO_3$ crystals in a different experimental condition, i.e. the *off line* mode

described before. The same procedures were used for image recording and processing and the results are reported in Fig. 6. Also in the *off line* mode the higher alignment effect was revealed in case of 25 μm and 100 μm gratings.

The percentage of alignment is higher for the experiment performed by in-*line* mode for all the cases analyzed. We hypothesize that the direct laser writing slightly induce a buffer evaporation; thus enhancing the bacteria probability to be close to the surface and, accordingly, to be trapped. In other words, in the *in-line* mode the laser affects bacteria mobility, decreasing their capacity to move respect to the *off-line* mode; thus inducing a small difference in *E. coli* orientations. Concerning the higher bacteria alignment at 25 μm and 100 μm gratings in both the experimental conditions, we believe this result depends on various parameters as the relative length between the bacterium that feels the PV field and the geometry of the field itself, i.e. the grating period. Moreover, we suppose that it also depends on the fluctuation in the bacteria concentration that could occur. Further experiments will be conducted devoted to better understand the influence of these parameters.

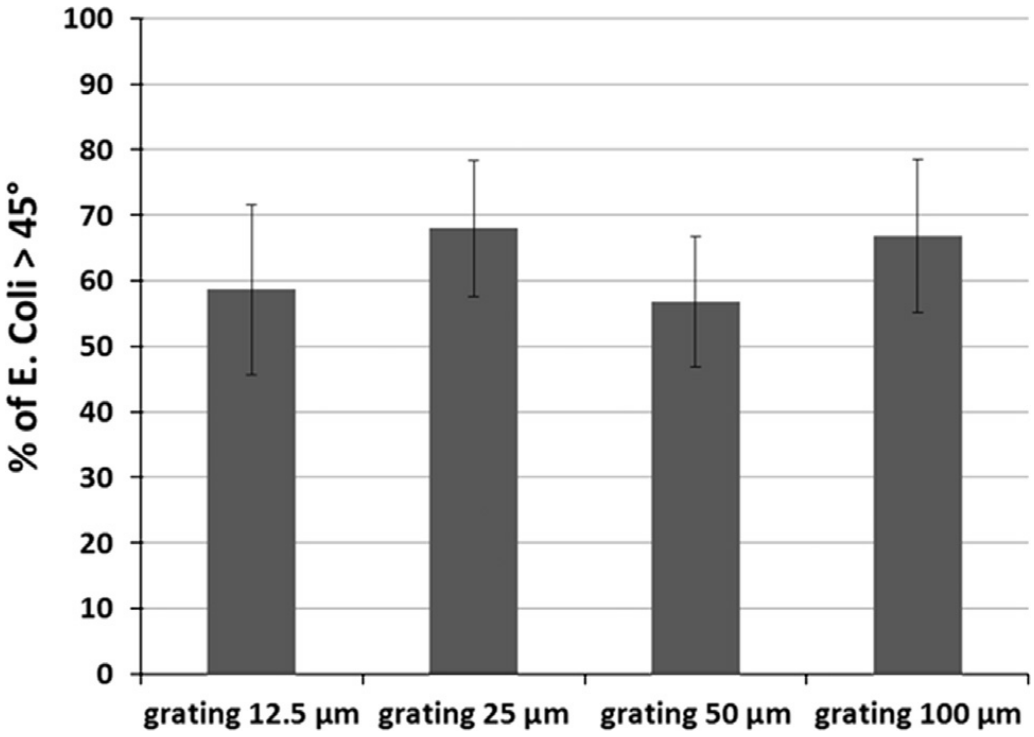

Figure 6: Histograms representation of percentage *E. coli* alignment in case of *off line* mode [ref. 32].

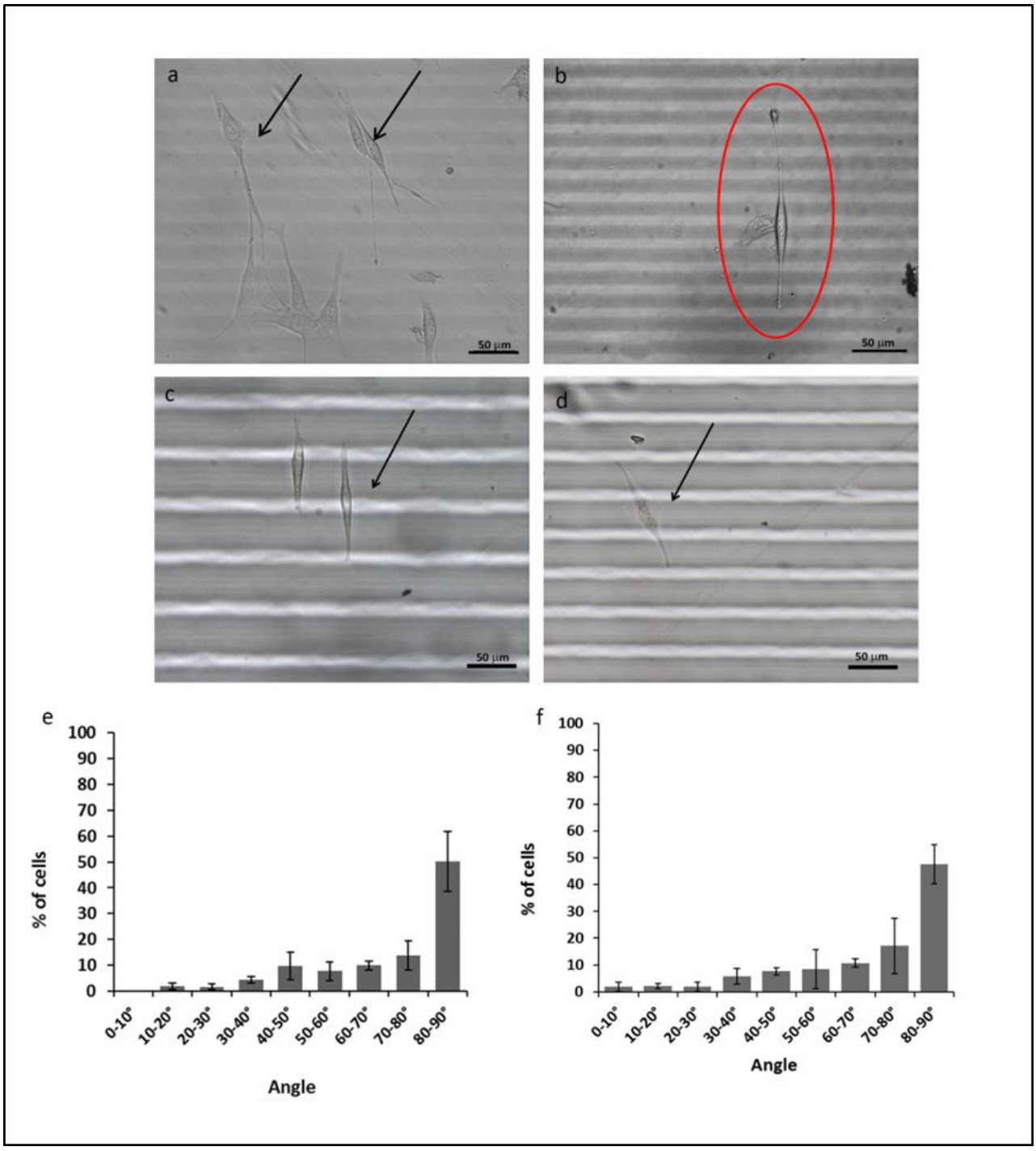

Figure 7: Cell orientation on $liNbO_3$ substrate after 24h. a) Fibroblasts grown on patterned (25micron grids) crystal oriented with an angle comprised between 45-90° b) Higher magnification of cells grown on patterned (25 micron grids) crystal. c-d) Fibroblasts grown on patterned (50 micron grids) crystal oriented with an angle comprised between 45-90° e-f) The graphs report the orientation angles of cells grown on patterned crystal (e) 25 micron grids, (f) 50 micron grids. The mean values for each substrate was evaluated over three biological replicates.

A similar study was designed to investigate the cellular responses occurring when fibroblasts come in contact with new materials [53-55] and to demonstrate the

usefulness of these substrates for cell biology studies. Cells seeded on patterned crystals showed a preferential orientation towards the pattern as 50% of them dispose with an angle comprised between 80-90° (Figure 7), compared to the randomly oriented cells grown on non-patterned crystals. The remaining 50% shows anyway a preferentiality in disposing with an angle higher than 45°.

In the near future, DHM is going to be used as a time-lapse imaging tool for the characterization of dynamic processes.

In this work, we prove a method to trap and orient *E. coli* bacteria and fibroblasts by light exposure onto a functionalized ferroelectric substrate. A systematic study to define the suitable conditions of the electric field gradients has been accomplished. The higher alignment percentage for bacteria is reached when 25 μm, and 100 μm linear gratings are inscribed inside the crystal volume through the PR effect. The related surface potentials are suitable for bacteria alignment in case of direct laser irradiation and, as well as, in case of *off line* trapping. The method proposed allows manipulating bacteria at large scale (few square centimetres area), without labeling them and by a single step process completely driven by laser light modulation.

Moreover, the PR induced DEP is free from electrodes; thus avoiding multiple fabrication steps and integration of different materials. We believe that this technique could have a broad field of potential applications concerning the controlled patterning of bio-samples to study growth dynamics, proliferation and cell–cell interaction mediated by well-organized geometries. Bacteria immobilization could be useful for understanding the early stage formation of biofilms and helping to improve future treatment or avoiding their growth. Furthermore, these crystal properties could open the way for their integration in opto-fluidic system, for example, to purify drinking water or simply for detecting toxicants and environmental agents. Finally, a well-known feature of the PR fields is their writing/ erasing capability that allows defining a kind of DEP reconfigurable electrodes [29]. Possible future applications in biology could exploit such capability to generate and control spatial structure of cells whose relative position can be modified and re-arranged just changing light intensities.

References

[1] M. Papadaki, N. Bursac, R. Langer, J. Merok, G. Vunjak-Novakovic, and L. E. Freed, "Tissue engineering of functional cardiac muscle: molecular, structural, and electrophysiological studies," *Am J Physiol Hear. Circ Physiol*, vol. 280, no. 1, pp. H168–178, Jan. 2001.

[2] P. M. Wigmore and G. F. Dunglison, "The generation of fiber diversity during myogenesis," *Int. J. Dev. Biol.*, vol. 42, pp. 117–125, 1998.

[3] G. Vunjak-Novakovic, G. Altman, R. Horan, and D. L. Kaplan, "Tissue engineering of ligaments," *Annu. Rev. Biomed. Eng.*, vol. 6, pp. 131–156, 2004.

[4] A. Khademhosseini, R. Langer, J. T. Borenstein, and J. P. Vacanti, "Microscale technologies for tissue engineering and biology," *Proc. Natl. Acad. Sci. U. S. A.*, vol. 103, no. 8, pp. 2480–2487, 2006.

[5] C. S. Chen, M. Mrksich, S. Huang, G. M. Whitesides, and D. E. Ingber, "Geometric control of cell life and death.," *Science*, vol. 276, no. 5317, pp. 1425–1428, 1997.

[6] R. McBeath, D. M. Pirone, C. M. Nelson, K. Bhadriraju, and C. S. Chen, "Cell Shape, Cytoskeletal Tension, and RhoA Regulate Stem Cell Lineage Commitment," *Dev. Cell*, vol. 6, no. 4, pp. 483–495, Apr. 2004.

[7] J. A. Burdick and G. Vunjak-Novakovic, "Engineered microenvironments for controlled stem cell differentiation," *Tissue Eng. Part A*, vol. 15, no. 2, pp. 205–219, 2009.

[8] B. Murtuza, J. W. Nichol, and A. Khademhosseini, "Micro- and nanoscale control of the cardiac stem cell niche for tissue fabrication.," *Tissue Eng. Part B. Rev.*, vol. 15, no. 4, pp. 443–454, 2009.

[9] Y.-J. Huang, J. Samorajski, R. Kreimer, and P. C. Searson, "The influence of electric field and confinement on cell motility.," *PLoS One*, vol. 8, no. 3, p. e59447, Jan. 2013.

[10] M. S. Kim, M. H. Lee, B.-J. Kwon, H. J. Seo, M.-A. Koo, K. E. You, D. Kim, and J.-C. Park, "Control of neonatal human dermal fibroblast migration on

poly(lactic-co-glycolic acid)-coated surfaces by electrotaxis.," *J. Tissue Eng. Regen. Med.*, Jan. 2015.

[11] A. K. Dubey, S. D. Gupta, and B. Basu, "Optimization of electrical stimulation parameters for enhanced cell proliferation on biomaterial surfaces.," *J. Biomed. Mater. Res. B. Appl. Biomater.*, vol. 98, no. 1, pp. 18–29, Jul. 2011.

[12] B. M. Gumbiner, "Cell Adhesion: The Molecular Basis of Tissue Architecture and Morphogenesis," *Cell*, vol. 84, no. 3, pp. 345–357, Feb. 1996.

[13] T. Yeung, P. C. Georges, L. A. Flanagan, B. Marg, M. Ortiz, M. Funaki, N. Zahir, W. Ming, V. Weaver, and P. A. Janmey, "Effects of substrate stiffness on cell morphology, cytoskeletal structure, and adhesion.," *Cell Motil. Cytoskeleton*, vol. 60, no. 1, pp. 24–34, Jan. 2005.

[14] A. J. Engler, L. Richert, J. Y. Wong, C. Picart, and D. E. Discher, "Surface probe measurements of the elasticity of sectioned tissue, thin gels and polyelectrolyte multilayer films: Correlations between substrate stiffness and cell adhesion," *Surf. Sci.*, vol. 570, no. 1–2, pp. 142–154, 2004.

[15] S. Lavenus, P. Pilet, J. Guicheux, P. Weiss, G. Louarn, and P. Layrolle, "Behaviour of mesenchymal stem cells, fibroblasts and osteoblasts on smooth surfaces," *Acta Biomater.*, vol. 7, no. 4, pp. 1525–1534, 2011.

[16] R. G. Flemming, C. J. Murphy, G. A. Abrams, S. L. Goodman, and P. F. Nealey, "Effects of synthetic micro- and nano-structured surfaces on cell behavior," *Biomaterials*, vol. 20, no. 6, pp. 573–588, Mar. 1999.

[17] S. V Anand, M. Yakut Ali, and M. T. A. Saif, "Cell culture on microfabricated one-dimensional polymeric structures for bio-actuator and bio-bot applications.," *Lab Chip*, vol. 15, no. 8, pp. 1879–88, Apr. 2015.

[18] I. Tonazzini, S. Meucci, P. Faraci, F. Beltram, and M. Cecchini, "Neuronal differentiation on anisotropic substrates and the influence ofnanotopographical noise on neurite contact guidance," *Biomaterials*, vol. 34, no. 25, pp. 6027–6036, 2013.

[19] C. Rianna, A. Calabuig, M. Ventre, S. Cavalli, V. Pagliarulo, S. Grilli, P. Ferraro, and P. A. Netti, "Reversible Holographic Patterns on Azopolymers for

Guiding Cell Adhesion and Orientation," *ACS Appl. Mater. Interfaces*, vol. 7, no. 31, pp. 16984–16991, 2015.

[20] "94038849.pdf." .

[21] H. Pohl, *Dielectrophoresis : the behavior of neutral matter in nonuniform electric fields*. Cambridge ;;New York: Cambridge University Press, 1978.

[22] R. Pethig, "Dielectrophoresis: an assessment of its potential to aid the research and practice of drug discovery and delivery.," *Adv. Drug Deliv. Rev.*, vol. 65, no. 11–12, pp. 1589–99, Nov. 2013.

[23] Yang, "Dielectrophoretic Separation of Prostate Cancer Cells," *Technol. Cancer Res. Treat.*, vol. 12, no. 1, 2012.

[24] D. S. Gray, J. L. Tan, J. Voldman, and C. S. Chen, "Dielectrophoretic registration of living cells to a microelectrode array," *Biosens. Bioelectron.*, vol. 19, no. 12, pp. 1765–1774, Jul. 2004.

[25] Y. Seki, T. Miyashita, A. Kandori, A. Maki, and H. Koizumi, "Simultaneous measurement of neuronal activity and magnetoencephalography and near-infrared spectroscopy," *J. Biomed. Opt.*, vol. 17, no. 10, 2012.

[26] S.-M. Yang, S.-Y. Tseng, H.-P. Chen, L. Hsu, and C.-H. Liu, "Cell patterning via diffraction-induced optoelectronic dielectrophoresis force on an organic photoconductive chip.," *Lab Chip*, vol. 13, no. 19, pp. 3893–902, Oct. 2013.

[27] C. A. DeForest and D. A. Tirrell, "A photoreversible protein-patterning approach for guiding stem cell fate in three-dimensional gels.," *Nat. Mater.*, vol. 14, no. 5, pp. 523–531, 2015.

[28] J. Ramón-Azcón, S. Ahadian, R. Obregón, G. Camci-Unal, S. Ostrovidov, V. Hosseini, H. Kaji, K. Ino, H. Shiku, A. Khademhosseini, and T. Matsue, "Gelatin methacrylate as a promising hydrogel for 3D microscale organization and proliferation of dielectrophoretically patterned cells.," *Lab Chip*, vol. 12, no. 16, pp. 2959–69, Aug. 2012.

[29] L. Miccio, P. Memmolo, S. Grilli, and P. Ferraro, "All-optical microfluidic chips for reconfigurable dielectrophoretic trapping through SLM light induced patterning.," *Lab Chip*, vol. 12, no. 21, pp. 4449–54, Nov. 2012.

[30] R. Vecchione, S. Coppola, E. Esposito, C. Casale, V. Vespini, S. Grilli, P. Ferraro, and P. A. Netti, “Electro-Drawn Drug-Loaded Biodegradable Polymer Microneedles as a Viable Route to Hypodermic Injection,” *Adv. Funct. Mater.*, vol. 24, no. 23, pp. 3515–3523, Jun. 2014.

[31] I. a Grimaldi, S. Coppola, F. Loffredo, F. Villani, G. Nenna, C. Minarini, V. Vespini, L. Miccio, S. Grilli, and P. Ferraro, “Graded-size microlens array by the pyro-electrohydrodynamic continuous printing method.,” *Appl. Opt.*, vol. 52, no. 32, pp. 7699–705, 2013.

[32] L. Miccio, V. Marchesano, M. Mugnano, S. Grilli, and P. Ferraro, “Light induced DEP for immobilizing and orienting Escherichia coli bacteria,” *Opt. Lasers Eng.*, vol. 76, pp. 34–39, Jan. 2016.

[33] N. C. Carville, L. Collins, M. Manzo, K. Gallo, B. I. Lukasz, K. K. McKayed, J. C. Simpson, and B. J. Rodriguez, “Biocompatibility of ferroelectric lithium niobate and the influence of polarization charge on osteoblast proliferation and function.,” *J. Biomed. Mater. Res. A*, vol. 103, no. 8, pp. 2540–8, Aug. 2015.

[34] C. Christophis, E. A. Cavalcanti-Adam, M. Hanke, K. Kitamura, A. Gruverman, M. Grunze, P. a Dowben, and A. Rosenhahn, “Adherent cells avoid polarization gradients on periodically poled LiTaO3 ferroelectrics.,” *Biointerphases*, vol. 8, no. 1, p. 26, 2013.

[35] V. Marchesano, O. Gennari, L. Mecozzi, S. Grilli, and P. Ferraro, “Effects of Lithium Niobate Polarization on Cell Adhesion and Morphology,” *ACS Appl. Mater. Interfaces*, vol. 7, no. 32, pp. 18113–18119, 2015.

[36] Lines M. E. and G.A. M., “Principles and Applications of Ferroelectrics and Related Materials “ 1977: Oxford

[37] A. Yariv , “Quantum electronics”, John Wiley&Sons (1989)

[38] J. Czochralski, “Ein neues verfahren zur messung der kristallisationsgeschwindigheit der metalle.”, *Phys. Chem.*, 92, 219–221, (1918)

[39] B.T. Matthias, J.P. Remeika , “Ferroelectricity in the Ilmenite Structure.”, *Physical Review*, 76, 1886-1887, (1949)

[40] R.S. Weis, T.K. Gaylord," Lithium niobate: Summary of physical properties and crystal structure", *Appl. Phys. A* , 37, 191 (1985).

[41] Arizmendi L., Photonic applications of lithium niobate crystals. Phys Status Solidi A 2004; 201(2):253-83.

[42] P. Günter and J.-P. Huignard Ed., Photorefractive materials and their applications I, Topics, in: Applied Physics, Vol. 61, (Springer-Verlag, Berlin, 1988).

[43] W. Phillips, J. J. Amodei, and D. L. Staebler, Optical and holographic storage properties of transition metal doped lithium niobate, RCA Review 33, 95 (1972).

[44] Miccio L, et al. All-optical microfluidic chips for reconfigurable dielectro-phoretic trapping through SLM light induced patterning. Lab Chip 2012;12 (21):4449–54.

[45] Vecchione R, et al. Electro-drawn drug-loaded biodegradable polymer microneedles as a viable route to hypodermic injection. Adv Funct Mater 2014; 24(23):3515–23.

[46] Graded-size microlens array by the pyro- electrohydrodynami continuous printing method. Appl Opt 2013; 52 (32):7699–705.

[47] Miccio L, et al. Light induced patterning of poly(dimethylsiloxane) micro-structures. Opt Express 2010; 18(11):10947–55.

[48] Agulló-López F, Calvo GF, Carrascosa M. Fundamentals of photorefractive phenomena. In: Günter P, Huignard J-P, editors. Photorefractive materials and their applications 1. New York: Springer; 2006. p. 43–82.

[49] Buse K. Light-induced charge transport processes in photorefractive crystals I: models and experimental methods. Appl Phys B 1997; 64(3):273–91.

[50] Arregui C, et al. Optoelectronic tweezers under arbitrary illumination patterns: theoretical simulations and comparison to experiment. Opt Express 2014; 22(23):29099–110.

[51] Burgos H, et al. Role of particle anisotropy and deposition method on the patterning of nano-objects by the photovoltaic effect in LiNbO3. Opt Mater 2013; 35(9):1700–5.

[52] Blazquez-Castro A, et al. Tumour cell death induced by the bulk photovoltaic effect of $LiNbO_3$:Fe under visible light irradiation. Photochem Photobiol Sci 2011; 10(6):956–63.

[53] N. C. Carville, L. Collins, M. Manzo, K. Gallo, B. I. Lukasz, K. K. McKayed, J. C. Simpson, and B. J. Rodriguez, "Biocompatibility of ferroelectric lithium niobate and the influence of polarization charge on osteoblast proliferation and function.," *J. Biomed. Mater. Res. A*, vol. 103, no. 8, pp. 2540–8, Aug. 2015.

[54] C. Christophis, E. A. Cavalcanti-Adam, M. Hanke, K. Kitamura, A. Gruverman, M. Grunze, P. a Dowben, and A. Rosenhahn, "Adherent cells avoid polarization gradients on periodically poled LiTaO3 ferroelectrics.," *Biointerphases*, vol. 8, no. 1, p. 26, 2013.

[55] E. B. Malarkey, K. A. Fisher, E. Bekyarova, W. Liu, R. C. Haddon, and V. Parpura, "Conductive Single-Walled Carbon Nanotube Substrates Modulate Neuronal Growth," *Nano Lett.*, vol. 9, no. 1, pp. 264–268, 2009.

Conclusions and future prospective

In conclusion, this innovative optofluidic platform allows the study of hundreds of cells and supplies as output their complete morphologic classification in 3D via the self-rotation of cells in microfluidic channels, in case of red blood cells and allows the analysis of cell behavior on crystal niobate.

The technique of R-TPM is simple, quick, reliable and versatile, it has been proved for cells with different shapes and characteristics, such as RBC as reported in chapter 3, but can be use also for others bio-samples such as Diatoms Algae (DA), as shown in Figure1. A route for full screening at the single-cell level can be a quite challenging achievement by means of the proposed approach.

Applications are foreseen, for example, in the isolation and characterization of "foreign" cancer cells in the blood stream and in revealing specific oceanic contaminants that threaten the ecosystem via the analysis of damaged chloroplasts.

Nevertheless, one of the future prospective of this work could be the possibility to develop a portable and quantitative bio-microfluidic device, including a compact detector (e.g., a camera phone), capable of acquiring images and transmitting digital information over existing communications channels, provides an integrated approach for detecting and diagnosing diseases in locations that are difficult or impractical to access by trained physicians or paramedics. Indeed, experts located remotely from the site where the test is performed can interpret the results of the assays and diagnose disease in real time, without traveling to remote and potentially dangerous locations in case of the analysis of red blood cells.

A LoC technology is nowadays the most appropriate site to recreate the cellular environment and mimic all the external cues and forces affecting the cell behaviour, taking advantage of the micro-fluidic flow control, as well as the miniaturization of components like valves, pumps, mixers and sorters. These features make a LoC extremely promising as a novel device to embed diagnostics tools to be used at the point-of-care, allowing first screenings or accurate analysis in absence of adequate facilities and with untrained personnel, e.g., in developing countries and low-resource settings.

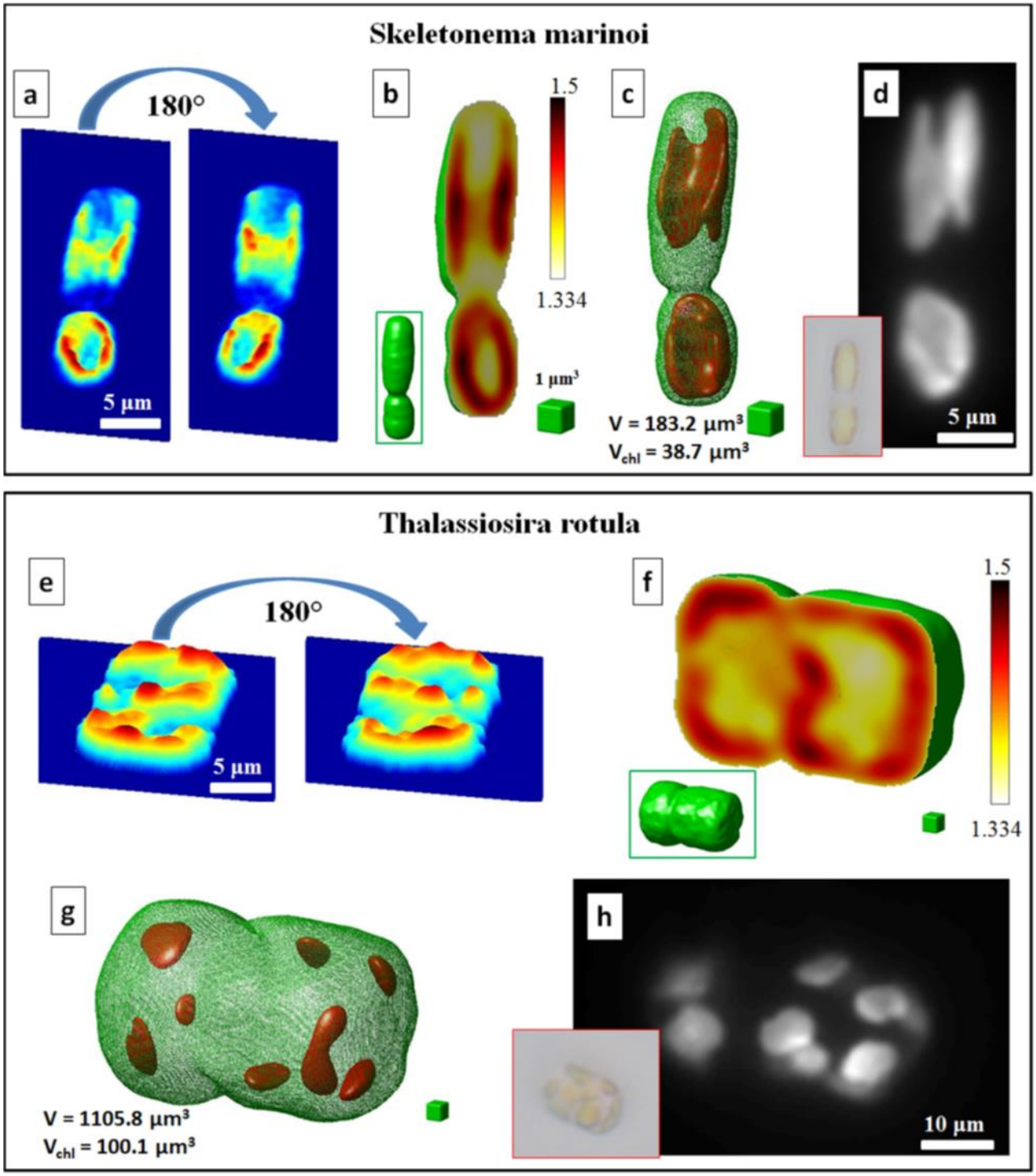

Figure 1: R-TPM for DA. (a-d) *Skeletonema marinoi* and (e-h) *Thalassiosira rotula*. (a,e) Two mirror QPMs used to define the rotating angle retrieval rule. (b,f) Calculated tomograms, where the central slices are shown. Inset figures in the green boxes show the whole tomogram shapes, highlighting the volume occupied by diatoms given by the parameter V. (c,g) are obtained from (b,f), respectively, by applying a RI threshold to extract the 3D distribution of the chloroplasts and their volume (Vchl). (d,h) Fluorescence images used for comparison. Inset figures in the red boxes show the typical bright-field microscope images of the two diatoms [ref. 3, chapter 3].

Environmental monitoring and the emerging field of telemedicine can also benefit from the spread of the LoC technology.

In a wider sense, these technologies permit communications between patients and medical staff with both convenience and fidelity, as well as the transmission of medical, imaging and health informatics data from one site to another. For these reasons, they represent a fascinating topic, with potential applications in many fields, such as for example the tele-diagnosis (Figure2). In the context of the latest imaging techniques, BLIPS technology – the paper-thin photo microscopy lens for all devices – represents a smart system model that could be integrated on a lab-on-chip device. BLIPS is an ultra-portable and very affordable set of mini lenses, which turn the mobile devices into photo digital microscopes in seconds. In this framework, imaging functionalities play a crucial role in gaining a deeper understanding of processes occurring inside the chip, and the study of biological samples in micro-fluidic channels requires some issues to be addressed. In the first place, label-free techniques are highly demanded, in order to avoid sample pretreatments and prevent the risk of altering the natural behaviour due to markers. In the second place, the quantitative information is required from the samples under analysis, e.g., thickness spatial distribution, morphologically relevant parameters, biovolume, refractive index spatial composition and dry mass, to name a few. In the third place, the integration of imaging functionalities on-board LoC devices is a highly pursued goal for point-of-care diagnostics, as the chip portability makes unnecessary the use of bulky diagnostics instruments. Besides, in order to collect statistically relevant data, high-throughput imaging systems, able to analyze a huge number of samples in small periods of time, rapidly extracting information, are highly in demand. These topics have recently attracted growing the interest of many research groups

working in heterogeneous disciplines, ranging from biology and medicine to optics, materials and biomedical engineering, physics, signal processing and information engineering, and the emerging field of bio-informatics. It has become more and more apparent that only a transdisciplinary approach can be successful in matching the above-mentioned requirements and make LoC diagnostics a widespread tool, used worldwide by the general public.

Other demanding applications can be addressed, for example in the isolation and characterization of circulating tumor cells in the blood stream, for leukemia cells detection and for bacteria and diatoms identification for water monitoring studies.

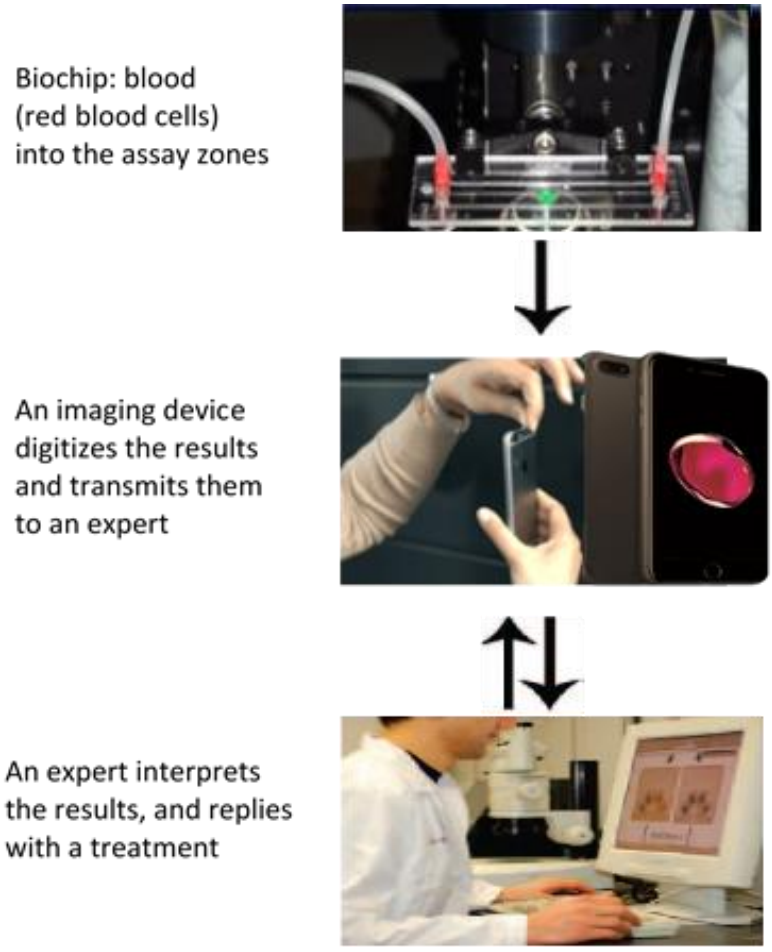

Figure 2: General strategy for performing inexpensive bioassays in remote locations and for exchanging the results of the tests with offsite technicians

.

A Appendix

A.1 Cell culture

A.1.1 Blood samples and isolation of red blood cells

Human blood (~ 4.0 ml) was collected in a 7.2-mg Ethylenediaminetetraacetic acid K2 (EDTA) vacutainer tube (BD, Plymouth, PL6 7BP, UK) from a healthy volunteer.

Complete and diluted blood is shown in figure1.

Blood was centrifuged at room temperature at 2500 rpm for 15 minutes to separate RBCs at the bottom of the sterile centrifugation tube from the plasma and buffy coat. After centrifugation, the plasma and buffy coat were discarded, and the RBC pellet (~ 1.5 ml) was washed with a saline solution of 0.90% w/v of Sodium chloride (NaCl) in sterile water in a 1:1 ratio and re-centrifuged at room temperature at 2500 rpm for 10 minutes. After the second centrifugation, the supernatant fraction was removed, and an aliquot of isolated RBCs (~ 100 µl) was diluted in 10 ml of the saline solution of 0.90% w/v of Sodium chloride (NaCl) in sterile water with a final osmolarity of 308 mOsm/L to maintain the osmotic pressure of the RBCs. Isolated RBCs are shown in figure 2.

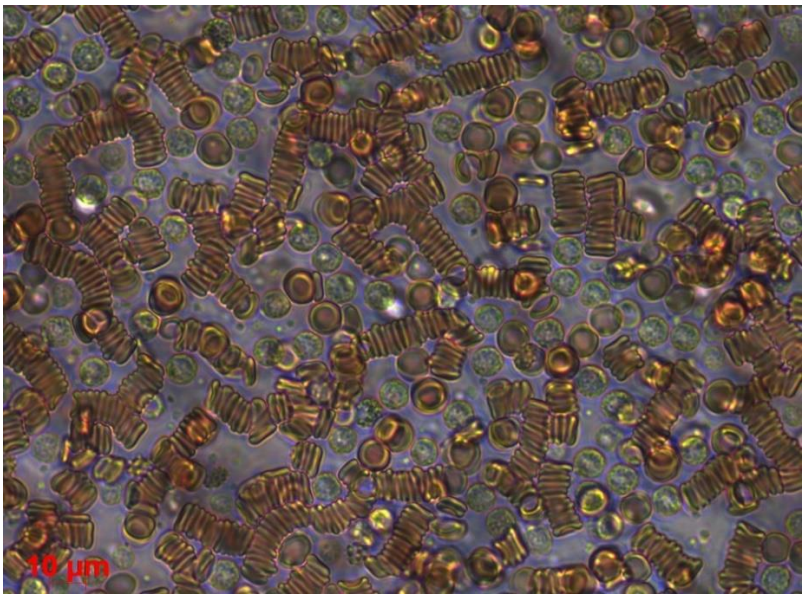

Figure1: Complete and diluted human blood

For the experiments, a final volume of diluted RBCs (~100 µl) was used. Altered RBC shapes were obtained by changing the buffer osmolarity, and a buffer of 205 and 410 mOsm/L was used to perform experiments under hypotonic and hypertonic conditions, respectively.

The same procedure was adopted for sick samples. The first was from a patient affected with iron refractory iron deficiency anemia (IRIDA) caused by mutations in the TMPRSS6 gene (L63Pfs13-W590R in compound heterozygosity) and the second sample from a patient affected with alpha-thalassemia caused by a heterozygous deletional event of both in-cis HBA1 genes (--CAMPANIA in heterozygosity).

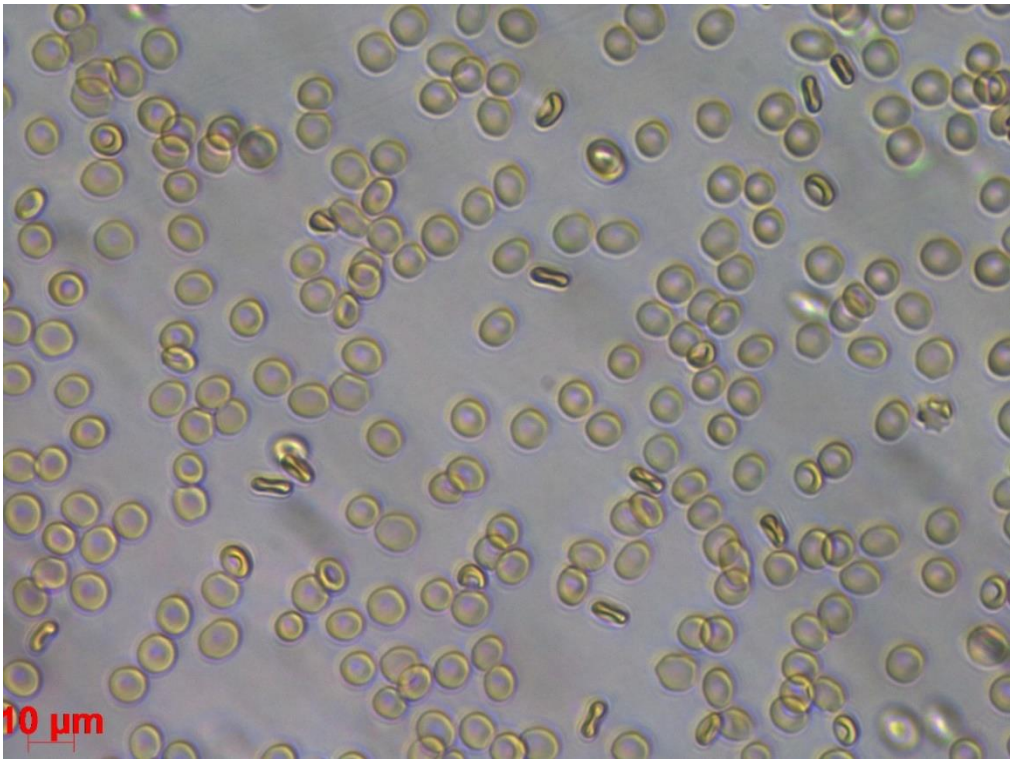

Figure 2: Isolated RBC

A.1.2 Cell line model: Murine embryonic fibroblast cell (NIH 3T3)

NIH 3T3 fibroblasts are cells from *Mus musculus,* mouse organism, they are harvested from embryo tissue.

NIH cells were grown in Dulbecco's Modified Eagle Medium supplemented with 10% Fetal Bovine Serum (both Life Technologies, Carlsbad, CA, USA), 2 mM L-glutamine (Sigma, St. Louis, MO), and 100 U/ml penicillin 100 µg/ml streptomycin at 37 °C at 5% CO_2. They show a typical fibroblast morphology and are adherent cells. Adherent cell lines grow *in vitro* until they have covered the surface area available or the medium is depleted of nutrients. At this point the cell lines should be sub cultured in order to prevent the culture dying. To maintain the same conditions during the experiments, cells were counted and put in a 35 mm Willco-dish (Willcowells BV, Amsterdam, The Netherlands) in a temperature and humidity controlled environment (using a micro-incubator by Bioscience Tools, San Diego, CA, USA).

A.1.3 Bacteria culture

E. coli DH5-alpha was plated and incubated on agar plates. The day before the beginning of experiment, a single bacterial colony was picked up and cultured in Luria-Bertani (LB) broth medium (10 g/l NaCl, 10 g/l tryptone, 5 g/l yeast extract) at 37 °C in a shaker incubator for 16–18 h to achieve saturation conditions. A 1:5 volumetric dilution of cell culture was then grown in LB until reaching the log phase corresponding to a cell concentration of 4 x 10^8 cells/ml, verified by OD measurements at 600 nm. Cells were then centrifuged at 5000 rpm for 10 min in order to separate the cells from the medium and, then re-suspended in fresh LB medium to reach a concentration of 2 x 10^7ml.

A.2 Methods and cell culture protocols

A.2.1 Trypsinization protocol of adherent cells

In order to remove adherent cells from a culture surface, treatment with trypsin was adopted.

1. Remove medium from culture vessel by aspiration and wash the monolayer with Ca^{+2} and Mg^{+2} - free salt solution to remove all traces of serum. Remove salt solution by aspiration.
2. Dispense enough trypsin or trypsin-EDTA solution into culture vessel to completely cover the monolayer of cells and place in 37 °C incubator for approximately 2 minutes.
3. Remove the trypsin or trypsin-EDTA solution by aspiration and return closed culture vessel to incubator. The coated cells are allowed to incubate until cells detach from the surface. Progress can be checked by examination with an inverted microscope. The time required to remove cells from the culture surface is dependent on cell type, population density, serum concentration in the growth medium, potency of trypsin and time since last subculture. NIH cells need approximately 5 minutes to detach from plate. Trypsin causes cellular damage and time of exposure should be kept to a minimum.
4. When trypsinization process is complete the cells will be in suspension and appear rounded.
5. It is advisable to add serum or medium containing serum to the cell suspension as soon as possible to inhibit further tryptic activity which may damage cells.
6. Cells can be resuspended by gently pipetting the cell suspension to break up the clumps. Further dilution can be made, if required, for cell counts and/or subculturing.

A.2.2 Counting cells by Burker chamber hemocytometer

Counting chambers serve to determine the number of particles per volume unit of a liquid. The particles (e.g., cells, leucocytes, erythrocytes, thrombocytes, bacteria, fungus spores, pollen) are visually counted under an inverted microscope. The microscope-slide-sized base plate is made of special optical glass.

Milled grooves divide the surface into two large fields (outside) and three narrow ridges (inside). The two outer fields are for inscriptions, whereas the ridges are ground and polished. The central ridge (= chamber bottom) has two engraved sets of rulings for counting, separated by a groove.

Generally the chamber bottom on the central ridge is 0.1 mm lower (= chamber depth) than the two outer ridges. Hence, when a cover glass is placed on top, there is a gap of 0.1 mm between the glass and the central ridge. The lateral boundaries of the volume to be counted are formed by the imaginary planes projected vertically onto the boundary lines of the ruling.

Burker chamber was used for cell counting. The ruling shows 9 large squares of 1 mm^2 each (Fig.3 A). These are used for counting leucocytes. Each large square is subdivided by double lines (0.05 mm apart) into 16 group squares with 0.2 mm sides (Fig.3 B).

The double lines form mini squares with an area of 0.0025 mm^2. Al least three squares delimited by triple lines are counted and each square corresponds to 1/10 mm^3. An arithmetic average of counted cells is carried out. Then, the average is multiplies for dilution factor equal to 10.000.

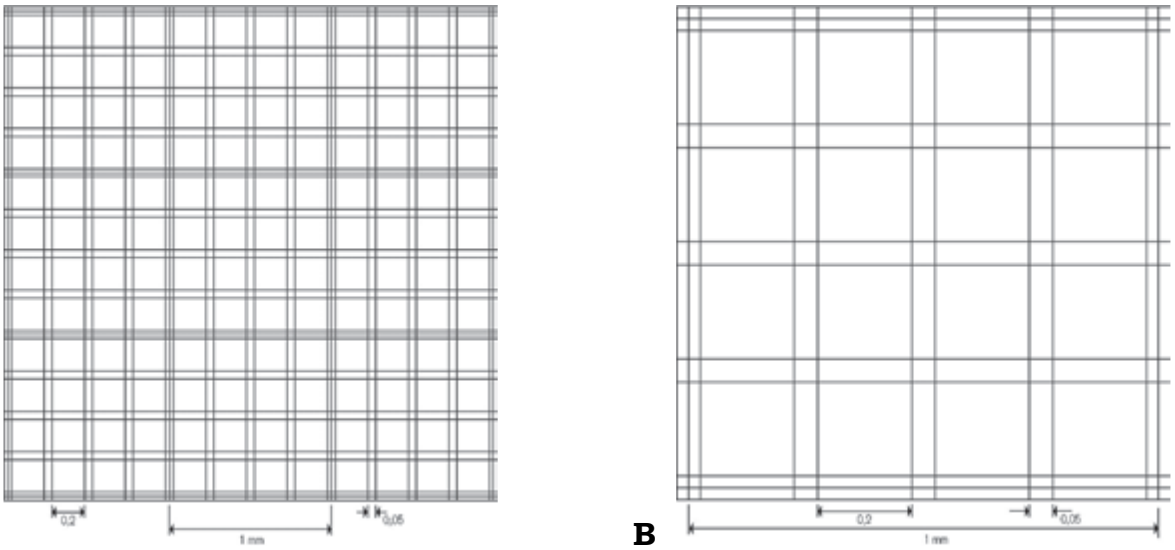

Figure 3: A) Burker chamber. B) Large central square

Equation for particle determination:

Number of cells/ml volume: (average of three squares) * 10000

A.2.3 Cryopreservation/thawing procedure of mammalian cells

1. Detach cells from the substrate with dissociation agents. Detach as gently as possible to minimize damage to the cells.
2. Resuspend the detached cells in a complete growth medium and establish the viable cell count.
3. Centrifuge at ~200 x g for 5 min to pellet cells. Using a pipette, withdraw the supernate down to the smallest volume without disturbing the cells.
4. Resuspend cells in freezing medium (composed of 20 % fetal bovine serum and 80% complete medium) to a concentration of 5 x 10^6 to 1 x 10^7 cells/ml.
5. Aliquot into cryogenic storage vials. Place vials on wet ice or in a 4°C refrigerator, and start the freezing procedure within 5 min.
6. Cells are frozen slowly at 1°C /min. This can be done by programmable coolers or by placing vials in an insulated box placed in a -70°C to -90°C freezer, then transferring to liquid nitrogen storage**.**

For thawing procedure:

The following protocol describes a general procedure for thawing cryopreserved cells.

1. Remove the cryovial containing the frozen cells from liquid nitrogen storage and immediately place it into a 37°C water bath.
2. Quickly thaw the cells (< 1 minute) by gently swirling the vial in the 37°C water bath until there is just a small bit of ice left in the vial.
3. Transfer the vial it into a laminar flow hood. Before opening, wipe the outside of the vial with 70% ethanol.
4. Transfer the desired amount of pre-warmed complete growth medium appropriate for your cell line dropwise into the centrifuge tube containing the thawed cells.
5. Centrifuge the cell suspension at approximately 200 × g for 5–10 minutes. The actual centrifugation speed and duration varies depending on the cell type.
6. After the centrifugation, check the clarity of supernatant and visibility of a complete pellet. Aseptically decant the supernatant without disturbing the cell pellet.
7. Gently resuspend the cells in complete growth medium, and transfer them into the appropriate culture vessel and into the recommended culture environment.

A.2.4 Cell viability assay: propidium iodide and Hoechst 33342 staining

The cell death induced by IE (well decribed in chapter 3, paragraph 3.3.1) was compared to a standard chemical assay, in order to validate the results.
Figure 4 shows the typical microscope images of adherent cells under IE (first line) and under SE (second line), observed under standard differential interference contrast (DIC) and fluorescence contrast. The appearance of necrotic cells was monitored using Hoechst 33342 and propidium iodide (PI) double- staining assay. The cells were stained with 5 µg/ ml Hoechst 33342 for 10 min in the dark at 37

°C. Next, PI was added to the culture medium (final concentration of 50 µg/ml) and incubated for 20 min in incubator. Stained nuclear/DNA morphology of cells was analysed by a fluorescence microscope using a magnification objective of 10× and 40×.

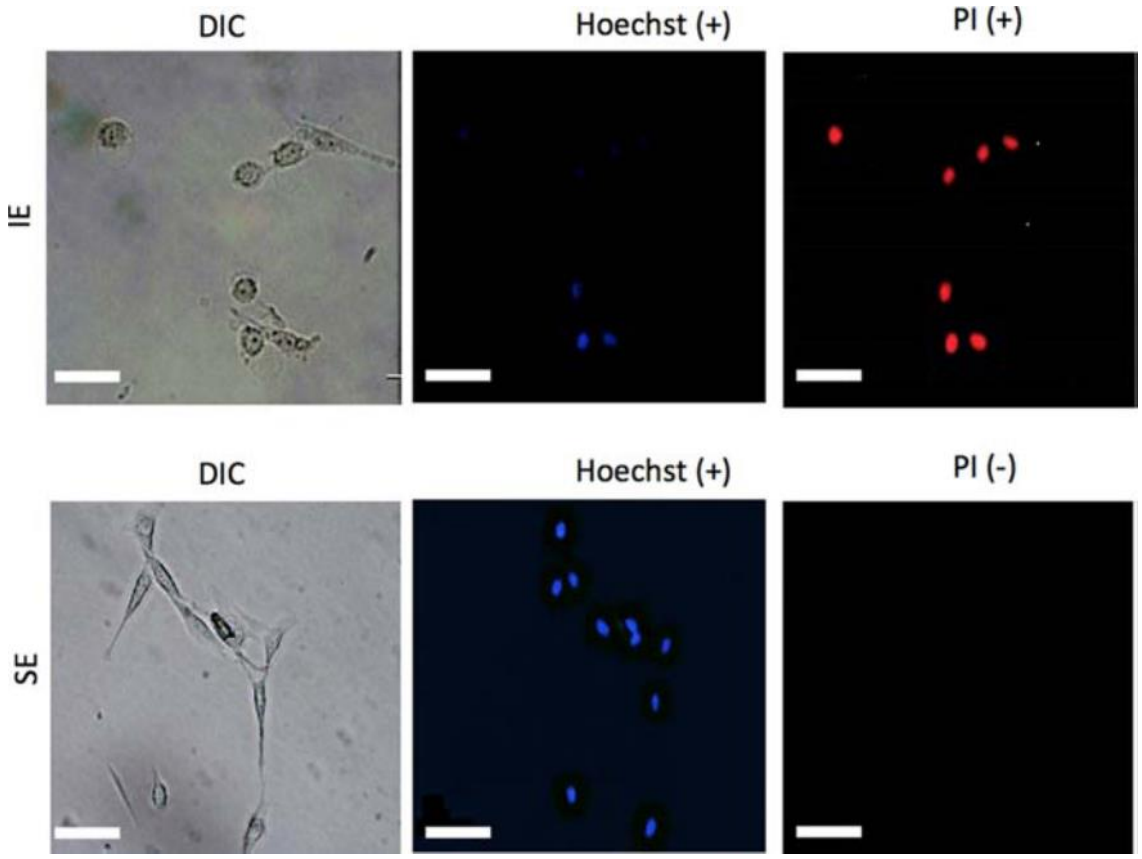

Figure 4: Optical microscope images of adherent cells subjected to IE (first line) and SE (second line), under DIC and fluorescence contrast. The blue colour refers to Hoechst labelling and the red colour to propidium iodide labelling. Scale bar 50 µm.

The cells were classified as viable (spherical blue fluorescence of nucleus), and necrotic (red fluorescence of large nucleus with spherical vesicles stained by PI). All experiments were performed in triplicate.

The chemical assay confirms the necrotic nature of the cells subjected to IE and the viability of those under SE. Figure 5 shows the microscope large view image of the cell culture sample investigated in Figure 4, just after light-induced necrosis. The highlighted region corresponds to the surface exposed to the blue laser during IE. Figure 5(a) shows the bright contrast image and Figure 5(b) the corresponding

fluorescence image after PI labelling. The most of the inner cells exhibited the round shape typical of dead cells, while the outer ones appeared clearly adhered to the substrate, thus confirming that the continuous exposure to blue light is toxic and that the blue light irradiation is the only responsible of cell death. In fact, the accurate control of temperature and pH in the micro-incubator allowed us to exclude any thermal or chemical side effect. During irradiation, photons are transferred from light to cell molecules. For wavelengths at the edge of the visible spectrum, as is the case of blue light, the molecules tend to gain both rotational and vibrational energy. Therefore the mean kinetic energy increases and induces simultaneously photothermal, photomechanical and photochemical damages**.**

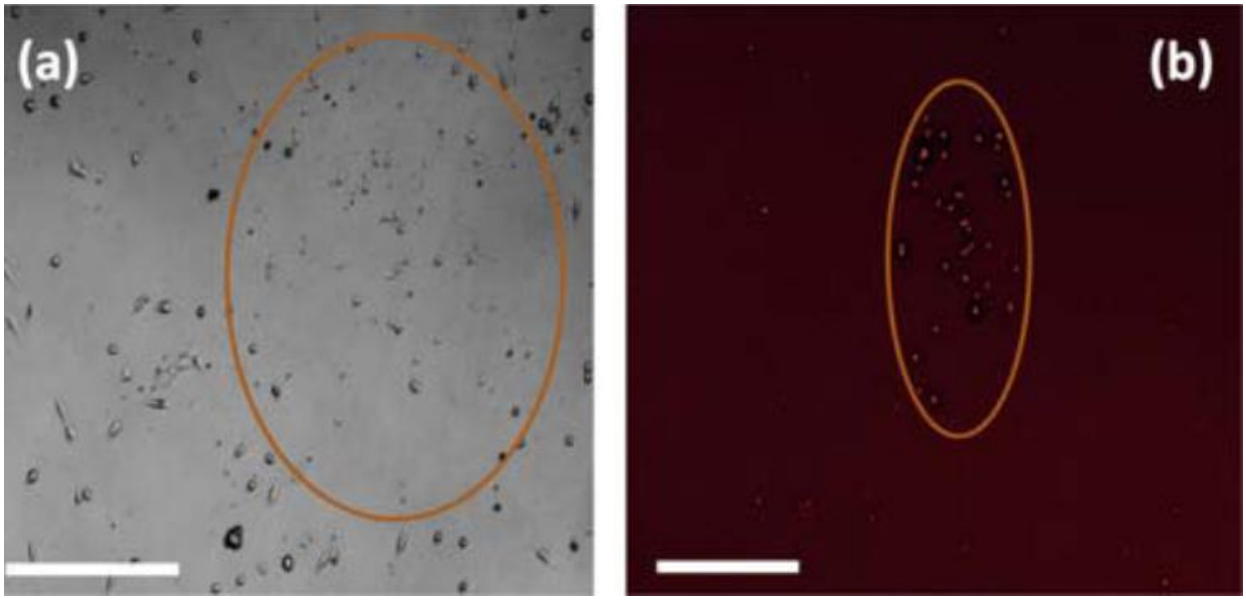

Figure 5: Large view image of the cell culture dish investigated in Figure 8, under (a) bright and (b) fluorescence contrast. Scale bar 500 μm.

A.2.5 Gene transfection protocol for actin filaments visualization

In order to study cell mechanics (well described in chapter 4) lipofectamine LTX reagent (by Life Technologies, lot 1468812) was used to transfect the pCMVLifeAct-TagRFP (ibidi) mammalian expression vector in NIH/3T3 cells in order to visualize filamentous actin (F-actin) in living cells as shown in Figure 6.

After 15 min of incubation with 0.75 µg of pDNA in lipoplexes, cells were returned to culture with complete medium and grown at 37 °C and 5% CO_2

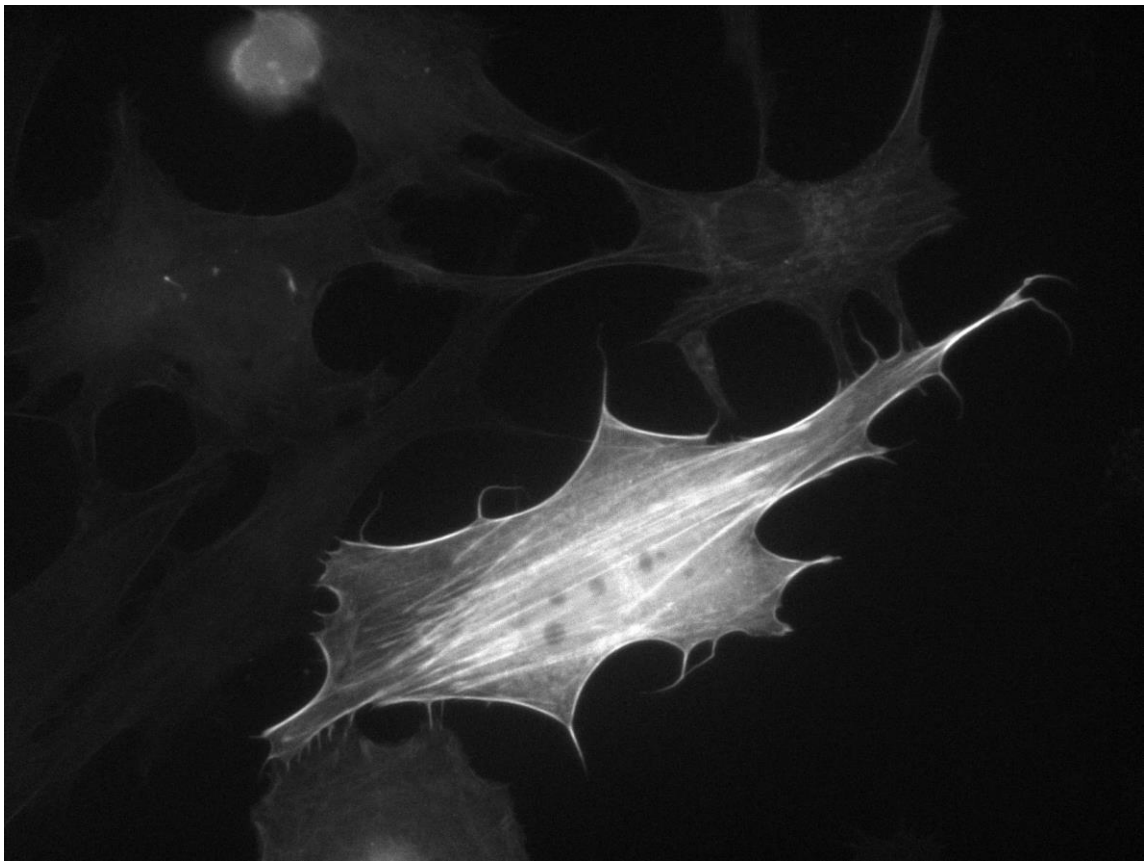

Figure 6. Gene transfection. Actin filaments in adherent NIH3T3 cells under a conventional fluorescence microscope. The image was acquired with 20x objective lens.

A.2.6 Surface treatment of cell culture dish

In order to avoid cell adhesion onto plate surface, that was necessary for the experiments in suspension (described in detail in chapter 4, paragraph 4.2.1) previously, 35 mm Willco-dishes were coated treating the surface in a low pressure O_2 plasma system (Femto System, Diener Electronic GmbH & Co. KG, Ebhausen, Germany) for micro-cleaning and to activate their surfaces; they were then spin-

coated with 50 µl of Fluorolink PFPE S10 (Solvay Polymers Ltd, Warrington, UK) at 10000 rpm for 2 min and incubated under vacuum for 30 min. After incubation, Fluorolink was de-activated adding de-ionized water and Petri dishes were rinsed with Ethanol 100% (Delchimica Scientific Glassware, Naples, Italy) in order to discard Fluorolink in excess, then they were sterilized with a UV lamp treatment for 30 min.

A.2.7 Statistical analysis of cell polarization

The approach described in this manuscript in chapter 5, paragraph 5.4 for cell orientation analysis is divided into two main processes. The first process provides an image collection for each sample. A number of 50 cells (three biological replicates) were analysed per 25µm grid and 50µm grid.
The cell number was calculated from a set of 20 images, acquired by an inverted microscope in bright field (Axio Zeiss Vert). The second process employs the angle tool of ImageJ, a public domain image analysis software by the National Institute of Health Once loading a cell-crystal image into ImageJ, the angle tool measures the angle value, 45°-90° angle range, between the major axis of the cell and the pattern lines. Afterwards the results of the angle values from the "results window" can be directly copied to Excel spreadsheet for statistical analysis**.**

A.2.8 Immunostaining assay

For fluorescence staining, cells were fixed with 4% paraformaldehyde for 15 min. at room temperature, permeabilized with 0.1% Triton X-100 and labelled with Alexa fluor 488 phalloidin (Sigma) for revealing the actin filaments. The nuclei were stained with blue fluorescent Hoechst 33342 dye, trihydrochloride trihydrate (Molecular Probes Invitrogen). The actin pattern and nuclei distribution of the NIH on the four samples are shown in Figure 7. These images were obtained by immunofluorescence on fixed Fibroblast 24 h after plating them on the different substrates. Confocal experiment shows a strong difference in the morphology of

the actin filament between the cells grown on control samples and on patterned samples. On the 25µm and 50 µm gratings cells appear polarized with an angle between 90° and 45° respect to the grid, they showed a smaller size and an irregular formation of actin stress fibres; also the nuclei seem to be aligned in the same direction, indicating a possible difference also in the cell differentiation and a change even in a normal cell physiology. On the 50µm grating the cells are bigger than 25 µm grating probably because of the wideness of the grid and a less narrow confinement.

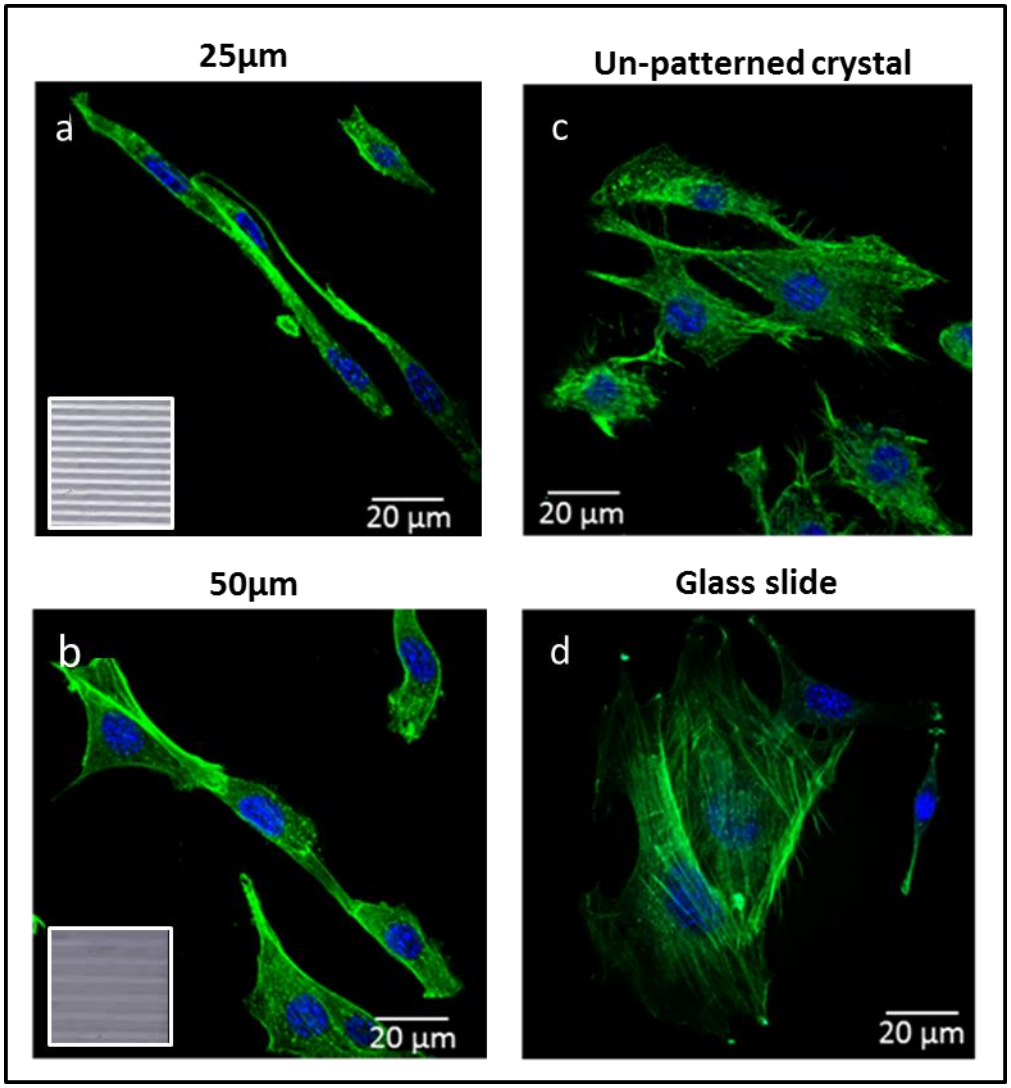

Figure 7: Morphology of nuclei and actin filaments. Typical confocal images of cells seeded onto (a) a crystal sample patterned at 25 µm period, (b) a crystal sample patterned at 50 µm period, (c) an un-patterned crystal and (d) a glass slide. The cells were stained by Alexa fluor 488 phalloidin and blue fluorescent Hoechst 33342 dye, trihydrochloride trihydrate (Molecular Probes Invitrogen) for visualizing nuclei and actin filaments.

On the other hand cells plated onto un-patterned crystal and normal glass appear rounder than the others with a well-organized actin structure and nuclei and a normal polymerization of actin stress fibers can be appreciate (Figure 7 (c-d)). As shown in the figure elliptical nuclei polarization follow actin orientation. In c and d (control samples), keep the typical round shape of nuclei and are not polarized in the actin filaments direction, while actin filaments are more structured then actin on 25 and 50 μm

A.2.9 Biocompatibility assay

The biocompatibility of crystals Lithium Niobate was tested by using a conventional live/dead viability/cytotoxicity assay kit (Molecular Probes Invitrogen).

The cells were seeded at a density of 1×10^5 cells on four kinds of substrates, 25, 50 μm, un-patterned crystal and glass slide, which was used as a control (Delchimica Scientific Glassware), and were incubated in Petri dishes for 24h. After incubation 1 mL of the combined live/dead cell staining solution (2 μM calcein AM and 4 μM EthD-1 in D-PBS) was added to the dish and incubated for 45 min at room temperature. The kit contains calcein-AM, which stains live cells as green, and the ethidium homodimer, which stains the dead cells as red. Samples were then observed under a conventional fluorescence upright microscope (Axio Imager, Carl Zeiss).

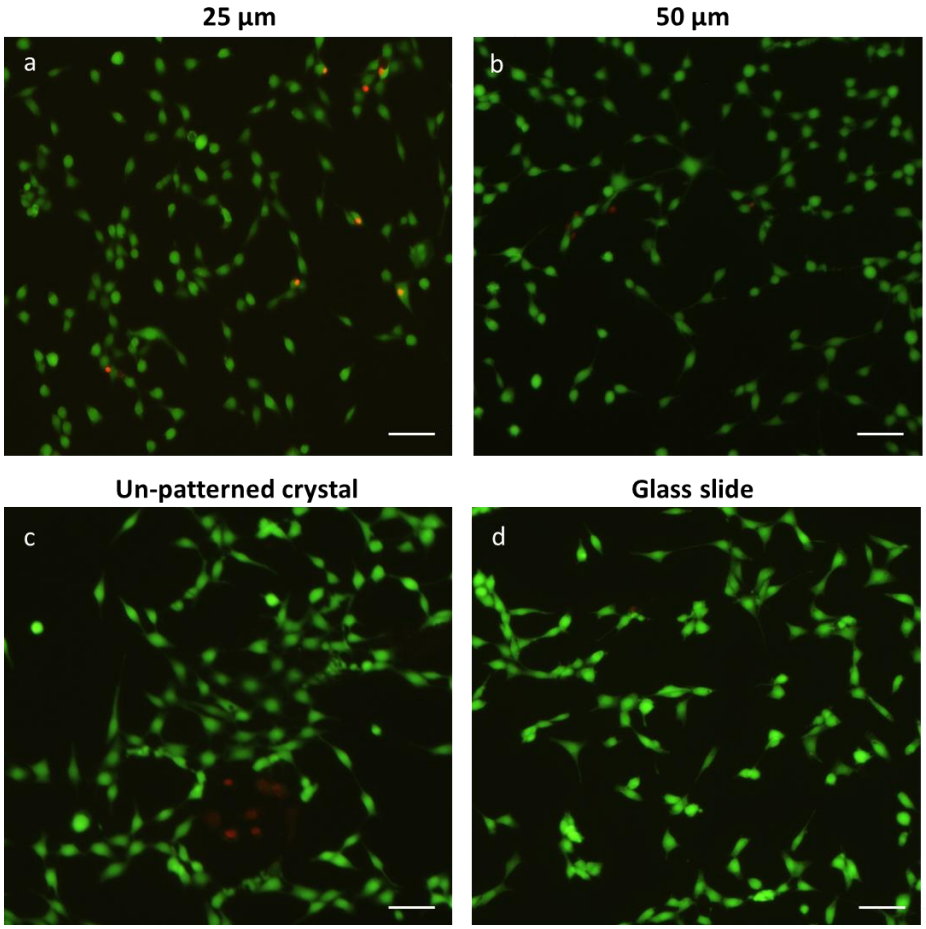

Figure 8: Biocompatibility Assay by live/dead viability staining. Typical fluorescence images of the cells seeded on (a) 25µm grids, (b) 50µm grids, (c) un-patterned crystal and (d) glass slide, treated by the live/dead assay after 24 h of incubation. Live cells are stained in green by Calcein-AM; dead cells are stained in red by Ethidium Homodimer. No evidence of red cells are on any of four substrates. Scale bars 50 µm.

Acknowledgements

I wish to express my sincere appreciation to those who have contributed to this thesis and supported me during this amazing journey. I would especially like to thank all the co-authors of the scientific papers included in this PhD thesis.
The doctoral research project was carried out at Institute of Applied Science and Intelligent Systems - ISASI (CNR - National Research Council of Italy), under the supervision of Dr. Pietro Ferraro.
I would like to thank all my colleagues at Federico II - University of Naples and express my gratititude to the Doctorate Committee members, and in particular to our PhD Coordinator, Professor Giuseppe Mensitieri, and to Professor P. A. Netti, for their positive and constructive attitude as well as their valuable advice.
Many thanks to the academic team of the CEINGE – Advanced Biotechnologies, Department of Molecular Medicine and Medical Biotechnology, and in particular to Professor Achille Iolascon, who provided me with valuable support and contributed to scientific publications that I co-authored. Above all I'd like to express my sincere gratitude to Dr. Domenico Paduano and Dr. Francesco Paduano, for their precious support of my research activity and for their kind availability.
Most important, I am very grateful to my PhD thesis advisor, Dr. Lisa Miccio, for his excellent guidance, for encouraging my research activity, and for his caring attitude that has supported me over the years.
Undertaking this PhD has been a life-changing experience for me and I really appreciate the patient and unflagging support as well as exemplary guidance that I have received from my co-advisor, Dr. Pasquale Memmolo, and Dr. Francesco Merola to whom I would like to give my special thanks for encouraging my growth as a research scientist and for his role in creating an excellent atmosphere for conducting my research. Their advice and support of my research as well as my career have been greatly appreciated.
I also would like to thank all my friends and colleagues – in particular Dr. Alejandro Calabuig and Dr. Vito Pagliarulo - and those who have accompanied me over the years as well as those I've gotten to know during these last three years in Italy, with whom I have enjoyed so many stimulating conversations.

Last but not least, I would like to thank Giuseppe, for being there with unconditional support when I've needed it most – and finally, my parents, Sergio, Maria Rosaria, Domenico and Michele for their love, inspiration and steadfast encouragement to pursue my dreams. Thank you!